ACTIVE DAMPING OF A BERNOULLI-EULER BEAM VIA END POINT IMPEDANCE CONTROL USING DISTRIBUTED PARAMETER TECHNIQUES

by

Gregory Michael Procopio

SUBMITTED TO THE DEPARTMENT OF MECHANICAL ENGINEERING
IN PARTIAL FULFILLMENT OF THE REQUIREMENTS
FOR THE DEGREES OF

BACHELOR OF SCIENCE IN MECHANICAL ENGINEERING

and

MASTER OF SCIENCE IN MECHANICAL ENGINEERING

at the

MASSACHUSETTS INSTITUTE OF TECHNOLOGY
September 18, 1986

Signature of Author_____
Department of Mechanical Engineering
September 18, 1986

Certified by_____
James E. Hubbard, Jr., Ph.D.
Thesis Supervisor

Accepted by_____
Professor Ain A. Sonin
Chairman, Departmental Graduate Committee

ACTIVE DAMPING OF A BERNOULLI-EULER BEAM VIA END POINT IMPEDANCE CONTROL USING DISTRIBUTED PARAMETER TECHNIQUES

by

Gregory Michael Procopio

submitted to the Department of Mechanical Engineering
in partial fulfillment of the requirements
for the degrees of Bachelor of Science
and Master of Science in Mechanical Engineering

ABSTRACT

A characteristic impedance end point controller was designed for a Bernoulli-Euler beam which nulls reflections of traveling waves at the boundaries of the beam. This controller was designed without truncation of the beam model. It was also designed without consideration of modes. The controller was designed to have the same functional form as the characteristic impedance of the beam so that the beam appeared to be semi-infinite, and no waves were reflected from the boundary to which the controller was attached. This was analogous to the characteristic termination of an electrical transmission line. The control law included a 2×2 matrix and used linear and angular velocity information from the tip of the beam to produce a seperate control force and moment.

There were two cases which were the subject of experimentation. The first was a clamped-free beam which was studied because of its general nature and could be applied to flexible space structures. The second case was a clamped-sliding beam which was used to model a Remote Center Compliance device which is a flexible device used in close-tolerance robotic assembly. The clamped-sliding beam had no angular motion at the tip so that it was not possible to match the characteristic impedance of the beam. However, by using a fractional derivative controller ($\sqrt{s}$) it was possible to control vibrations at the tip.

Digital simulations for a free-free beam and a clamped-free beam showed that the characteristic impedance controller damped out vibrations effectively. The simulations also showed that the fractional derivative controller controls vibrations in the clamped-sliding beam. The digital simulations assumed gains that required hefty control actuators. The experimental actuators were made with piezoelectric polymer film which made very low-gain actuators. Even so, they were able to improve the damping of the beams. The settling time for the clamped-free beam was reduced by a factor of 4, and the damping factor ζ for the clamped-sliding beam was increased 152%.

Thesis Supervisor: James E. Hubbard, Jr., Ph.D.
Title: Lecturer in the Department of Mechanical Engineering

ACKNOWLEDGEMENT

I would first of all like to thank Jim Hubbard for taking me in as one of his students when I had only a flimsy idea of what I wanted to do. His patience and faith helped keep me sane. I would also like to thank everyone in the Structures Lab (Tom Bailey, Shawn Burke, Alex Gruzen, and John Plump) for their help and companionship; they have actually made the crunch at the end a good time. I only wish I had started working with them sooner. Thanks go to Pete Sifferlen and Chris Trainor for putting up with me when I monopolized their personal computers for weeks to run simulations. I thank Vern Assarian and the rest of Group 30C for supporting me even when it seemed I was no longer part of that group. Last, but certainly the first, I thank my friend Patrice Parris for the moral support needed to survive (and for giving me a place to sleep the final few weeks).

I acknowledge the support of this thesis research by the Instrument Development Department contract # 35876.

Contents

List of Figures

List of Tables

Chapter 1

Introduction

In dealing with the dynamic control of devices or vehicles which have flexible members, the modelling of the higher order structural modes is often ignored and a rigid body model is used. This is justified by ensuring that the system is robustly stable with respect to modelling errors. In some cases, even if stability is not a problem, the excitation of the higher order structural modes is of concern with respect to such issues as fatigue, positioning accuracy, and vibration isolation. Instead of treating structural modes as a modelling error, a continuous parameter model may be included from the outset.

The modelling of flexible structures is often done using finite element techniques. However, in order to approach the modelling problem from an analytical standpoint, the structure model is broken up into larger pieces such as flexible, continuous beams or plates. Structures in which the use of long, flexible, lightly damped beams is common are space structures. Devices such as remote control arms on the shuttle, and antennaes and solar panels on satellites are good candidates for impedance damping methods.

A specific device which could benefit from active damping is the Remote Center Compliance (RCC), which is a device used in high precision robotic assembly to enable the mating of parts with close tolerances. A precision RCC is made with long, thin beams so that the stiffness is small. However, since the RCC is carrying the assembly tool and a piece part, this leads to a low frequency, lightly damped structure. The usefulness of the RCC lies within its quasi-static mechanical properties, but higher order vibrational modes are easily

excited [14][1]. The RCC is a good candidate for active damping and is a specific application studied in this document. A schematic showing a basic RCC is given in Fig. 1.1. The conceptual operation of an RCC is depicted in Fig. 1.2 which demonstrates how a lateral force causes a lateral deflection with no rotation, and a moment about the compliance center causes rotation about that center with no lateral deflection. A typical high precision RCC may use six wires, much like that depicted in Fig. 1.1. The wires act as beams, and since the RCC vibrates at low frequencies, the wires can be modelled as Bernoulli-Euler beams. The problem of damping the RCC can therefore be viewed as a problem in the damping of a beam with specific boundary conditions.

A controller for the active vibration control of a continuous beam can be designed without truncating the continuous parameter model to a lumped parameter model. The method being studied is to formulate a state space model of a continuous beam and append an end point controller which has the same functional form as the characteristic impedance of the beam [22]. The characteristic impedance termination will null any reflections from the end of the beam so that it appears to be semi-infinite and no standing waves are produced on the beam. This approach is analogous to the characteristic termination of an electrical transmission line which is a well developed subject [19]. The end point impedance controller is not designed with consideration of damping modes of the beam, but is designed to absorb waves traveling along the beam.

The actuator used to control vibrations of the beam is a piezoelectric, polymer film attached along the length of the beam [2]. By shaping the distribution of the film, the effort applied by the film can be made to appear as a moment and/or force at the beam's tip [9].

In order to match the impedance of the beam at its tip, the end point impedance controller requires both linear and angular velocity information at the tip of the beam. In many beam configurations (i.e., pinned, sliding, clamped) this is not possible. This implies that the controller can match the impedance of the beam only when the end is not geometrically constrained (this does not exclude tip masses and inertias). However, even for those cases where one of the velocity signals is not available, a controller may still be designed using a subset of the end point impedance controller. The use of fractional operator

[1]Numbers in square brackets designate references in the Bibliography at end of paper.

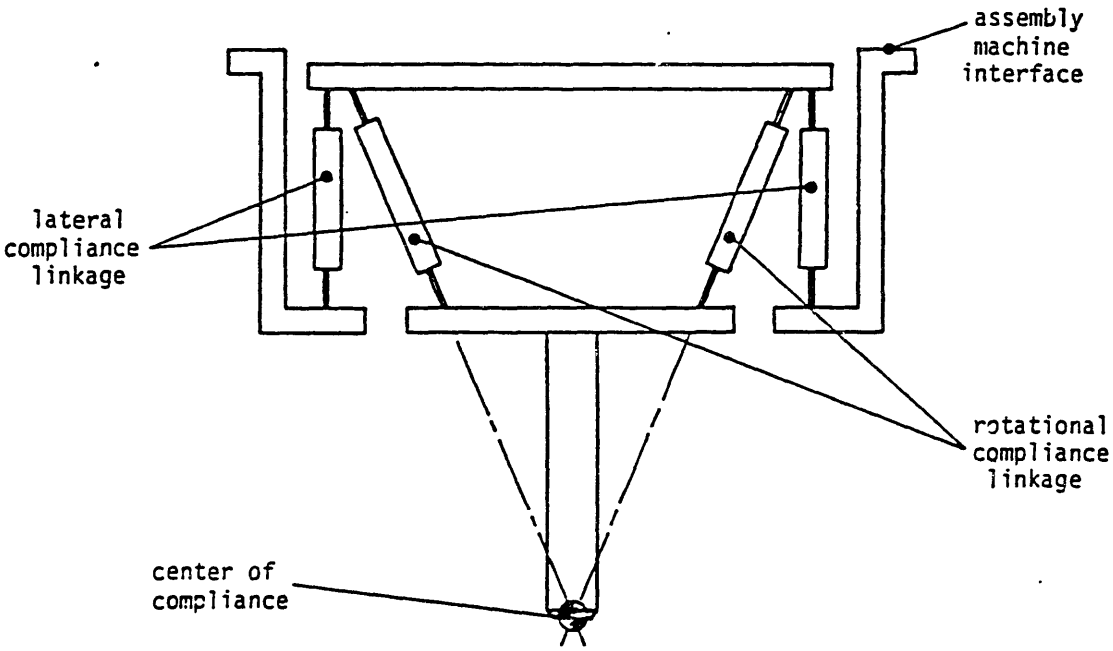

Figure 1.1: Schematic representation of a six wire RCC

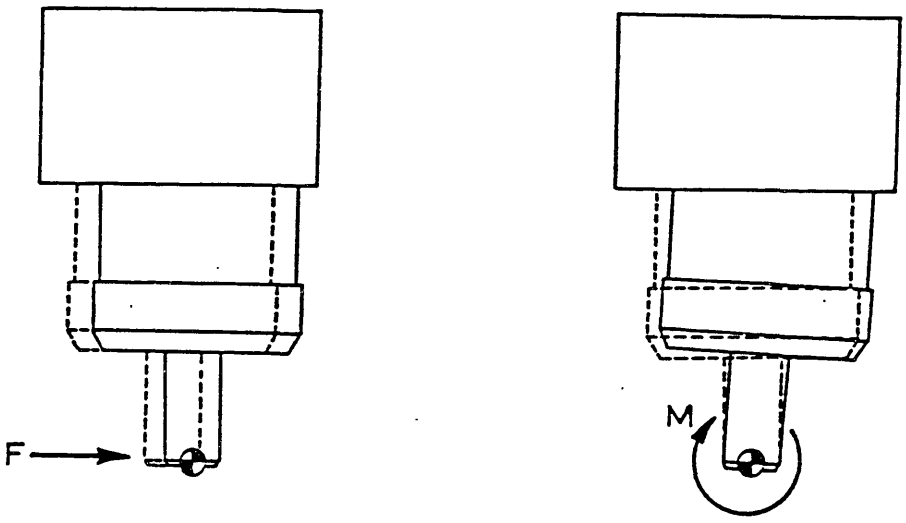

a. Response to applied lateral force.

b. Response to applied moment.

Figure 1.2: Ideal response of RCC to applied forces and moments

controllers, which are by-products of the end-point impedance controller, yields good results in the damping of a system with no angular motion at the tip as in the Remote Center Compliance. Because of the requirement for both linear and angular velocity information to implement the end point impedance controller, the second case studied in this document (in addition to the RCC case) is a cantilever beam. The cantilever beam has both linear and angular motion at the free end so that the full end point impedance controller can be implemented.

Although the piezoelectric film used for actuating the control force and moment is not strong enough to match the impedance at the end of the beam, the controllers being studied still result in improved structural damping.

The theoretical basis for the end point impedance controller and its derivation are described in Chapter 2. Chapter 2 also includes the derivation of transfer functions for the two specific cases studied in this paper: the clamped-free (cantilever) beam, and the clamped-sliding (RCC) beam. Chapter 3 describes the method used to approximate the infinite-order transfer functions with finite order Padé type approximations so that digital simulations of the dynamics of the beam with and without the controller could be done. Simulations for a free-free beam, a clamped-free beam, and a clamped-sliding beam are demonstrated. The experimental analysis of the clamped-free beam and the clamped-sliding beam cases is documented in Chapter 4. Conclusions and recommendations for further research are discussed in the final chapter.

Chapter 2

Theory

In much of the research on the dynamic properties of the Bernoulli-Euler beam, a model is chosen which aims to approximate the distributed nature of the beam into a lumped parameter model. This is a convenient approach because of the completeness of lumped parameter systems theory, but in the design of a controller for the real system, the higher modes have been neglected and the controller may have to be modified to accomodate these unmodeled modes late in the design process [4].

A more complete approach is to design a controller based on a distributed parameter model of the system. In Linear Systems by Schwarz & Friedland, the method for modelling distributed parameter systems is presented primarily through the use of an electrical transmission line as an example. The concepts developed for the electrical transmission line are extended to include other systems including the transverse motion of a Bernoulli-Euler beam [19].

2.1 General Distributed Parameter System[1]

The general representation of a one dimensional distributed system may be expressed by the following partial differential equation.

$$\frac{\partial \mathbf{y}}{\partial x} = \mathbf{F}_0\mathbf{y} + \mathbf{F}_1\frac{\partial \mathbf{y}}{\partial t} + \mathbf{F}_2\frac{\partial^2 \mathbf{y}}{\partial t^2} + \cdots + \mathbf{F}_r\frac{\partial^r \mathbf{y}}{\partial t^r} + \mathbf{q}(t,x) \tag{2.1}$$

where the matrices $\mathbf{F}_i = [f^i_{jk}]$ are in general functions of x but for homogenous systems are constants, and $\mathbf{y} = [y_j]$ is the vector of the variables of interest

[1] For a more complete discussion, refer to Chapter 12 of Schwarz and Friedland [19].

where $y_j \equiv y_j(t,x)$. The term $\mathbf{q}(t,x)$ is a forcing term. For many systems of interest, the highest order of the partial differential equations among the system of equations in equation 2.1 is second order so that $\mathbf{F}_i = \mathbf{0}$ for $i \geq 3$. This implies that for most distributed systems, the dynamic behavior can be modelled with a diffusion equation (first order partial differential equation), or a wave equation (second order partial differential equation).

Taking the Laplace transform of equation 2.1:

$$\frac{d\mathbf{Y}}{dx} = (\mathbf{F}_0 + \mathbf{F}_1 s + \mathbf{F}_2 s^2)\mathbf{Y} + \bar{\mathbf{Q}}(s,x) \tag{2.2}$$

where

$$\bar{\mathbf{Q}}(s,x) = \mathbf{Q}(s,x) - \mathbf{F}_1\mathbf{y}(0,x) - \mathbf{F}_2[\dot{\mathbf{y}}(0,x) + s\mathbf{y}(0,x)].$$

Equation 2.2 is now an ordinary differential equation in x with the solution

$$\mathbf{Y}(s,x) = \mathbf{H}(s,x-x_0)\mathbf{Y}(s,x_0) + \int_{x_0}^{x} \mathbf{H}(s,x-\xi)\bar{\mathbf{Q}}(s,\xi)d\xi \tag{2.3}$$

where $\mathbf{H}(s,x)$ is the fundamental matrix for the homogeneous form of equation 2.2, and when the matrices $\mathbf{F}_i$ are constant, the fundamental matrix takes the form:

$$\begin{aligned}\mathbf{H}(s,x) &= \exp[(\mathbf{F}_0 + \mathbf{F}_1 s + \mathbf{F}_2 s^2)x] \\ &= \mathbf{I} + (\mathbf{F}_0 + \mathbf{F}_1 s + \mathbf{F}_2 s^2)x + (\mathbf{F}_0 + \mathbf{F}_1 s + \mathbf{F}_2 s^2)^2 \tfrac{x^2}{2!} + \cdots .\end{aligned} \tag{2.4}$$

This formulation is completely analogous to the evaluation of the state transition matrix for lumped parameter systems, and the method is based upon the Cayley-Hamilton theorem [13].

The fundamental matrix $\mathbf{H}(s,x)$ is a matrix of analytic functions in the s-plane for all finite x. However, for $x \to \infty$, some of the elements of the fundamental matrix may diverge. For a real system, the condition of $x \to \infty$ describes a semi-infinite system, and it is expected that the physical variables remain finite regardless of the position x. Therefore, if the fundamental matrix is to describe a real semi-infinite system, the physical variables must be constrained to have a relationship such that the divergent elements of $\mathbf{H}(s,x)$ are cancelled. This relationship between the physical variables is known as the constraint of characteristic termination.

The constraint of characteristic termination may be determined by diagonalizing the system matrix

$$\mathbf{F}_0 + \mathbf{F}_1 s + \mathbf{F}_2 s^2 = \mathbf{T}(s)\mathbf{\Lambda}(s)\mathbf{T}^{-1}(s) \tag{2.5}$$

where $\mathbf{\Lambda}(s)$ is a diagonal matrix of the system eigenvalues, and $\mathbf{T}(s)$ is a transformation matrix whose columns are the eigenvectors of the system, $\mathbf{T}_i(s)$. The eigenvalues are found by solving for the zeros of the characteristic polynomial

$$\left|\lambda\mathbf{I} - \mathbf{F}_0 - \mathbf{F}_1 s - \mathbf{F}_2 s^2\right| = 0. \tag{2.6}$$

The eigenvalues of the system $\lambda_i(s)$ may then be used to solve for the eigenvectors by solving the eigenvalue problem

$$(\mathbf{F}_0 + \mathbf{F}_1 s + \mathbf{F}_2 s^2)\mathbf{T}(s) = \mathbf{T}(s)\Lambda(s). \tag{2.7}$$

The fundamental matrix $\mathbf{H}(s, x)$ may now be written in the form

$$\begin{aligned}\mathbf{H}(s,x) &= \exp[(\mathbf{F}_0 + \mathbf{F}_1 s + \mathbf{F}_2 s^2)x] \\ &= e^{\mathbf{T}(s)\mathbf{\Lambda}(s)\mathbf{T}^{-1}(s)x}.\end{aligned} \tag{2.8}$$

Inspection of the Taylor series expansion of equation 2.8 reveals that

$$\mathbf{H}(s,x) = \mathbf{T}(s)e^{\mathbf{\Lambda}(s)x}\mathbf{T}^{-1}(s) \tag{2.9}$$

and the solution of the homogenous form of equation 2.2 may be written as

$$\mathbf{Y}(s,x) = \mathbf{T}(s)e^{\mathbf{\Lambda}(s)x}\mathbf{T}^{-1}(s)\mathbf{Y}(s,0). \tag{2.10}$$

By defining a new set of variables

$$\mathbf{U}(s,x) = \mathbf{T}^{-1}(s)\mathbf{Y}(s,x) \tag{2.11}$$

equation 2.10 is transformed to

$$\mathbf{U}(s,x) = e^{\mathbf{\Lambda}(s)x}\mathbf{U}(s,0). \tag{2.12}$$

Since $\mathbf{\Lambda}$ is a diagonal matrix of the system eigenvalues $\lambda_i(s)$, the matrix $e^{\mathbf{\Lambda}(s)x}$ is also a diagonal matrix of the exponentials $e^{\lambda_i(s)x}$. In order for the system variables to remain finite for any positive x, it is necessary that the positive eigenvalues do not appear in the matrix $e^{\mathbf{\Lambda}(s)x}$. This further requires

that the components of $\mathbf{U}$ corresponding to the positive eigenvalues must be zero in a semi-infinite system. In other words, suppose the first m eigenvalues of a k^{th} order system are positive. Then

$$\mathbf{U}(s,x) = \left[\begin{array}{c} U_1(s,x) \\ \vdots \\ U_m(s,x) \\ \hline U_{m+1}(s,x) \\ \vdots \\ U_k(s,x) \end{array}\right] = \left[\begin{array}{c} \mathbf{0} \\ \hline \bar{\mathbf{U}}(s,x) \end{array}\right] \tag{2.13}$$

but

$$\mathbf{U}(s,x) = \mathbf{T}^{-1}(s)\mathbf{Y}(s,x) = \left[\begin{array}{c} \mathbf{W}_1(s) \\ \hline \mathbf{W}_2(s) \end{array}\right] \mathbf{Y}(s,x) = \left[\begin{array}{c} \mathbf{0} \\ \hline \bar{\mathbf{U}}(s,x) \end{array}\right] \tag{2.14}$$

where $\mathbf{W}_1(s)$ is an $m \times k$ matrix whose columns are the first m *reciprocal-* or *left*-eigenvectors[2] corresponding to the first m positive eigenvalues.

Therefore, in a physical, semi-infinite system the dynamic variables are related through the equation of characteristic constraint:

$$\mathbf{W}_1(s)\mathbf{Y}(s,x) \equiv \mathbf{0} \quad \text{for all } x. \tag{2.15}$$

Simply stated, the equation of characteristic constraint defines a relationship between the dynamic variables of a semi-infinite, one-dimensional, distributed parameter system. This relationship between the variables must hold true at any point along a semi-infinite system, or along a finite system before any waves have reached the end point where there may be reflections. The equation of characteristic constraint may be used to define a control law for end-point control such that the characteristic constraint is enforced at the end point making the system appear to be semi-infinite. In this case, any waves will not be reflected at the end point but will be absorbed by the controller.

2.2 Transverse Motion of a Beam

Two well known models for a distributed parameter, elastic beam are the Timoshenko model and the Bernoulli-Euler model. The Timoshenko model is more

[2]The *left*-eigenvectors are those which solve $\mathbf{W(s)}(\mathbf{F}_0 + \mathbf{F}_1 s + \mathbf{F}_2 s^2) = \mathbf{\Lambda}(s)\mathbf{W}(s)$. Note that $\mathbf{W}(s) = \mathbf{T}^{-1}(s)$. [18]

complete and can be used for a wider range of applications than the Bernoulli-Euler model. The Bernoulli-Euler model is sufficient for low frequency, long wavelength applications.[12] For the purposes of this research, where the primary interest lies with the lower frequency modes of the beam, the Bernoulli-Euler beam was used. The Bernoulli-Euler model assumes that all energy is stored as potential energy due to bending, and kinetic energy due to transverse, linear motion of the beam. (This model neglects the potential energy due to shearing, and kinetic energy due to rotational inertia which are included in the Timoshenko model). There are four variables needed to completely describe the state of the system in the Bernoulli-Euler formulation for the beam. The symbols y, θ, M, and Q denote transverse displacement, angular rotation, bending moment and transverse shear force respectively as shown in Fig. 2.1. There are four relations associated with the beam:

$$M = EI\frac{\partial^2 y}{\partial x^2} \tag{2.16}$$

$$\frac{\partial Q}{\partial x} = -\rho A\frac{\partial^2 y}{\partial t^2} \tag{2.17}$$

$$Q = \frac{\partial M}{\partial x} \tag{2.18}$$

$$\theta = \frac{\partial y}{\partial x} \tag{2.19}$$

where equation 2.16 is the bending moment equation for a beam, equation 2.17 is Newton's second law, equation 2.18 describes moment balance, and equation 2.19 describes geometry. I is the area moment of inertia of the beam cross section, E is Young's modulus, A is the beam cross-sectional area, and ρ is the density. Equations 2.16–2.18 may be combined, using dynamic equilibrium constraints, to yield the Bernoulli-Euler equation:

$$a^2\frac{\partial^4 y}{\partial x^4} + \frac{\partial^2 y}{\partial t^2} = 0 \tag{2.20}$$

where

$$a^2 = \frac{EI}{\rho A}.$$

The Laplace transform of the Bernoulli-Euler equation (assuming zero initial conditions) yields an ordinary differential equation in x and s:

$$s^2 y(x,s) + a^2\frac{d^4 y(x,s)}{dx^4} = 0 \tag{2.21}$$

where $y(x,s) \equiv \mathcal{L}y(x,t)$. In order to transform the Bernoulli-Euler equation into the general form of equation 2.1, let

$$\mathbf{Y} = \begin{pmatrix} \dot{y} \\ \dot{\theta} \\ m \\ q \end{pmatrix} \tag{2.22}$$

where

$$\begin{pmatrix} \dot{y} \\ \dot{\theta} \\ m \\ q \end{pmatrix} = \begin{pmatrix} sy(x,s) \\ s\theta(x,s) \\ \frac{a}{EI}M \\ \frac{a}{EI}Q \end{pmatrix}.$$

These four states are the Laplace transforms of the transverse velocity, angular velocity, bending moment, and transverse shear force, with M and Q scaled to have the same dimensions as $\dot{y}$ and $\dot{\theta}$, respectively. With this choice of variables, the matrices $\mathbf{F}_0$, $\mathbf{F}_1$, and $\mathbf{F}_2$ of equation 2.2 are

$$\mathbf{F}_0 = \begin{bmatrix} 0 & 1 & 0 & 0 \\ 0 & 0 & 0 & 0 \\ 0 & 0 & 0 & 1 \\ 0 & 0 & 0 & 0 \end{bmatrix}; \quad \mathbf{F}_1 = \begin{bmatrix} 0 & 0 & 0 & 0 \\ 0 & 0 & \frac{1}{a} & 0 \\ 0 & 0 & 0 & 0 \\ -\frac{1}{a} & 0 & 0 & 0 \end{bmatrix}; \quad \mathbf{F}_2 = \mathbf{0}. \tag{2.23}$$

This yields a state space form for the Bernoulli-Euler equation

$$\frac{d}{dx}\begin{pmatrix} \dot{y} \\ \dot{\theta} \\ m \\ q \end{pmatrix} = \begin{bmatrix} 0 & 1 & 0 & 0 \\ 0 & 0 & p & 0 \\ 0 & 0 & 0 & 1 \\ -p & 0 & 0 & 0 \end{bmatrix}\begin{pmatrix} \dot{y} \\ \dot{\theta} \\ m \\ q \end{pmatrix} \tag{2.24}$$

with $p \equiv s/a$. Equation 2.24 may be written conveniently as

$$\frac{d\mathbf{Y}}{dx} = \mathbf{A}\mathbf{Y}. \tag{2.25}$$

The eigenvalues and eigenvectors of the system may be found by solving equation 2.6

$$|\lambda\mathbf{I} - \mathbf{A}| = \begin{vmatrix} \lambda & -1 & 0 & 0 \\ 0 & \lambda & -p & 0 \\ 0 & 0 & \lambda & -1 \\ p & 0 & 0 & \lambda \end{vmatrix} = \lambda^4 + p^2 = 0. \tag{2.26}$$

The four roots of equation 2.26 are

$$\lambda_1 = \sqrt{p}\left(\frac{1+j}{\sqrt{2}}\right)$$

$$\lambda_2 = \sqrt{p}\left(\frac{1-j}{\sqrt{2}}\right)$$

$$\lambda_3 = \sqrt{p}\left(\frac{-1+j}{\sqrt{2}}\right)$$

$$\lambda_4 = \sqrt{p}\left(\frac{-1-j}{\sqrt{2}}\right).$$

Notice that the eigenvalues are all proportional to λ_1, i.e. the four roots are λ_1, $-j\lambda_1$, $j\lambda_1$, $-\lambda_1$. The transformation matrix needed to diagonalize the matrix **A** is

$$\mathbf{T} = \frac{1}{2}\begin{bmatrix} p & p & p & p \\ p\lambda_1 & p\lambda_2 & p\lambda_3 & p\lambda_4 \\ \lambda_1^2 & \lambda_2^2 & \lambda_3^2 & \lambda_4^2 \\ \lambda_1^3 & \lambda_2^3 & \lambda_3^3 & \lambda_4^3 \end{bmatrix}. \tag{2.27}$$

(This is very similar to the transformation of a matrix in companion form to a diagonal matrix. See reference [13].) In this particular case, because of the relationship between the eigenvalues, the inverse of the transformation matrix takes a special form

$$\mathbf{T}^{-1} = \frac{1}{2}\begin{bmatrix} p^{-1} & (p\lambda_1)^{-1} & \lambda_1^{-2} & \lambda_1^{-3} \\ p^{-1} & (p\lambda_2)^{-1} & \lambda_2^{-2} & \lambda_2^{-3} \\ p^{-1} & (p\lambda_3)^{-1} & \lambda_3^{-2} & \lambda_3^{-3} \\ p^{-1} & (p\lambda_4)^{-1} & \lambda_4^{-2} & \lambda_4^{-3} \end{bmatrix}. \tag{2.28}$$

Inspection of equation 2.14 shows that

$$\mathbf{W}_1 = \frac{1}{2}\begin{bmatrix} p^{-1} & (p\lambda_1)^{-1} & \lambda_1^{-2} & \lambda_1^{-3} \\ p^{-1} & (p\lambda_2)^{-1} & \lambda_2^{-2} & \lambda_2^{-3} \end{bmatrix}. \tag{2.29}$$

The equation of characteristic constraint for a Bernoulli-Euler beam is therefore

$$\begin{bmatrix} p^{-1} & (p\lambda_1)^{-1} & \lambda_1^{-2} & \lambda_1^{-3} \\ p^{-1} & (p\lambda_2)^{-1} & \lambda_2^{-2} & \lambda_2^{-3} \end{bmatrix}\begin{pmatrix} \dot{y} \\ \dot{\theta} \\ m \\ q \end{pmatrix} = \begin{pmatrix} 0 \\ 0 \end{pmatrix}. \tag{2.30}$$

The equation of characteristic constraint may be expanded into a pair of complex equations

$$\begin{aligned} \dot{y} + \tfrac{1-j}{\sqrt{2p}}\dot{\theta} - jm - \tfrac{1+j}{\sqrt{2p}}q = 0 \\ \dot{y} + \tfrac{1+j}{\sqrt{2p}}\dot{\theta} + jm - \tfrac{1-j}{\sqrt{2p}}q = 0 \end{aligned} \tag{2.31}$$

which may be solved to form a characteristic impedance

$$\begin{pmatrix} m \\ q \end{pmatrix} = \begin{bmatrix} -1 & -\sqrt{2/p} \\ \sqrt{2p} & 1 \end{bmatrix} \begin{pmatrix} \dot{y} \\ \dot{\theta} \end{pmatrix}. \tag{2.32}$$

The characteristic impedance of the beam is the relationship required for a semi-infinite beam as discussed in Section 2.1. As will be shown in the section 2.4, the characteristic impedance can be used as a control law at one end of a finite beam to create a system that behaves as if it were semi-infinite, i.e., a beam in which travelling waves are not reflected when they reach the end of the beam.

2.3 Propagation Operators

It is somewhat tedious to calculate the fundamental matrix (also known as the transmission matrix) $\mathbf{H}(s,x)$ in equation 2.3 by transforming a diagonal matrix of exponentials as in equation 2.9. It is more convenient from the standpoint of control to describe the dynamics in terms of propagation and end effects. The physics of wave propagation and input admittance are understood more readily when the different mechanisms are separated as shown in Fig. 2.2.

As mentioned previously, the matrix $\mathbf{A}$ can be transformed into a diagonal matrix $\mathbf{D}$

$$\mathbf{D} = \mathbf{T}^{-1}\mathbf{A}\mathbf{T} \tag{2.33}$$

with

$$\mathbf{D} = \begin{pmatrix} \lambda_1 & 0 & 0 & 0 \\ 0 & \lambda_2 & 0 & 0 \\ 0 & 0 & \lambda_3 & 0 \\ 0 & 0 & 0 & \lambda_4 \end{pmatrix}. \tag{2.34}$$

Notice that the diagonalized matrix $\mathbf{D}$ is a complex matrix. It is generally more convenient and easier conceptually to deal with real matrices. $\mathbf{D}$ can be transformed into a block diagonal matrix with real components by the transformation

$$\mathbf{D}^* = \mathbf{B}\mathbf{D}\mathbf{B}^{-1} \tag{2.35}$$

which yields

$$\mathbf{D}^* = \left(\frac{p}{2}\right)^{1/2} \begin{pmatrix} 1 & 1 & 0 & 0 \\ -1 & 1 & 0 & 0 \\ 0 & 0 & -1 & 1 \\ 0 & 0 & -1 & -1 \end{pmatrix} \tag{2.36}$$

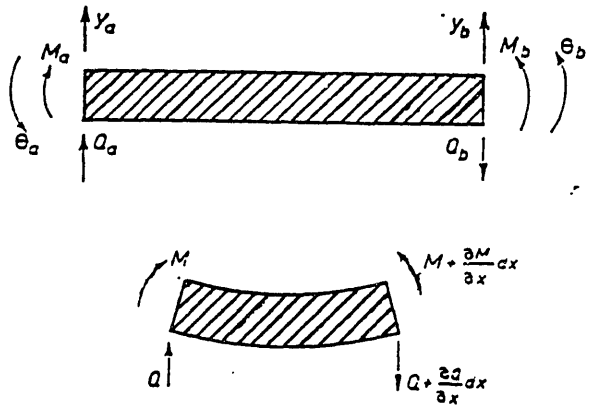

Figure 2.1: Transverse forces, displacements, moments, and angular displacements of a thin-beam and differential element

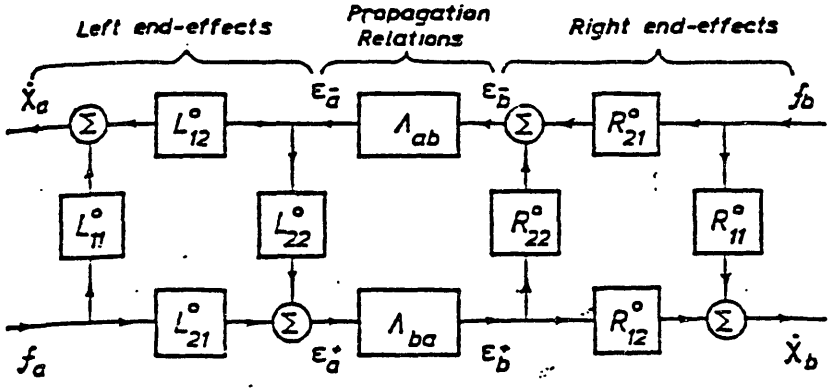

Figure 2.2: Propagation and end-effects relations for transverse vibrations of a free-free beam

where

$$\mathbf{B} = \frac{1}{\sqrt{2}} \begin{pmatrix} 1 & 1 & 0 & 0 \\ j & -j & 0 & 0 \\ 0 & 0 & 1 & 1 \\ 0 & 0 & j & -j \end{pmatrix}$$
$$\mathbf{B}^{-1} = \frac{1}{\sqrt{2}} \begin{pmatrix} 1 & -j & 0 & 0 \\ 1 & j & 0 & 0 \\ 0 & 0 & 1 & -j \\ 0 & 0 & 1 & j \end{pmatrix}. \tag{2.37}$$

The relationship between the original matrix $\mathbf{A}$ and the block diagonal matrix $\mathbf{D}^*$ is

$$\mathbf{A} = \mathbf{T}\mathbf{B}^{-1}\mathbf{D}^*\mathbf{B}\mathbf{T}^{-1} \tag{2.38}$$

which may be expressed as

$$\mathbf{A} = \mathbf{T}^*\mathbf{D}^*\mathbf{T}^{*-1} \tag{2.39}$$

which defines the new transformation matrix $\mathbf{T}^*$;

$$\mathbf{T}^* = \mathbf{T}\mathbf{B}^{-1}. \tag{2.40}$$

This new matrix and its inverse are

$$\mathbf{T}^* = \frac{1}{2} \begin{bmatrix} \sqrt{2}p & 0 & \sqrt{2}p & 0 \\ p^{3/2} & p^{3/2} & -p^{3/2} & p^{3/2} \\ 0 & \sqrt{2}p & 0 & -\sqrt{2}p \\ -p^{3/2} & p^{3/2} & p^{3/2} & p^{3/2} \end{bmatrix}$$
$$\mathbf{T}^{*-1} = \frac{1}{2} \begin{bmatrix} \sqrt{2}p^{-1} & p^{-3/2} & 0 & -p^{-3/2} \\ 0 & p^{-3/2} & \sqrt{2}p^{-1} & p^{-3/2} \\ \sqrt{2}p^{-1} & -p^{-3/2} & 0 & p^{-3/2} \\ 0 & p^{-3/2} & -\sqrt{2}p^{-1} & p^{-3/2} \end{bmatrix}. \tag{2.41}$$

A new state vector $\mathbf{U}$ may be defined by

$$\mathbf{Y} = \mathbf{T}^*\mathbf{U}. \tag{2.42}$$

Plugging equation 2.42 into equation 2.25 along with equation 2.39 yields

$$\frac{d\mathbf{U}}{dx} = \mathbf{D}^*\mathbf{U}. \tag{2.43}$$

This ordinary differential equation may be solved between two points a and b where a represents the end of the beam $x = 0$, and b represents the end of the beam $x = l$. The solution to equation 2.43 between a and b is

$$\mathbf{U}_b(p) = e^{l\mathbf{D}^*}\mathbf{U}_a(p) \tag{2.44}$$

with the matrix exponential a block diagonal matrix

$$e^{l\mathbf{D}^*} = \begin{bmatrix} e^{\sqrt{Lp}}\mathbf{F} & \mathbf{0} \\ \mathbf{0} & e^{-\sqrt{Lp}}\mathbf{F} \end{bmatrix} \tag{2.45}$$

where

$$\mathbf{F} = \begin{bmatrix} \cos\sqrt{Lp} & \sin\sqrt{Lp} \\ -\sin\sqrt{Lp} & \cos\sqrt{Lp} \end{bmatrix}; \quad L = \frac{l^2}{2}. \tag{2.46}$$

Notice that in equation 2.45, the terms containg $e^{\sqrt{Lp}}$ are not analytic as $L \to \infty$ for large s (the semi-infinite condition). These components cannot be admissible transfer functions (this is the same argument which led to the equation of characteristic constraint). By letting

$$\mathbf{U} = \begin{pmatrix} u_1 \\ u_2 \\ u_3 \\ u_4 \end{pmatrix}$$

equation 2.44 can be rearranged so that a matrix of admissible transfer functions is obtained:

$$\begin{matrix} \epsilon_a^- \\ \epsilon_b^+ \end{matrix} \left\{ \begin{pmatrix} u_{1a} \\ u_{2a} \\ u_{3b} \\ u_{4b} \end{pmatrix} \right. = \left(\begin{array}{cc|cc} \overbrace{C(Lp) & -S(Lp)}^{\mathbf{\Lambda}_{ab}} & 0 & 0 \\ S(Lp) & C(Lp) & 0 & 0 \\ \hline 0 & 0 & C(Lp) & S(Lp) \\ 0 & 0 & -S(Lp) & C(Lp) \end{array} \right) \left. \begin{pmatrix} u_{1b} \\ u_{2b} \\ u_{3a} \\ u_{4a} \end{pmatrix} \right\} \begin{matrix} \epsilon_b^- \\ \epsilon_a^+ \end{matrix} \tag{2.47}$$

$\mathbf{\Lambda}_{ba}$

where

$$\begin{aligned} C(Lp) &= \epsilon^{-\sqrt{Lp}}\cos\sqrt{Lp} \\ S(Lp) &= \epsilon^{-\sqrt{Lp}}\sin\sqrt{Lp} \end{aligned}.$$

Equation 2.47 may be written as

$$\begin{pmatrix} \epsilon_a^- \\ \epsilon_b^+ \end{pmatrix} = \begin{pmatrix} \mathbf{\Lambda}_{ab} & 0 \\ 0 & \mathbf{\Lambda}_{ba} \end{pmatrix} \begin{pmatrix} \epsilon_b^- \\ \epsilon_a^+ \end{pmatrix}. \tag{2.48}$$

The symbols ϵ_a, ϵ_b, $\mathbf{\Lambda}_{ab}$, and $\mathbf{\Lambda}_{ba}$ are illustrated in Fig. 2.2. Vaughan [22] names the matrices $\mathbf{\Lambda}_{ab}$ and $\mathbf{\Lambda}_{ba}$ as the Bernoulli-Euler propagation matrices, and he names the operators $C(Lp)$ and $S(Lp)$ propagation operators. It is evident that these matrices and operators describe propagation within the beam and do not include end effects when it is noted that $\mathbf{\Lambda}_{ba}$, which is the transfer function matrix between ϵ_a^+ and ϵ_b^+, is also the transfer function matrix between ϵ_a^+ and $\epsilon_{x=l}^+$ for $l \to \infty$. Thus, the propagation matrices describe propagation within the beam before any end conditions are encountered.

For free-free boundary conditions, equation 2.42 can be rearranged to conform to the definitions of Fig. 2.2:

$$\begin{matrix} \dot{x}_a \\ \epsilon_a^+ \end{matrix} \left\{ \begin{pmatrix} \dot{y} \\ \dot{\theta} \\ u_3 \\ u_4 \end{pmatrix}_a \right. = \left(\begin{array}{cc|cc} \overbrace{1 & \sqrt{2}p^{-1/2}}^{\mathbf{L}_{11}^0} & \overbrace{\sqrt{2}p & -\sqrt{2}p}^{\mathbf{L}_{12}^0} \\ -\sqrt{2}p^{1/2} & -1 & 0 & 2p^{3/2} \\ \hline \sqrt{2}p^{-1} & 2p^{-3/2} & 1 & -2 \\ -\sqrt{2}p^{-1} & 0 & 0 & 1 \\ \underbrace{\qquad\qquad}_{\mathbf{L}_{21}^0} & & \underbrace{\qquad\qquad}_{\mathbf{L}_{22}^0} & \end{array} \right) \left. \begin{pmatrix} m \\ q \\ u_1 \\ u_2 \end{pmatrix}_a \right\} \begin{matrix} f_a \\ \epsilon_a^- \end{matrix} \tag{2.49}$$

$$\begin{matrix} \dot{x}_b \\ \epsilon_b^- \end{matrix} \left\{ \begin{pmatrix} \dot{y} \\ \dot{\theta} \\ u_1 \\ u_2 \end{pmatrix}_b \right. = \left(\begin{array}{cc|cc} \overbrace{1 & -\sqrt{2}p^{-1/2}}^{\mathbf{R}_{11}^0} & \overbrace{\sqrt{2}p & \sqrt{2}p}^{\mathbf{R}_{12}^0} \\ \sqrt{2}p^{1/2} & -1 & 0 & 2p^{3/2} \\ \hline \sqrt{2}p^{-1} & -2p^{-3/2} & 1 & 2 \\ \sqrt{2}p^{-1} & 0 & 0 & 1 \\ \underbrace{\qquad\qquad}_{\mathbf{R}_{21}^0} & & \underbrace{\qquad\qquad}_{\mathbf{R}_{22}^0} & \end{array} \right) \left. \begin{pmatrix} m \\ q \\ u_3 \\ u_4 \end{pmatrix}_b \right\} \begin{matrix} f_b \\ \epsilon_b^+ \end{matrix} \tag{2.50}$$

Equation 2.49 describes the end effects of the left, or a end of a free-free beam, and equation 2.50 describes the end effects of the right, or b end. Equations

2.49, and 2.50 may be written in the short-hand notation

$$\begin{pmatrix} x \\ \epsilon^+ \end{pmatrix}_a = \begin{pmatrix} \mathbf{L}^0_{11} & \mathbf{L}^0_{12} \\ \mathbf{L}^0_{21} & \mathbf{L}^0_{22} \end{pmatrix} \begin{pmatrix} f \\ \epsilon^- \end{pmatrix}_a$$

$$\begin{pmatrix} x \\ \epsilon^- \end{pmatrix}_b = \begin{pmatrix} \mathbf{R}^0_{11} & \mathbf{R}^0_{12} \\ \mathbf{R}^0_{21} & \mathbf{R}^0_{22} \end{pmatrix} \begin{pmatrix} f \\ \epsilon^+ \end{pmatrix}_b$$

Now that the mathematical description of a free-free beam has been separated into propagation and end effects, it is a simple matter to study the effect of an arbitary impedance attached to the end of the beam. In the next section, the effect of attaching a characteristic impedance controller to the right end of the beam is explored.

2.4 End-Point Control of Bending Vibrations

At any point along the length of the beam excepting the end-points, the dynamic variables must conform to the characteristic impedance, equation 2.32. If a controller is attached to the end of the beam, it has its own impedance which in general is different from the characteristic impedance of the beam. A terminal impedance may be attached to the right-hand end of Fig. 2.2 as shown in Fig. 2.3. Through the use of block diagram algebra, the attached impedance block can be incorporated into the free-free end effect blocks as shown in Fig. 2.4. The end-effects relations for the system incorporating a terminal impedance are

$$\begin{aligned} \mathbf{R}_{11} &= [(\mathbf{I} - \mathbf{R}^0_{11}\mathbf{Z}_b)^{-1}\mathbf{R}^0_{11}] \\ \mathbf{R}_{12} &= [(\mathbf{I} - \mathbf{R}^0_{11}\mathbf{Z}_b)^{-1}\mathbf{R}^0_{12}] \\ \mathbf{R}_{21} &= [\mathbf{R}^0_{21}(\mathbf{I} - \mathbf{Z}_b\mathbf{R}^0_{11})^{-1}] \\ \mathbf{R}_{22} &= \mathbf{R}^0_{22} + [\mathbf{R}^0_{21}(\mathbf{I} - \mathbf{Z}_b\mathbf{R}^0_{11})^{-1}\mathbf{Z}_b\mathbf{R}^0_{12}]. \end{aligned} \tag{2.51}$$

A transfer function matrix may be derived from Fig. 2.4:

$$\begin{pmatrix} \dot{x}_a \\ \dot{x}_b \end{pmatrix} = \begin{pmatrix} \mathbf{Y}_{aa} & \mathbf{Y}_{ab} \\ \mathbf{Y}_{ba} & \mathbf{Y}_{bb} \end{pmatrix} \begin{pmatrix} f_a \\ f^*_b - \mathbf{Z}_b\dot{x}^*_b \end{pmatrix} \tag{2.52}$$

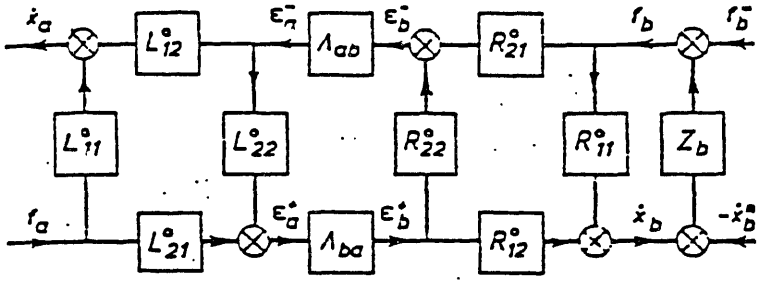

Figure 2.3: Propagation and end-effects relations for free-free beam with terminal impedance appended

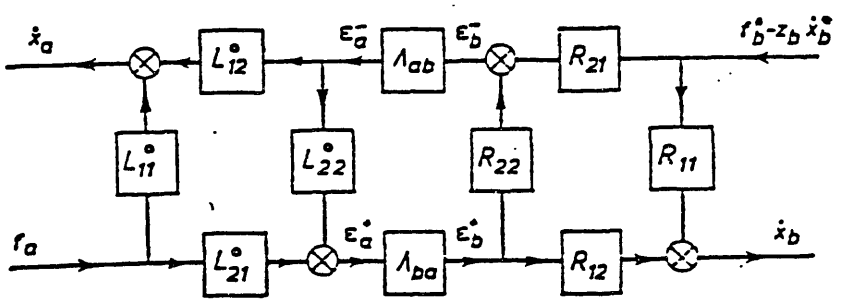

Figure 2.4: Propagation and end-effects relations for beam with terminal impedance incorporated into end-effects

where

$$\begin{aligned}
\mathbf{Y}_{aa}&=\mathbf{L}^0_{11}+\mathbf{L}^0_{12}(\mathbf{I}-\mathbf{\Lambda}_{ab}\mathbf{R}_{22}\mathbf{\Lambda}_{ba}\mathbf{L}^0_{22})^{-1}\mathbf{\Lambda}_{ab}\mathbf{R}_{22}\mathbf{\Lambda}_{ba}\mathbf{L}^0_{21}\\
\mathbf{Y}_{ab}&=\mathbf{L}^0_{12}(\mathbf{I}-\mathbf{\Lambda}_{ab}\mathbf{R}_{22}\mathbf{\Lambda}_{ba}\mathbf{L}^0_{22})^{-1}\mathbf{\Lambda}_{ab}\mathbf{R}_{21}\\
\mathbf{Y}_{ba}&=\mathbf{R}_{12}(\mathbf{I}-\mathbf{\Lambda}_{ba}\mathbf{L}^0_{22}\mathbf{\Lambda}_{ab}\mathbf{R}_{22})^{-1}\mathbf{\Lambda}_{ba}\mathbf{L}^0_{21}\\
\mathbf{Y}_{bb}&=\mathbf{R}_{11}+\mathbf{R}_{12}(\mathbf{I}-\mathbf{\Lambda}_{ba}\mathbf{L}^0_{22}\mathbf{\Lambda}_{ab}\mathbf{R}_{22})^{-1}\mathbf{\Lambda}_{ba}\mathbf{L}^0_{22}\mathbf{\Lambda}_{ab}\mathbf{R}_{21}
\end{aligned} \tag{2.53}$$

By examining Fig. 2.4, it is evident that if $\mathbf{R}_{22}$ could be made identical to $\mathbf{0}$, there would be no reflections of waves propagating from left to right. This describes the behavior of a semi-infinite beam as described in Section 2.2 which suggests the use of the beam's characteristic impedance given by equation 2.32 for a terminal impedance, i.e.:

$$\begin{pmatrix} m \\ q \end{pmatrix}_b = \begin{pmatrix} -G_{\dot{y}} & -G_{\dot{\theta}}\sqrt{2/p} \\ K_{\dot{y}}\sqrt{2p} & K_{\dot{\theta}} \end{pmatrix} \begin{pmatrix} \dot{y}-\dot{y}^* \\ \dot{\theta}-\dot{\theta}^* \end{pmatrix}_b \tag{2.54}$$

where the $*$-ed variables are reference values. In particular, if $\mathbf{Z}_b$ is equal to the characteristic impedance of the beam (i.e., $G_{\dot{y}} = G_{\dot{\theta}} = K_{\dot{y}} = K_{\dot{\theta}} = 1$), then the reflection matrix $\mathbf{R}_{22}$ is identical to the zero matrix which means that no waves are reflected from the right-hand end of the beam. Thus, enforcing the equation of characteristic constraint at the end of the beam does make the beam behave as a semi-infinite beam.

2.5 Boundary Conditions

Equation 2.52 is the transfer function matrix for a distributed parameter beam with the left-hand end free, and the right-hand end terminated with an impedance. The appended impedance may describe a control, or passive end condition (i.e. pinned, clamped, sliding, etc.), or both. For a more general description of a beam, terminal impedances may be appended to both ends of the beam model so that Equation 2.53 becomes

$$\begin{aligned}
\mathbf{Y}_{aa}&=\mathbf{L}_{11}+\mathbf{L}_{12}(\mathbf{I}-\mathbf{\Lambda}_{ab}\mathbf{R}_{22}\mathbf{\Lambda}_{ba}\mathbf{L}_{22})^{-1}\mathbf{\Lambda}_{ab}\mathbf{R}_{22}\mathbf{\Lambda}_{ba}\mathbf{L}_{21}\\
\mathbf{Y}_{ab}&=\mathbf{L}_{12}(\mathbf{I}-\mathbf{\Lambda}_{ab}\mathbf{R}_{22}\mathbf{\Lambda}_{ba}\mathbf{L}_{22})^{-1}\mathbf{\Lambda}_{ab}\mathbf{R}_{21}\\
\mathbf{Y}_{ba}&=\mathbf{R}_{12}(\mathbf{I}-\mathbf{\Lambda}_{ba}\mathbf{L}_{22}\mathbf{\Lambda}_{ab}\mathbf{R}_{22})^{-1}\mathbf{\Lambda}_{ba}\mathbf{L}_{21}\\
\mathbf{Y}_{bb}&=\mathbf{R}_{11}+\mathbf{R}_{12}(\mathbf{I}-\mathbf{\Lambda}_{ba}\mathbf{L}_{22}\mathbf{\Lambda}_{ab}\mathbf{R}_{22})^{-1}\mathbf{\Lambda}_{ba}\mathbf{L}_{22}\mathbf{\Lambda}_{ab}\mathbf{R}_{21}
\end{aligned} \tag{2.55}$$

with

$$\begin{aligned}
\mathbf{L}_{11}&=[(\mathbf{I}-\mathbf{L}^0_{11}\mathbf{Z}_a)^{-1}\mathbf{L}^0_{11}]\\
\mathbf{L}_{12}&=[(\mathbf{I}-\mathbf{L}^0_{11}\mathbf{Z}_a)^{-1}\mathbf{L}^0_{12}]\\
\mathbf{L}_{21}&=[\mathbf{L}^0_{21}(\mathbf{I}-\mathbf{Z}_a\mathbf{L}^0_{11})^{-1}]\\
\mathbf{L}_{22}&=\mathbf{L}^0_{22}+[\mathbf{L}^0_{21}(\mathbf{I}-\mathbf{Z}_a\mathbf{L}^0_{11})^{-1}\mathbf{Z}_a\mathbf{L}^0_{12}].
\end{aligned} \tag{2.56}$$

Using this approach, the transfer function matrix may be found for a variety of beam configurations.

2.5.1 Clamped-Free Beam

One of the cases studied in this paper is the clamped free beam. This case is of particular interest because since both linear and angular velocity is present at the beam's end, the full end point impedance controller may be implemented. The clamped-free condition may be implemented with a cantilever beam with the left end clamped, and the right end free, as shown in Fig. 2.5. The geometric boundary conditions at the left-hand end are $y(t) = 0$ and $\theta(t) = 0$. These boundary conditions can be plugged into equation 2.42 to yield

$$\begin{pmatrix} 0 \\ 0 \\ m \\ q \end{pmatrix}_a = \begin{pmatrix} \frac{\sqrt{2}}{2}p(u_1+u_3) \\ \frac{p^{3/2}}{2}(u_1+u_2-u_3+u_4) \\ \frac{\sqrt{2}}{2}p(u_2-u_4) \\ \frac{p^{3/2}}{2}(-u_1+u_2+u_3+u_4) \end{pmatrix}_a \tag{2.57}$$

which may be solved to eliminate m and q:

$$\epsilon_a^+ \left\{ \begin{pmatrix} u_3 \\ u_4 \end{pmatrix}_a = \begin{bmatrix} -1 & 0 \\ -2 & -1 \end{bmatrix} \begin{pmatrix} u_1 \\ u_2 \end{pmatrix}_a \right\} \epsilon_a^-. \tag{2.58}$$

By examining equation 2.49, it is seen that equation 2.58 is in the form $\epsilon_a^+ = \mathbf{L}_{22}\epsilon_a^-$. $\mathbf{L}_{11}$, $\mathbf{L}_{12}$, and $\mathbf{L}_{21}$ are all equal to $\mathbf{0}$. Plugging these values of $\mathbf{L}_{ij}$, and $\mathbf{R}_{ij} = \mathbf{R}^0_{ij}$ into equation 2.55, the transfer function matrices for the clamped-free beam configuration are

$$\begin{aligned}
\mathbf{Y}_{aa}&=0\\
\mathbf{Y}_{ab}&=0\\
\mathbf{Y}_{ba}&=0\\
\mathbf{Y}_{bb}&=\mathbf{R}^0_{11}+\mathbf{R}^0_{12}(\mathbf{I}-\mathbf{\Lambda}_{ba}\mathbf{L}_{22}\mathbf{\Lambda}_{ab}\mathbf{R}^0_{22})^{-1}\mathbf{\Lambda}_{ba}\mathbf{L}_{22}\mathbf{\Lambda}_{ab}\mathbf{R}^0_{21}.
\end{aligned} \tag{2.59}$$

The transfer function matrix $\mathbf{Y}_{bb}$ is a 2×2 matrix of transfer functions and may be written as

$$\mathbf{Y}_{bb} = \begin{pmatrix} \mathbf{Y}_{bb}(1,1) & \mathbf{Y}_{bb}(1,2) \\ \mathbf{Y}_{bb}(2,1) & \mathbf{Y}_{bb}(2,2) \end{pmatrix} \tag{2.60}$$

Using the values for the $\mathbf{R}_{ij}^0$ from equation 2.50, and the value of $\mathbf{L}_{22}$ from equation 2.58, the elements of the transfer function matrix $\mathbf{Y}_{bb}$ can be calculated:

$$\mathbf{Y}_{bb}(1,1) = \frac{(S^2 + C'^2)^2 + 2S^2 - 2C'^2 + 1}{(S^2 + C'^2)^2 + 2S^2 + 6C'^2 + 1} \tag{2.61}$$

$$\mathbf{Y}_{bb}(1,2) = \sqrt{\frac{2}{p}} \frac{(S^2 + C'^2)^2 + 4SC' - 1}{(S^2 + C'^2)^2 + 2S^2 + 6C'^2 + 1} \tag{2.62}$$

$$\mathbf{Y}_{bb}(2,1) = -\sqrt{2p} \frac{(S^2 + C'^2)^2 - 4SC' - 1}{(S^2 + C'^2)^2 + 2S^2 + 6C'^2 + 1} \tag{2.63}$$

$$\mathbf{Y}_{bb}(2,2) = -\frac{(S^2 + C'^2)^2 + 2S^2 - 2C'^2 + 1}{(S^2 + C'^2)^2 + 2S^2 + 6C'^2 + 1} \tag{2.64}$$

where

$$\begin{matrix} S \equiv S(Lp) \equiv e^{-\sqrt{Lp}} \sin\sqrt{Lp} \\ C \equiv C'(Lp) \equiv e^{-\sqrt{Lp}} \cos\sqrt{Lp} \end{matrix}, \quad L = \frac{l^2}{2}$$

The above transfer functions model the behavior of a clamped-free beam and include all modes. The approximation of these transfer functions is discussed in Chapter 3.

2.5.2 Clamped-Sliding Beam

A beam configuration which may be used to model a Remote Center Compliance is a clamped-sliding beam configuration. As shown in Fig. 2.6 the left-hand boundary conditions are the same as that for a clamped-free beam, but at the right-hand end, $\theta(t) = 0$. These boundary conditions can be plugged into equation 2.42 to yield

$$\begin{pmatrix} \dot{y} \\ 0 \\ m \\ q \end{pmatrix}_b = \begin{pmatrix} \frac{\sqrt{2}}{2} p(u_1 + u_3) \\ \frac{p^{3/2}}{2}(u_1 + u_2 - u_3 + u_4) \\ \frac{\sqrt{2}}{2} p(u_2 - u_4) \\ \frac{p^{3/2}}{2}(-u_1 + u_2 + u_3 + u_4) \end{pmatrix}_b \tag{2.65}$$

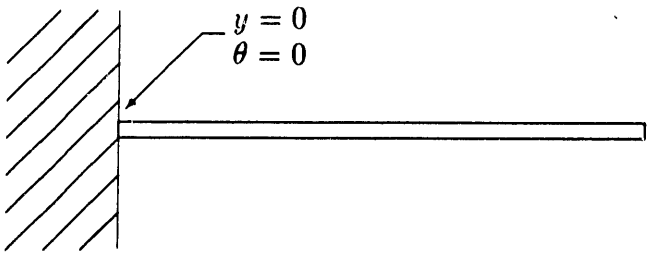

Figure 2.5: Clamped-Free beam configuration

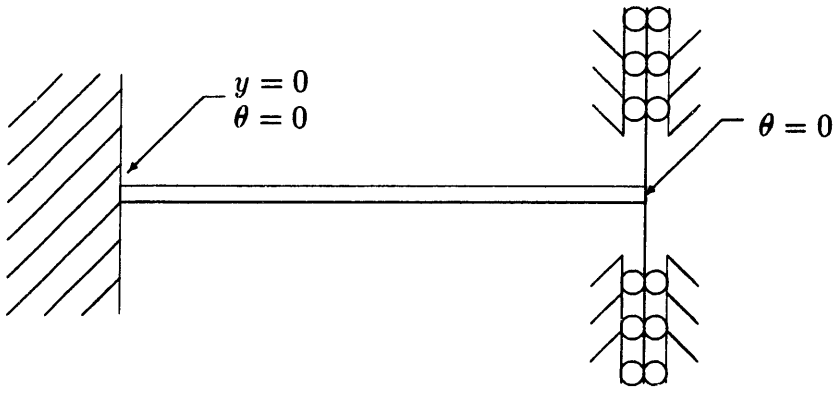

Figure 2.6: Clamped-sliding beam configuration

which may be rearranged to form

$$\begin{pmatrix} \dot{y} \\ \dot{\theta} \\ u_1 \\ u_2 \end{pmatrix}_b = \left(\begin{array}{cc|cc} 0 & -\frac{\sqrt{2}}{2}p^{-1/2} & \sqrt{2}p & 0 \\ 0 & 0 & 0 & 0 \\ \hline 0 & -p^{-3/2} & 1 & 0 \\ 0 & p^{-3/2} & 0 & -1 \end{array}\right) \begin{pmatrix} m \\ q \\ u_3 \\ u_4 \end{pmatrix}_b . \qquad (2.66)$$

$\mathbf{R}_{11}$ $\mathbf{R}_{12}$ $\mathbf{R}_{21}$ $\mathbf{R}_{22}$

Plugging these values of $\mathbf{R}_{ij}$ along with the value of $\mathbf{L}_{22}$ into equation 2.55, the transfer function matrices may be calculated. As in the clamped-free case, $\mathbf{Y}_{aa} = \mathbf{Y}_{ab} = \mathbf{Y}_{ba} = \mathbf{0}$. The transfer function matrix relating output to input at the right hand end is

$$\mathbf{Y}_{bb} = \mathbf{R}_{11} + \mathbf{R}_{12}(\mathbf{I} - \mathbf{\Lambda}_{ba}\mathbf{L}_{22}\mathbf{\Lambda}_{ab}\mathbf{R}_{22})^{-1}\mathbf{\Lambda}_{ba}\mathbf{L}_{22}\mathbf{\Lambda}_{ab}\mathbf{R}_{21} \qquad (2.67)$$

which may be expanded into its four component transfer functions. In this case of a clamped-sliding configuration, $\mathbf{Y}_{bb}(1,1) = \mathbf{Y}_{bb}(2,1) = \mathbf{Y}_{bb}(2,2) = 0$ and

$$\mathbf{Y}_{bb}(1,2) = \sqrt{\frac{1}{2p}}\frac{(S^2+C^2)^2 - 6S^2 - 2C^2 + 1}{(S^2+C^2)^2 - 4SC - 1} \qquad (2.68)$$

where

$$\begin{array}{l} S \equiv S(Lp) \equiv \epsilon^{-\sqrt{Lp}} \sin\sqrt{Lp} \\ C \equiv C(Lp) \equiv \epsilon^{-\sqrt{Lp}} \cos\sqrt{Lp} \end{array}, \quad L = \frac{l^2}{2}.$$

This is the transfer function between a force input, and linear velocity output at the right hand end. Because of the $\theta(t) = 0$ constraint, an applied moment has no effect, and an applied force does not induce a rotation.

The approximation of the transfer function for the clamped-sliding beam will be discussed in the next chapter.

Chapter 3

Dynamic Simulation

3.1 Approximating Infinite-Order Systems

Models for distributed parameter systems describe infinite order systems as opposed to lumped parameter systems which are modeled with a finite number of energy storage elements. If a closed-form, time-domain solution of the system transfer function matrix 2.52 can be found, then the theoretical time response can be calculated exactly. However, a closed-form, time-domain solution may be impossible to find. Therefore, an approximation of the time-domain response is sought.

As an example, equation 2.52 is the transfer function matrix for a free-free beam with a controller attached to the right-hand end. The third of equation 2.53, $\mathbf{Y}_{ba}$, is a transfer function matrix of the velocity outputs of the right-hand end of the beam to the disturbance force and moment of the left-hand end of the beam. The elements of $\mathbf{Y}_{ba}$ may be written as:

$$\mathbf{Y}_{ba}(1,1) = \frac{4S(S^2+C^2-1)}{(S^2+C^2)^2-6S^2-2C^2+1} \tag{3.1}$$

$$\mathbf{Y}_{ba}(1,2) = -2\sqrt{\frac{2}{p}}\frac{(S+C)(S^2+C^2)+(S-C)}{(S^2+C^2)^2-6S^2-2C^2+1} \tag{3.2}$$

$$\mathbf{Y}_{ba}(2,1) = 2\sqrt{2p}\frac{(S-C)(S^2+C^2)+(S+C)}{(S^2+C^2)^2-6S^2-2C^2+1} \tag{3.3}$$

$$\mathbf{Y}_{ba}(2,2) = \frac{4S(S^2+C^2-1)}{(S^2+C^2)^2-6S^2-2C^2+1} \tag{3.4}$$

where

$$S=S(Lp)=\epsilon^{-\sqrt{Lp}}\sin\sqrt{Lp} \quad , \quad L=\frac{l^2}{2}.$$
$$C=C(Lp)=\epsilon^{-\sqrt{Lp}}\cos\sqrt{Lp}$$

These transfer functions are transcendental and have infinitely many poles and zeros. A closed form solution of these transfer functions via the inverse laplace transform was not attempted. Instead, a Padé type approximation was made to create a polynomial transfer function. The approximation was made by first constructing a Bode plot of the transcendental transfer function. By way of example, the beam used by Vaughan [22] is used to demonstrate the digital simulation of a free-free beam. The parameters for this example beam are given in Table 3.1. A Bode plot for $\mathbf{Y}_{bn}(2,2)$ using these parameters is shown in Fig. 3.1. The first five poles and zeros as well as the appropriate gain were then estimated from the Bode plot. A more precise estimate was obtained with the use of a zero-finding IMSL routine(ZANLYT). The first five pairs of poles and zeros were estimated and are shown in Table 3.2. The estimated poles, zeros, and gain were then combined to form a transfer function of the form

$$\mathbf{Y}_{bn}(2,2)=\frac{\text{Gain}\left((s/z_1)^2+1\right)\left((s/z_2)^2+1\right)\cdots\left((s/z_5)^2+1\right)}{s\left((s/p_1)^2+1\right)\left((s/p_2)^2+1\right)\cdots\left((s/p_5)^2+1\right)} \tag{3.5}$$

which could then be converted into a conventional state-space representation. A comparison of the Bode plots of the approximated transfer function and the original transfer function is shown in Fig. 3.2. The fidelity of the approximation is excellent up to the third mode, after which the approximated transfer function rolls off in magnitude. The approximation is expected to roll off in the higher frequency range because the approximation is only for the first five modes. However, there was more attenuation at the fourth and fifth mode than was expected. This does not really cause any problems because for the cases studied, these higher modes contribute only a small amount to the velocity signals and are well damped.

The time domain solution of the approximated system may be easily solved for an arbitrary input using comercially availabel software packages such as CTRL-C or PC-MATLAB. Fig. 3.3 shows the response of $\dot{\theta}_b$ to a ten pound step in Q_n for an uncontrolled free-free beam. The fractional operators used in the controller were also approximated using a Padé type approximation. The method used to derive the approximation differs from that used above for finding

Length (l)	200 in.
Cross-section area (A)	1.0 in.^{2}
Young's modulus (E)	$30 \times 10^6 \frac{\text{lb}}{\text{in.}^2}$
Density (ρ)	$0.725 \times 10^{-3} \frac{\text{lb-sec}^2}{\text{in.}^4}$
Area moment of inertia (I)	0.0796 in.^{4}
$a = \sqrt{EI/(\rho A)}$	$57.5 \times 10^3 \frac{\text{in.}^2}{\text{sec}}$
EI/a	$41.5 \frac{\text{in.-lb}}{(\text{in./sec})}$

Table 3.1: Example beam parameters

Gain $= -.4589$

Poles	*Zeros*
0	
$\pm 32.16i$	± 28.40
$\pm 88.65i$	± 113.5
$\pm 173.8i$	± 255.4
$\pm 287.3i$	± 454.0
$\pm 429.2i$	± 709.4

Table 3.2: Poles, Zeros, and Gain for $\mathbf{Y}_{ba}(2,2)$

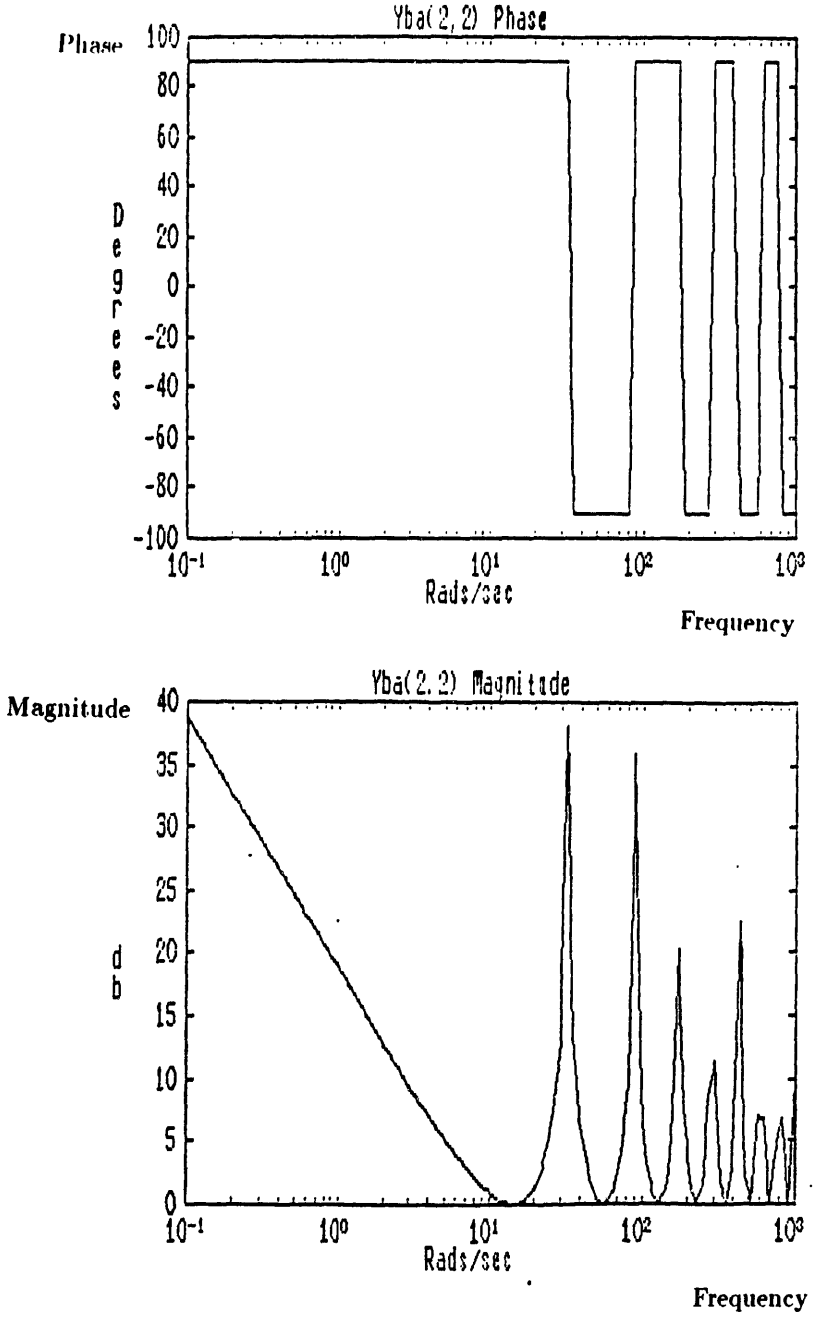

Figure 3.1: Bode plot of $\mathbf{Y}_{ba}(2,2)$

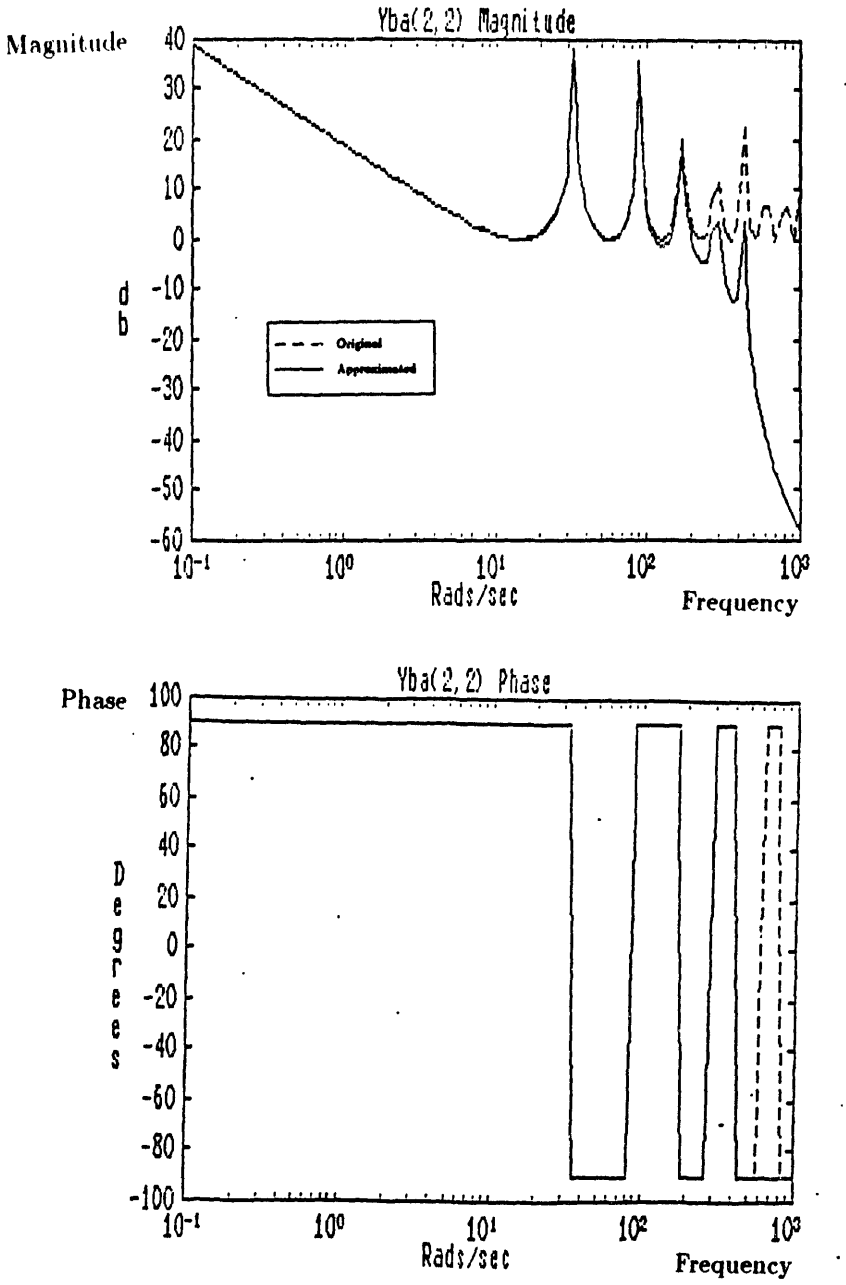

Figure 3.2: Comparison of original and approximated $\mathbf{Y}_{ba}$

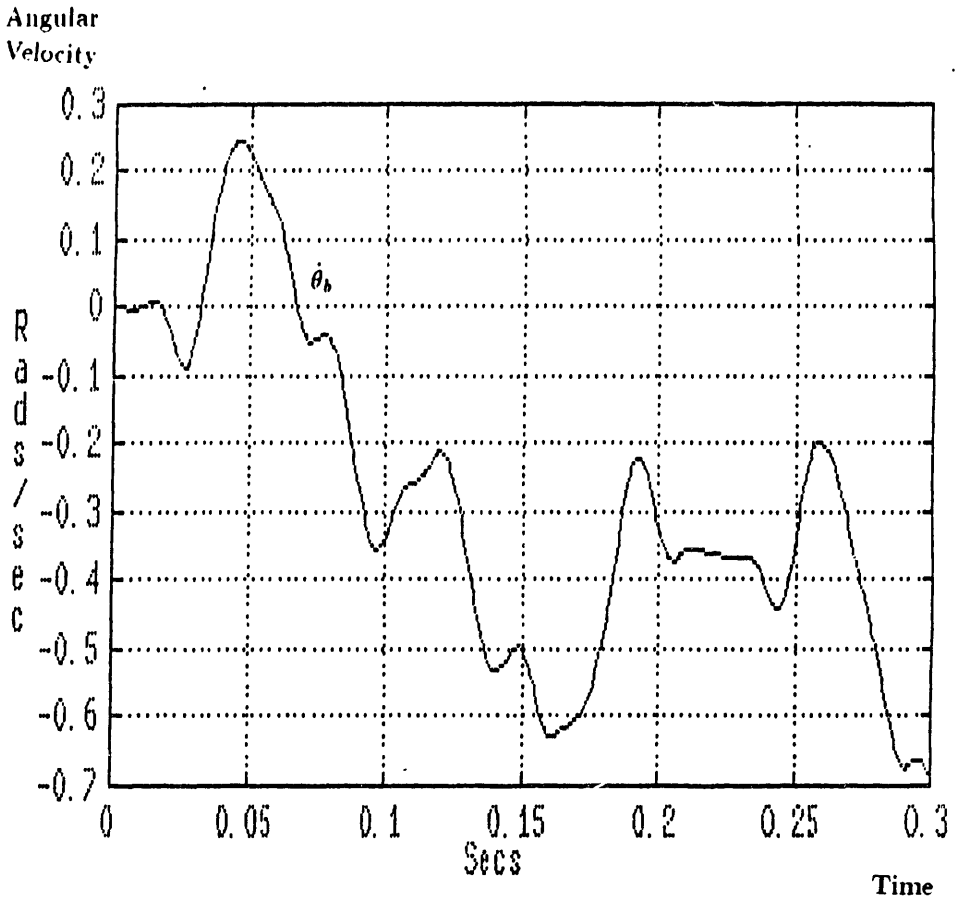

Figure 3.3: Response of $\dot{\theta}_b$ to step input in Q_a

approximations for the system transfer functions. Appendix A describes the approximation of the fractional operators.

3.2 Control Simulation of Free-free Beam

Using the model developed in the previous section, the effects of the controller of equation 2.54 may be included. A block diagram of the free-free beam with the controller attached is shown in Fig. 3.4. The blocks for $Y_{ba}(1,2)$, $Y_{ba}(2,2)$, $Y_{bb}(1,2)$, and $Y_{bb}(2,2)$ were implemented digitally using forward integration (Adams-Bashford)[20]. The blocks for $Y_{bb}(1,1)$ and $Y_{bb}(2,1)$ were implemented using *backward Euler* integration due to the "stiffness" of those transfer functions(see Appendix B). A software package such as TUTSIM allows seperate blocks to be linked together easily. By adjusting the values of the coefficients $G_{\dot{y}}$, $G_{\dot{\theta}}$, $K_{\dot{y}}$, and $K_{\dot{\theta}}$, different control configurations can be formed. By letting these coefficients be all equal to 1, the controller takes on the form of the beams characteristic impedance, as described in Section 2.4. Fig. 3.5 shows the time response of the free-free beam with the same conditions as for the response shown in Fig. 3.3.

3.3 Simulation of Clamped-free Beam

The first beam configuration used for experimentation described in the next chapter is the clamped-free beam. The parameters used for the simulation are given in Table 3.3. Fig. 3.6 shows the block diagram for a clamped-free beam configuration including the controller. The blocks $Y_{bb}(1,1)$ and $Y_{bb}(2,1)$ were implemented using backward integration due to the stiffness of the system. Fig. 3.7 shows the uncontrolled time response (controller gains set to zero) of the beam's linear tip velocity to the force pulse shown in Fig. 3.8, which approximates the pulse imparted to the beam by an impact hammer. The plot in Fig. 3.7 is the response to a pulse input with a peak force of ten pounds, and a duration of three milliseconds.

By setting the appropriate gains to zero in the controller matrix (equation 2.54), several different controllers can be constructed. By setting $K_{\dot{\theta}} = 1$, for example, and the other three gains to zero ($K_{\dot{\theta}}$ control), the same input

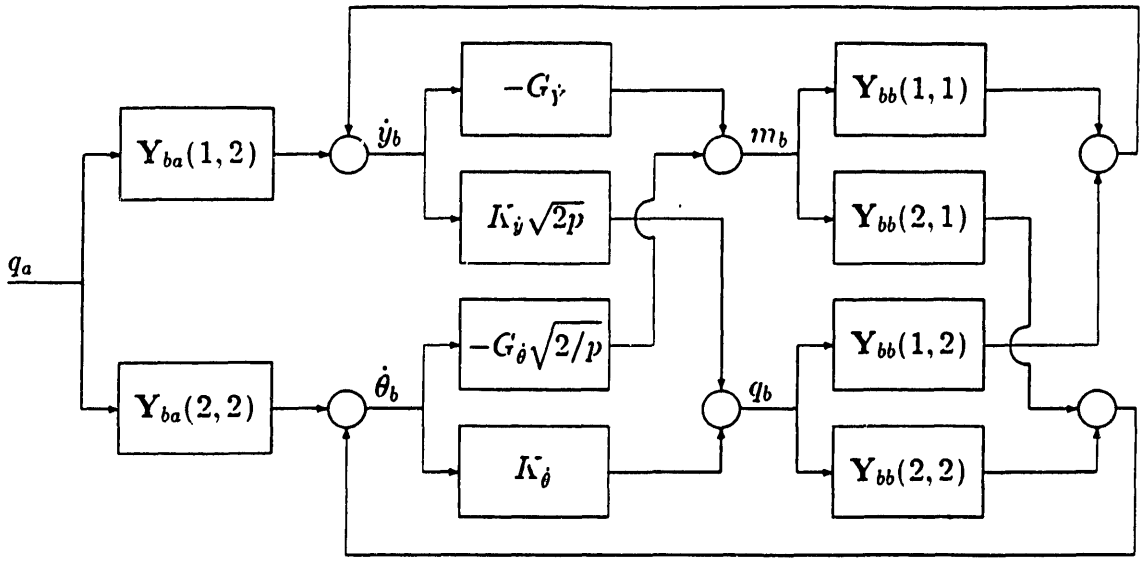

Figure 3.4: Free-free beam with controller: block diagram

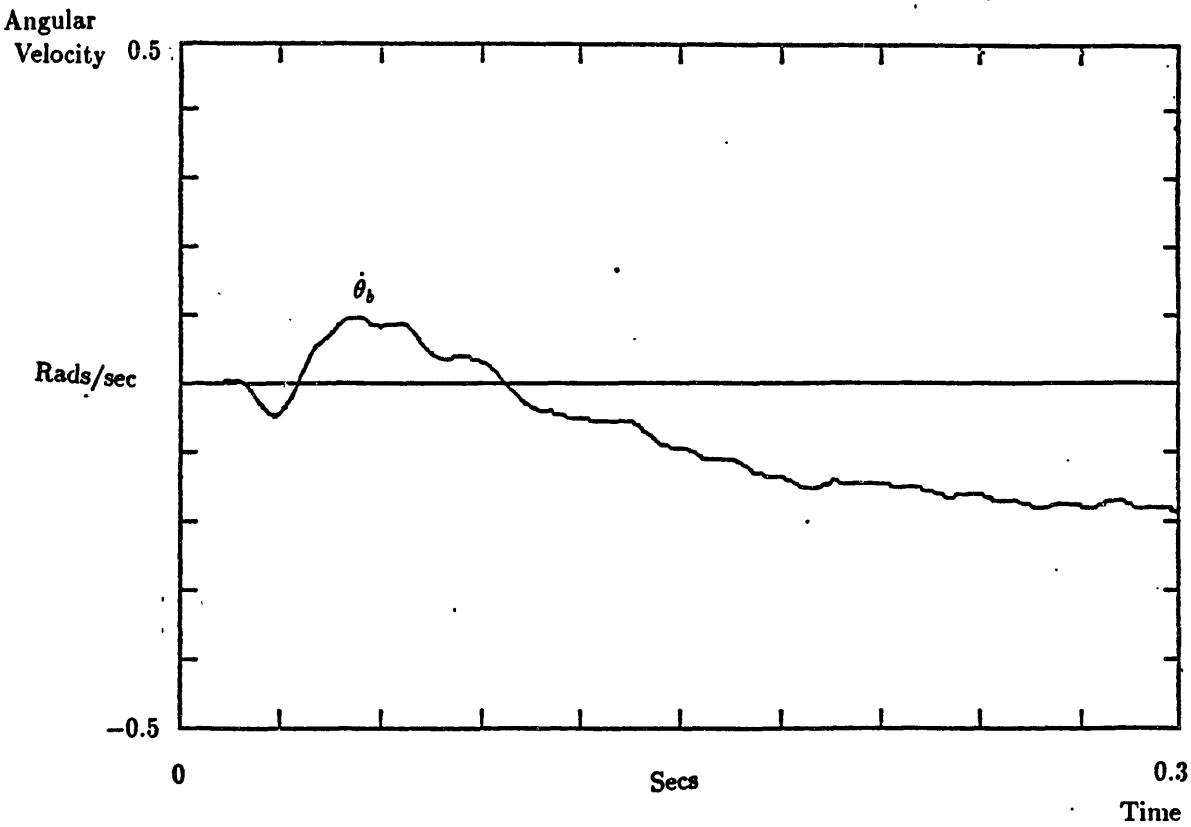

Figure 3.5: Response of free-free beam with controller attached

Length (l)	52 in.
Cross-section area (A)	0.75 in.^{2}
Young's modulus (E)	$11 \times 10^6 \frac{\text{lb}}{\text{in.}^2}$
Density (ρ)	$0.266 \times 10^{-3} \frac{\text{lb-sec}^2}{\text{in.}^4}$
Area moment of inertia (I)	0.976×10^{-3} in.^{4}
$a = \sqrt{EI/(\rho A)}$	$7.35 \times 10^3 \frac{\text{in.}^2}{\text{sec}}$
EI/a	$1.467 \frac{\text{in.-lb}}{(\text{in./sec})}$

Table 3.3: Clamped-free beam parameters

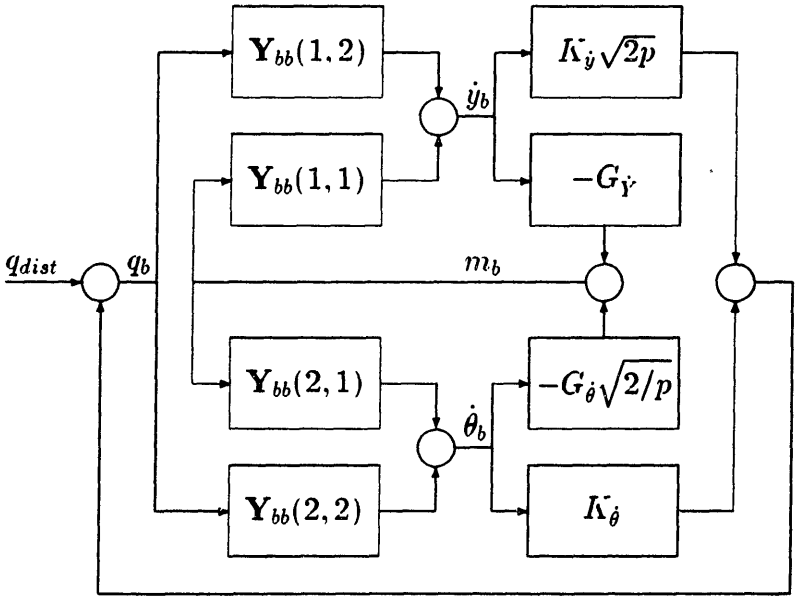

Figure 3.6: Block diagram for clamped-free beam

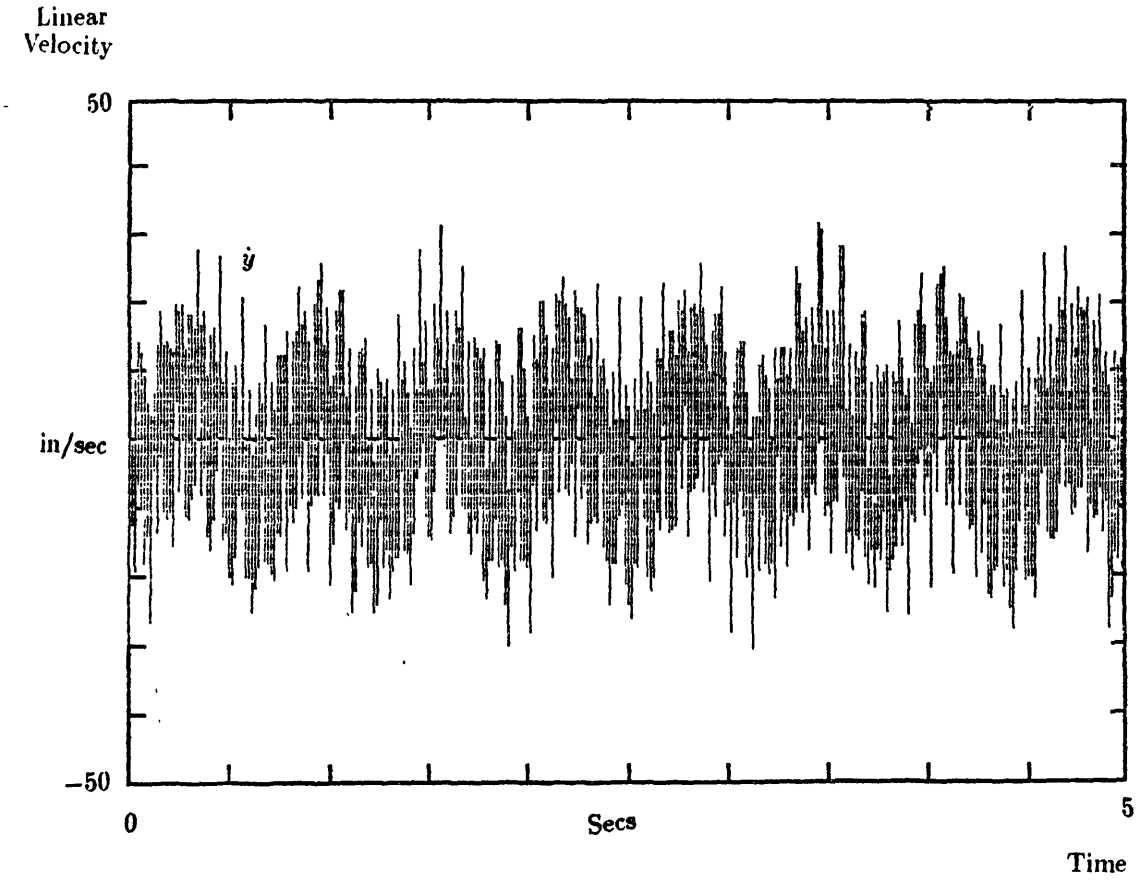

Figure 3.7: Linear velocity response to force input: uncontrolled

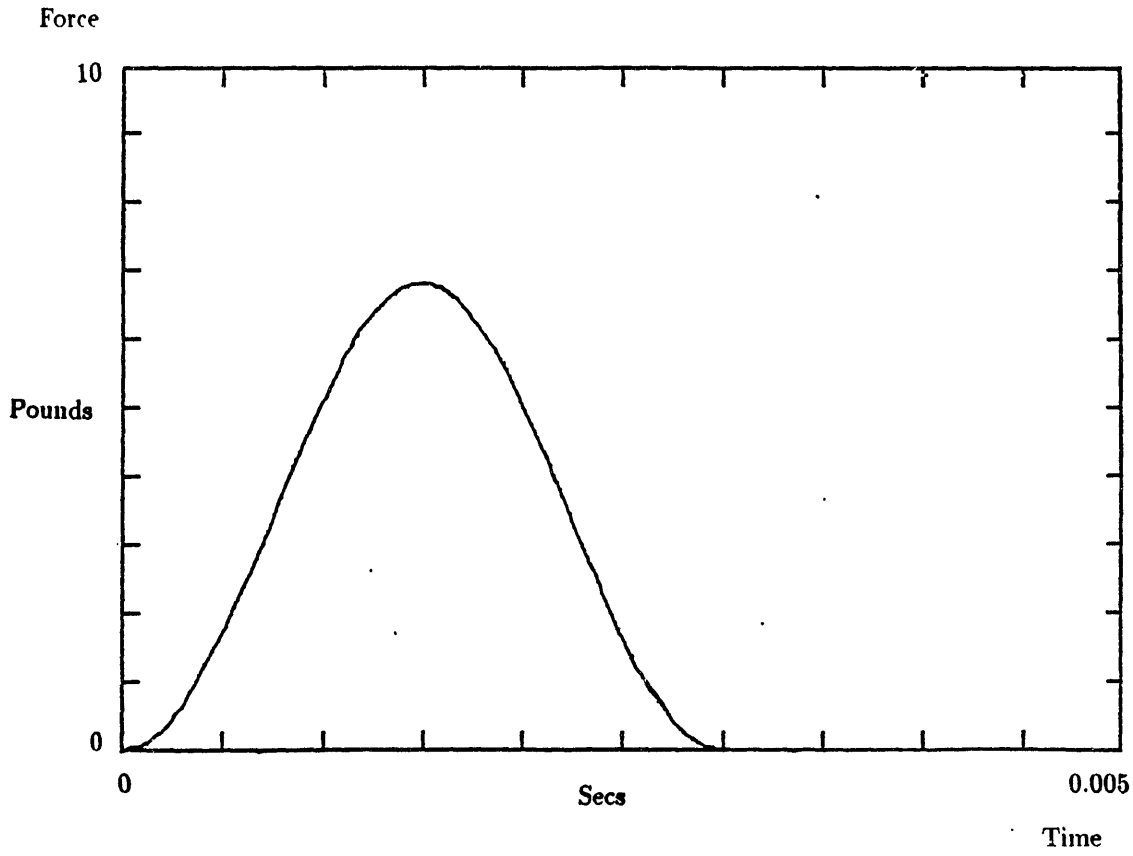

Figure 3.8: Force pulse input

used for Fig. 3.7 produces the response shown in Fig. 3.9. With $K_{\dot{\theta}} = K_{\dot{y}} = 1$ and the other two gains equal to zero(K control), the response becomes that shown in Fig. 3.10. Fig. 3.11 shows the response of the clamped-free beam with a characteristic impedance controller (all gains set to 1 (Z control)).

3.4 Simulation of Clamped-Sliding Beam

The beam configuration which emulates the motion of the Remote Center Compliance is the clamped-sliding beam. The results of Chapter 2 show that there is a single transfer function for a clamped-sliding beam, $Y_{bb}(1,2)$, which is the transfer function between a force input and linear velocity output. A set of parameters consistent with the beam used for experiments is summarized in Table 3.4. A simulation of the response of a clamped-sliding beam to a pulse input (8.5 pound peak force) is shown in Fig. 3.12.

Because of the absence of any angular motion at the tip of a clamped-sliding beam, it is not possible to implement the complete control law Equation 2.54. The only element that can do any work is $K_{\dot{y}}\sqrt{2p}$ so that the control law for a clamped sliding beam is

$$q_b = K_{\dot{y}}\sqrt{2p}\dot{y} \tag{3.6}$$

Using $K_{\dot{y}} = 1$, the uncontrolled simulation of Fig. 3.12 is transformed into Fig. 3.13. Even without the full impedance controller, it is possible to do effective disturbance rejection for the clamped-free case.

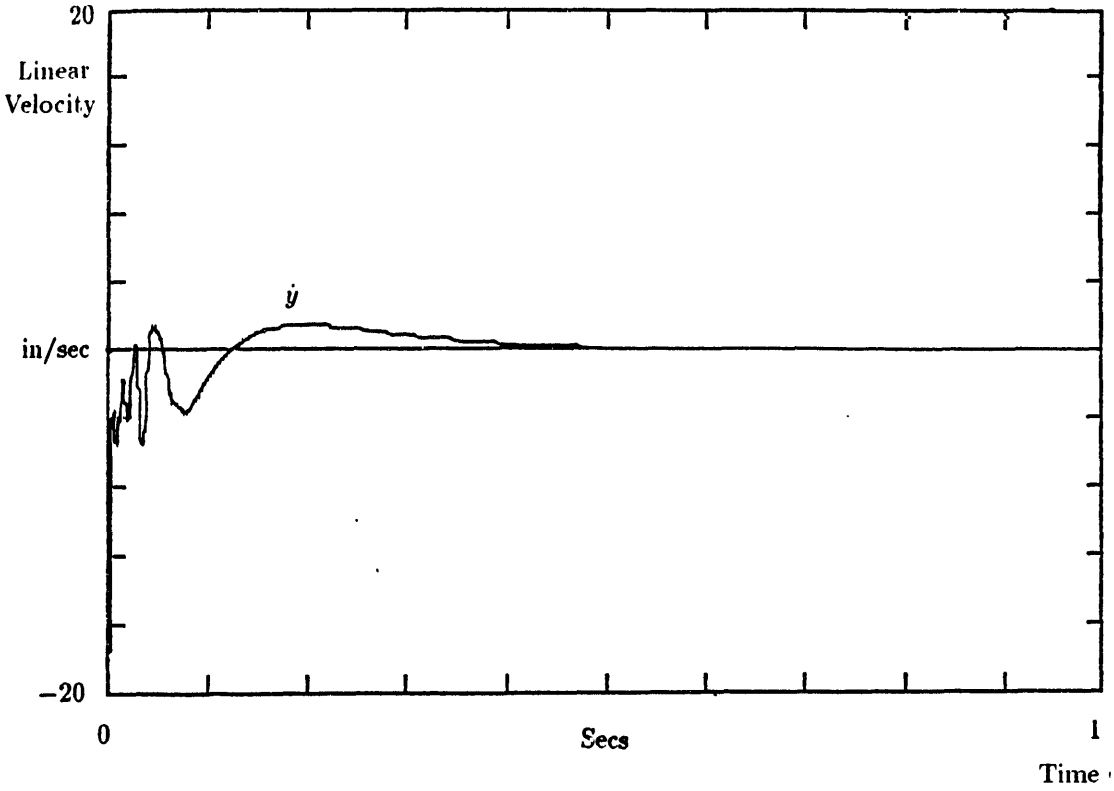

Figure 3.9: Clamped-free beam with $K_{\dot{\theta}}$ control

Length (l)	10.75 in.
Cross-section area (A)	0.02 in.^{2}
Young's modulus (E)	$30 \times 10^6 \frac{\text{lb}}{\text{in.}^2}$
Density (ρ)	$0.725 \times 10^{-3} \frac{\text{lb-sec}^2}{\text{in.}^4}$
Area moment of inertia (I)	0.667×10^{-6} in.^{4}
$a = \sqrt{EI/(\rho A)}$	$1.18 \times 10^3 \frac{\text{in.}^2}{\text{sec}}$
EI/a	$.0172 \frac{\text{in.-lb}}{(\text{in./sec})}$

Table 3.4: Clamped-sliding beam parameters

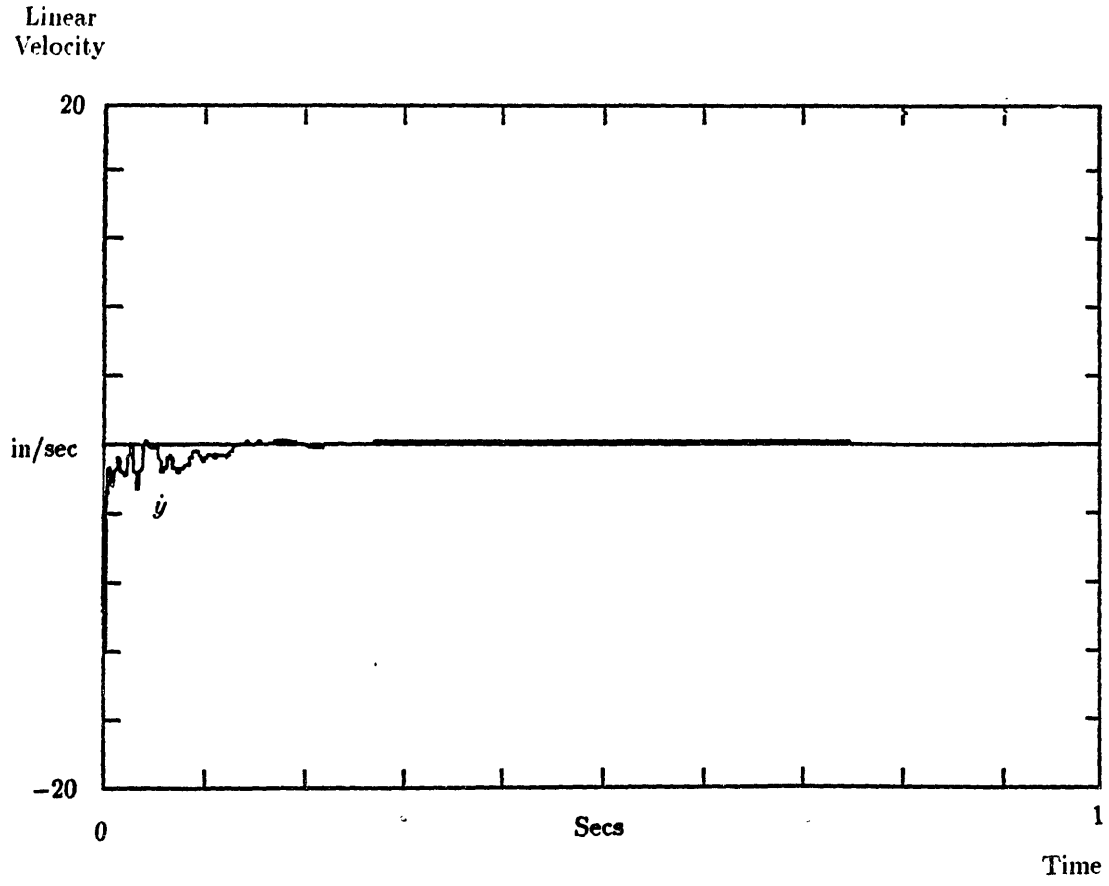

Figure 3.10: Clamped-free beam with K control

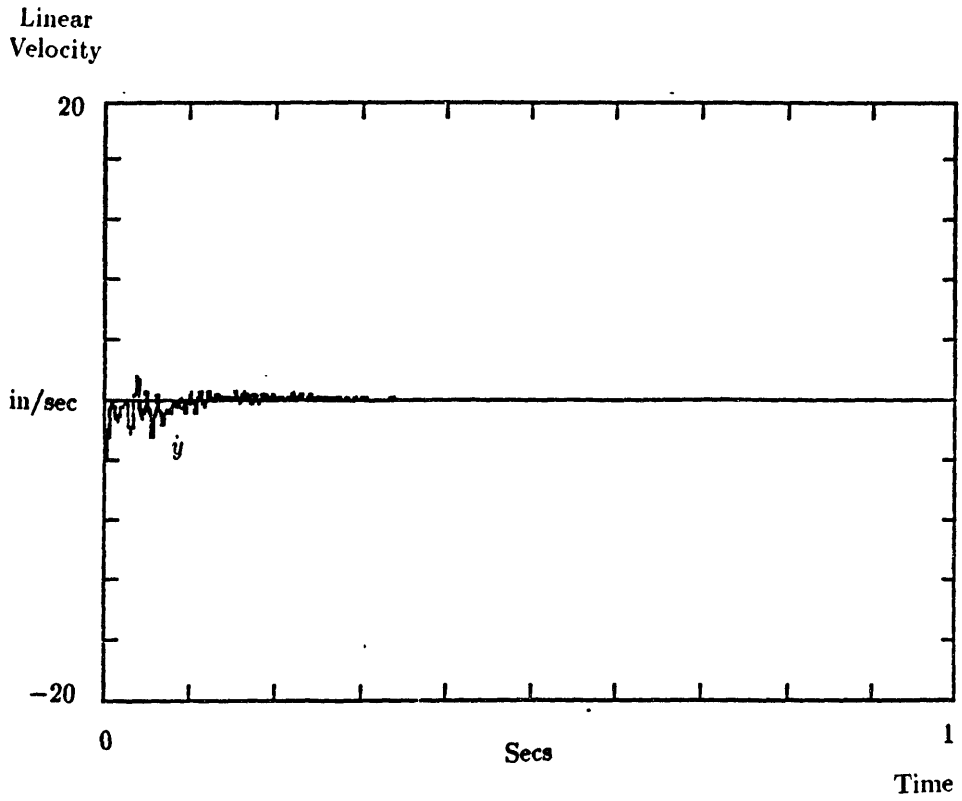

Figure 3.11: Clamped-free beam with Z control

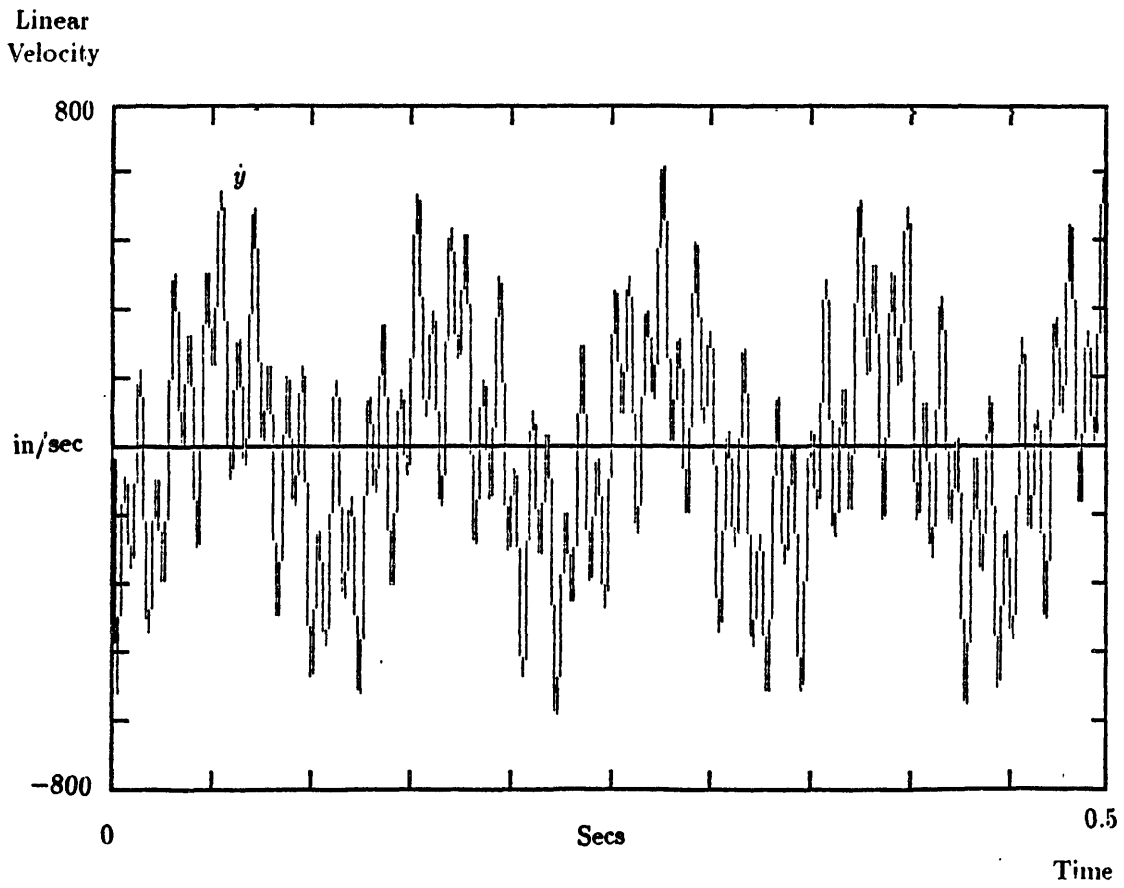

Figure 3.12: Uncontrolled response of clamped-sliding beam to pulse input

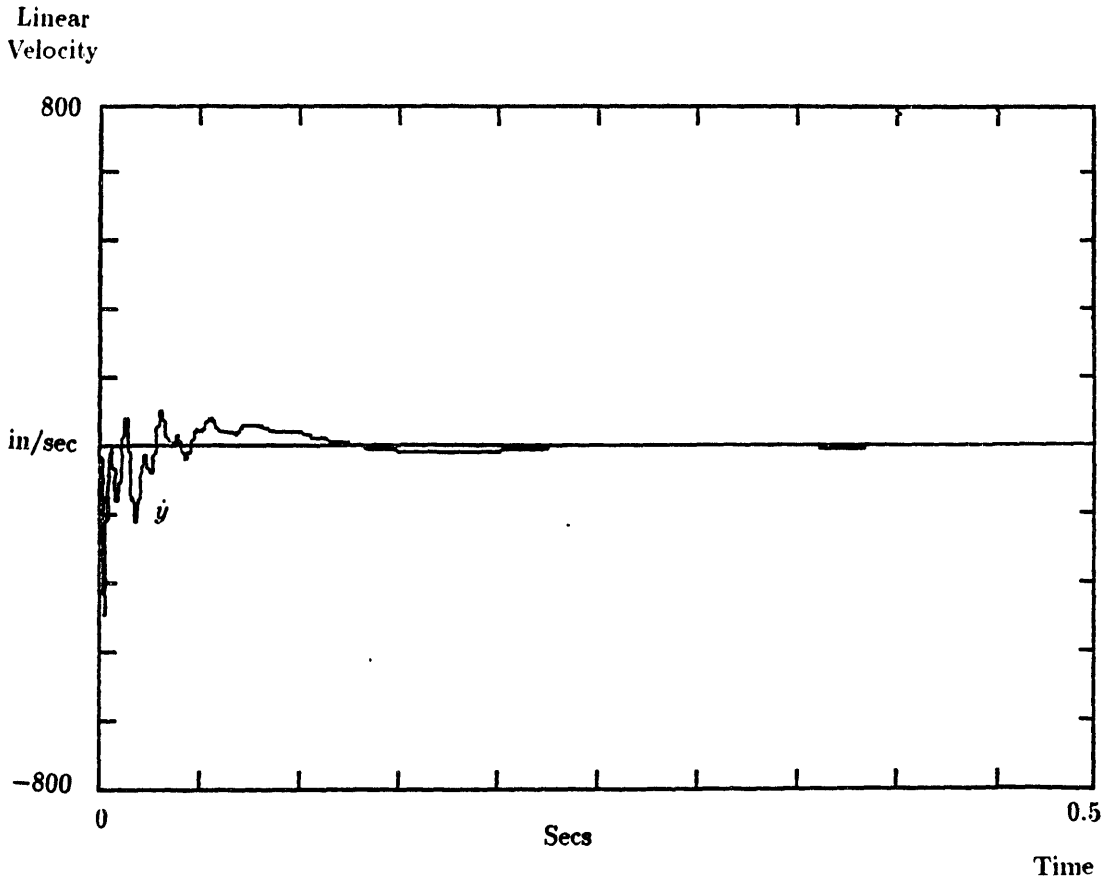

Figure 3.13: Clamped-sliding beam with $K_{\dot{y}}$ controller

Chapter 4

Experimental Analysis

In order to study the effects of the end point impedance controller, two experiments were conducted: a clamped-free beam experiment so that all four elements of the impedance controller could be implemented; and a clamped-sliding beam experiment so that the active damping of a Remote Center Compliance model could be demonstrated. The two experiments required seperate setups which will be described individually.

4.1 Clamped-free Beam

4.1.1 Experimental Setup

The parameters for the beam used in the clamped-sliding experiment are listed in Table 3.3. The beam was clamped to a large *Contraves* air bearing table using steel angle brackets as shown in Fig. 4.1. The air bearing table was not floating during the experiment and it was clamped so that it could not rotate. This was important because if the clamped end of the beam not held rigidly, the clamped-free model would have been invalidated. The beam was horizontal so that there were no non-linear stiffening effects due to gravity.

Motion of the tip of the beam was measured through the use of a linear accelerometer and an angular accelerometer. The angular accelerometer (Endevco model 7302-B) was rigidly attached to the tip of the beam via an aluminum bracket which was bolted to the beam. The linear accelerometer (Entran model EGA-125-5D) was mounted to the same bracket as the angular accelerometer by bonding it with bee's wax. Both accelerometers were piezoresistive and were

balanced using a Vishay strain gauge conditioner. The Vishay had a base gain of 100 with an additional adjustable gain. The gain for the angular acceleration signal was set to 20 for a total gain of 2000 in the Vishay, and the angular acceleration signal had a gain of 10 for a total gain of 1000. The angular accelerometer had a sensitivity of $3.5\frac{\mu V}{\text{rad/sec}^2}$ and the linear accelerometer had a sensitivity of $11.95\frac{mV}{\text{in/sec}^2}$.

The acceleration signals from the Vishay strain gauge conditioner were integrated using analog circuit integrators which included a high pass filter to ac-couple the signals. This eliminated any dc component due to drift of the Vishay. The controller was also built with analog components. The fractional operators were built using operational amplifier circuits as described in Appendix A, and they used ten-stage lattice networks in the feedback path. The valid frequency range for the $\sqrt{s}$ operator was 18 hz which is high enough to include the first two modes of the beam. The operator for $\sqrt{1/s}$ was implemented with smaller values for the resistors and capacitors in order to boost the gain for this operator. This also increased the bandwidth of the fractional integrator to several thousand hertz. The reason for such a large improvement in performance is not understood. The same values of resistors and capacitors were not used in the fractional differentiator because high frequency noise would have been amplified. The products of all the system gains were calculated and lumped into the four controller gains. These gains are given in Table 4.1. These gains include the gain of the Kepco amplifiers (Model BOP 1000M) which was 100. The gains also include the gains for the film actuators. The calculation of the actuator gains is described in Appendix C. The moment actuator had a gain of 9.937×10^{-5} in lbf/V. The force actuator had a gain of 9.0×10^{-7} lbf/V. Notice that the controller gains needed to match the characteristic impedance at the end of the beam are $G_{\dot{y}} = G_{\dot{\theta}} = K_{\dot{y}} = K_{\dot{\theta}} = 1$. The gains used in the controller were limited in magnitude because of the small gain of the film actuators. Voltages applied to the piezoelectric film were limited to ± 400 volts by using zener diodes in the controller circuitry. This was done because too high a voltage would destroy the piezoelectric film.

All measurements were taken with a Nicolet Dual Channel FFT Analyzer (model 660B) which was connected to a Tektronics digital plotter (model 4462).

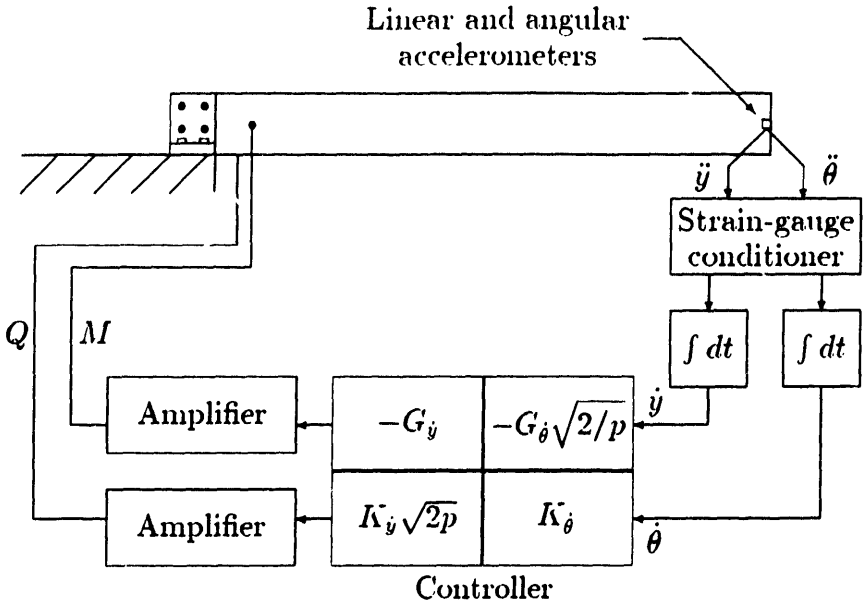

Figure 4.1: Side view of clamped-free beam setup

$G_{\dot{y}}$=0.01282
$G_{\dot{\theta}}$=166.2 $\times$ 10^{-6}
$K_{\dot{y}}$=0.0071
$K_{\dot{\theta}}$=287.35 $\times$ 10^{-6}

Table 4.1: Controller gains for clamped-free beam

4.1.2 Procedure and Results

All the data collected from experimentation with the clamped-free beam was restricted to the time domain. The calculation of frequency domain transfer functions was attempted via impact testing. However, the sharp pulse produced by a hammer impact caused current surges that were harmful to the piezoelectric film. For this reason, impact testing was abandoned, and tests were restricted to initial displacement decays except for several time domain decay excited by a light impact.

For the initial displacement tests, the tip of the beam was displaced one inch and released. This type of input mainly excited the first mode of the beam. Fig. 4.2 shows the linear tip acceleration signal produced for a free decay with the controller unattached. The end point impedance controller was then attached so that both a control force and a control moment would be applied to the end of the beam. Fig. 4.3 shows the linear tip acceleration with the controller attached. In order to study the seperate effects of the control moment and the control force, first the control force was disconnected so that only a control moment was applied (G-control); then the control moment was disconnected leaving only the control force (K-control). Fig. 4.4 shows the response of the linear tip acceleration to an initial displacement with the control moment applied, and Fig. 4.5 shows the response of the linear tip acceleration to an initial displacement with the control force applied.

In order to demonstrate the active control of more that one mode simultaneously, an impact test was done using a very light hit so that the film would not be damaged. The result of the impact was to excite multiple modes at once. A typical force pulse is shown in Fig. 4.6 with a magnified time scale so that the pulse shape details are visible. The typical force pulse had a duration of 0.005 seconds and a peak magnitude of 0.8 pounds. Fig. 4.7 shows the response of the linear tip acceleration to an impact with the controller unattached. Fig. 4.10 show the response of the linear tip velocity of the clamped-free beam to an impact.

The end point impedance controller was then attached and the tip of the beam was again impacted. Fig. 4.8 shows the controlled response of the linear tip acceleration to an impact. Fig. 4.9 shows a simulation of the response of the

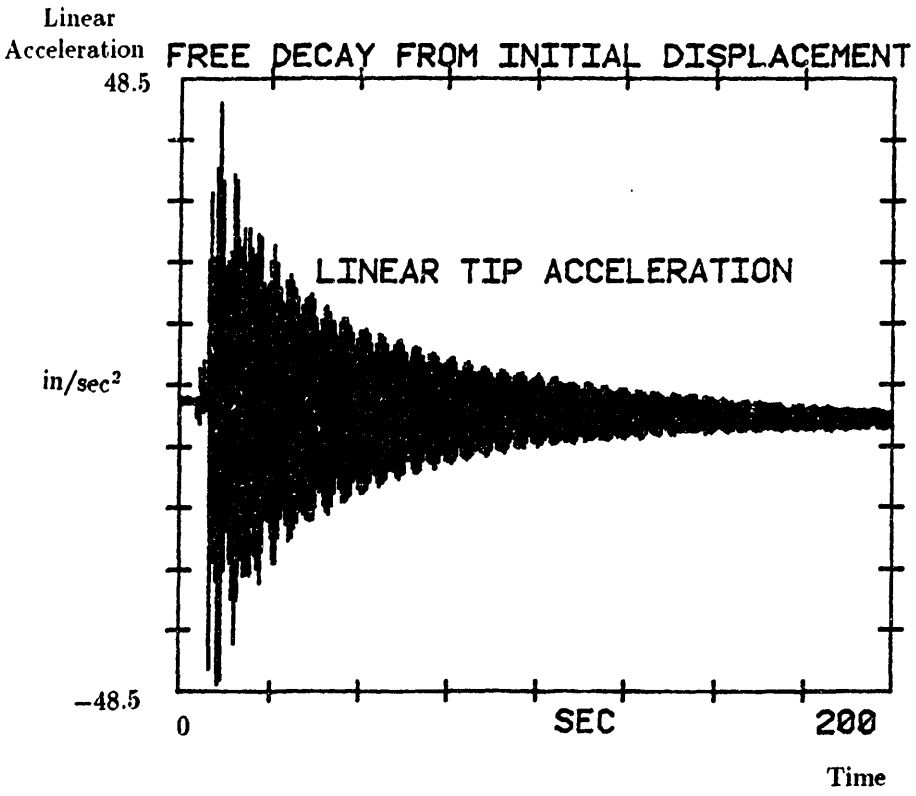

Figure 4.2: Free decay from initial displacement for clamped-free beam

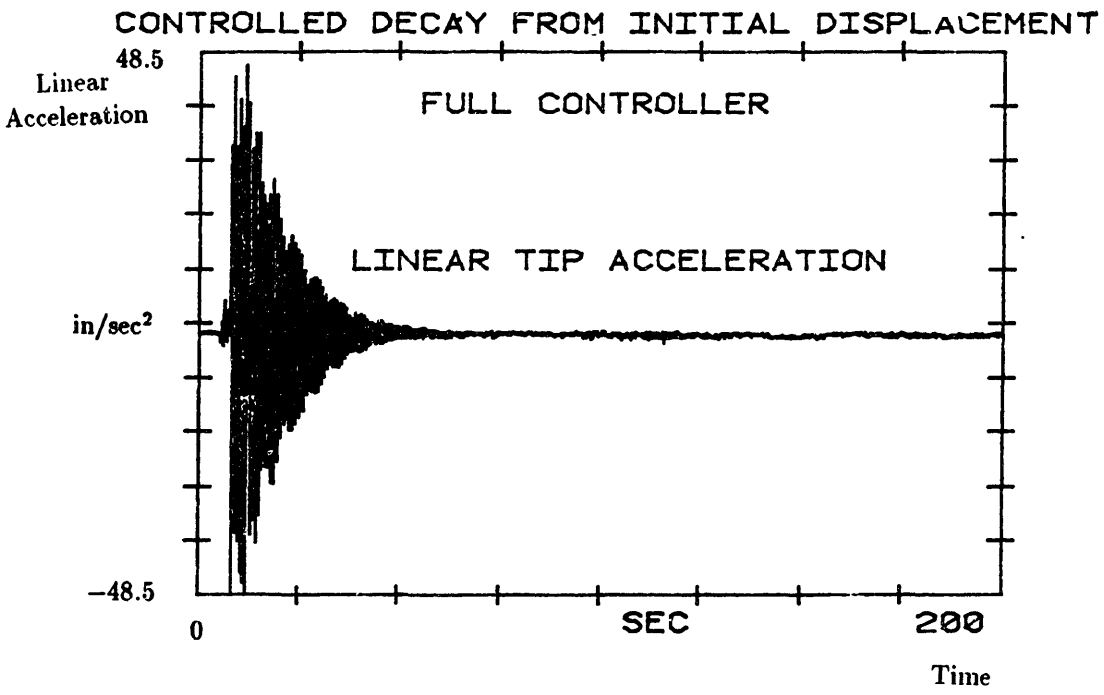

Figure 4.3: Controlled decay from initial displacement for clamped-free beam

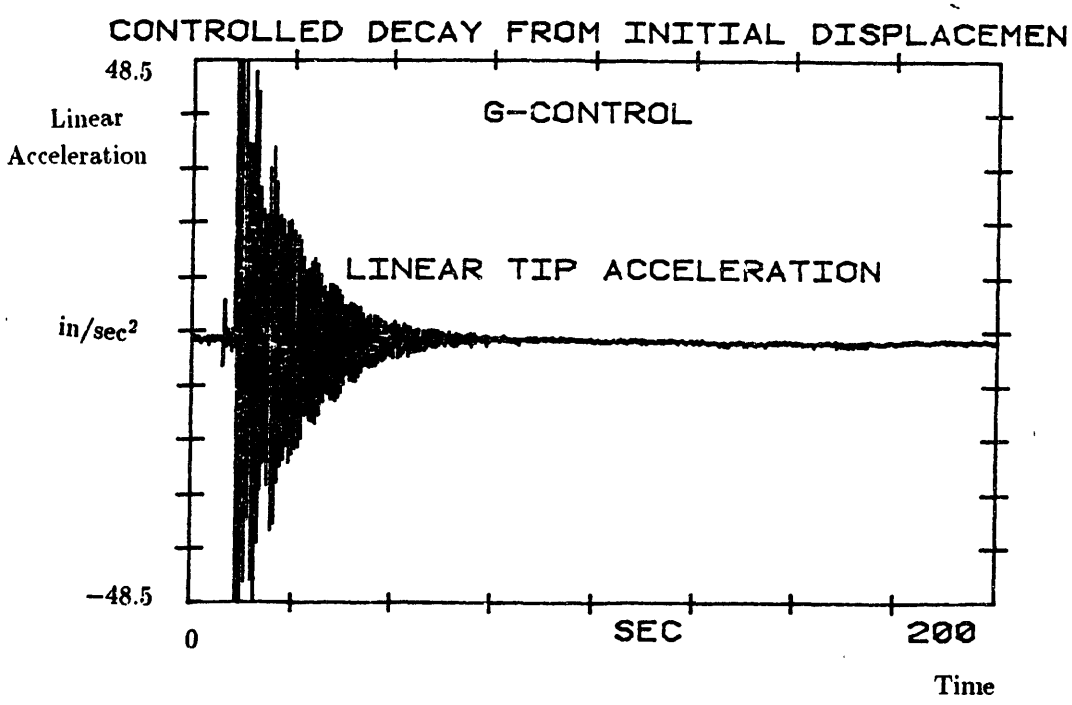

Figure 4.4: G-control of clamped-free beam

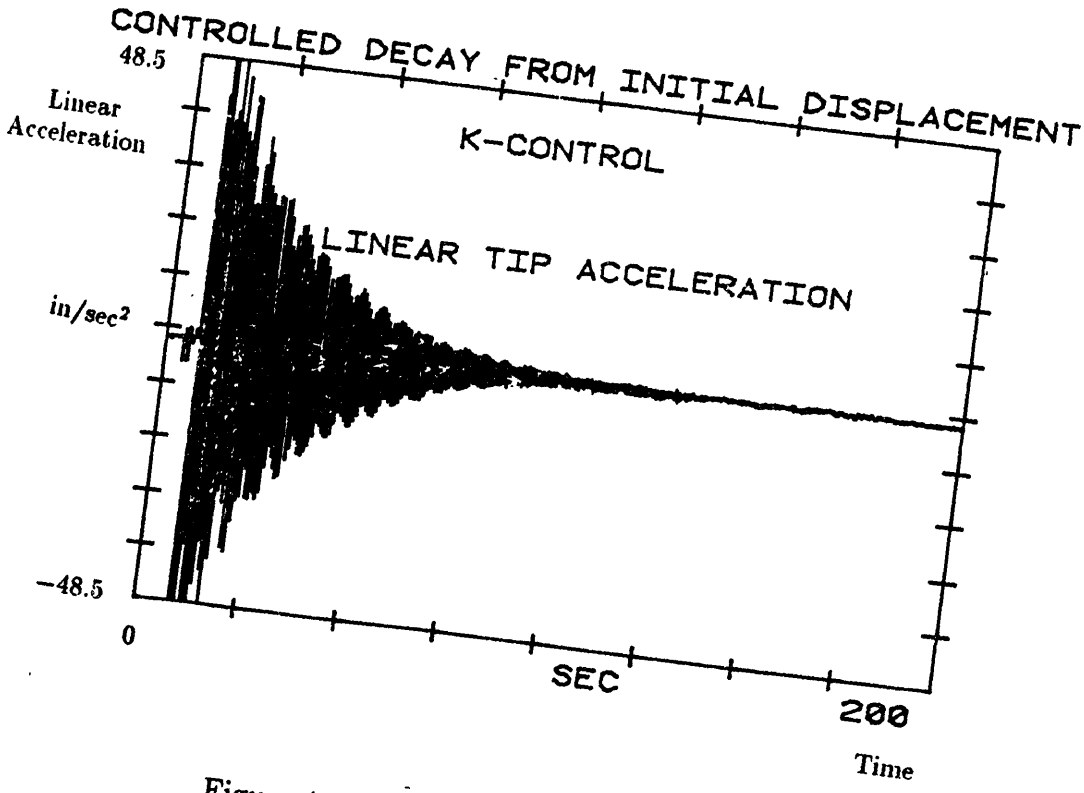

Figure 4.5: K-control of clamped-free beam

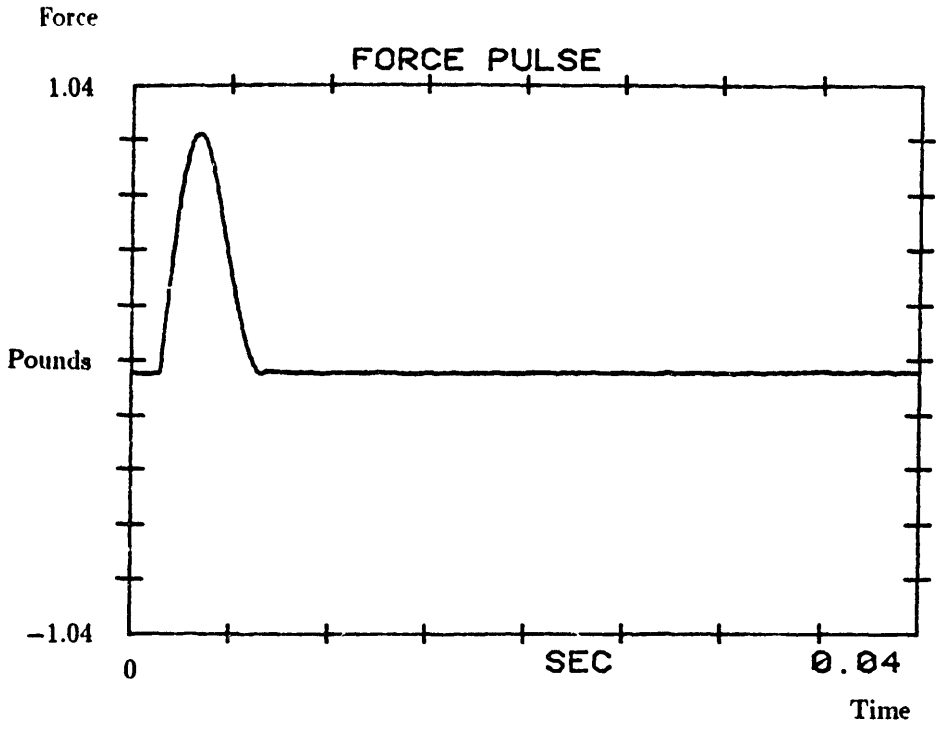

Figure 4.6: Typical impact pulse applied to clamped-free beam

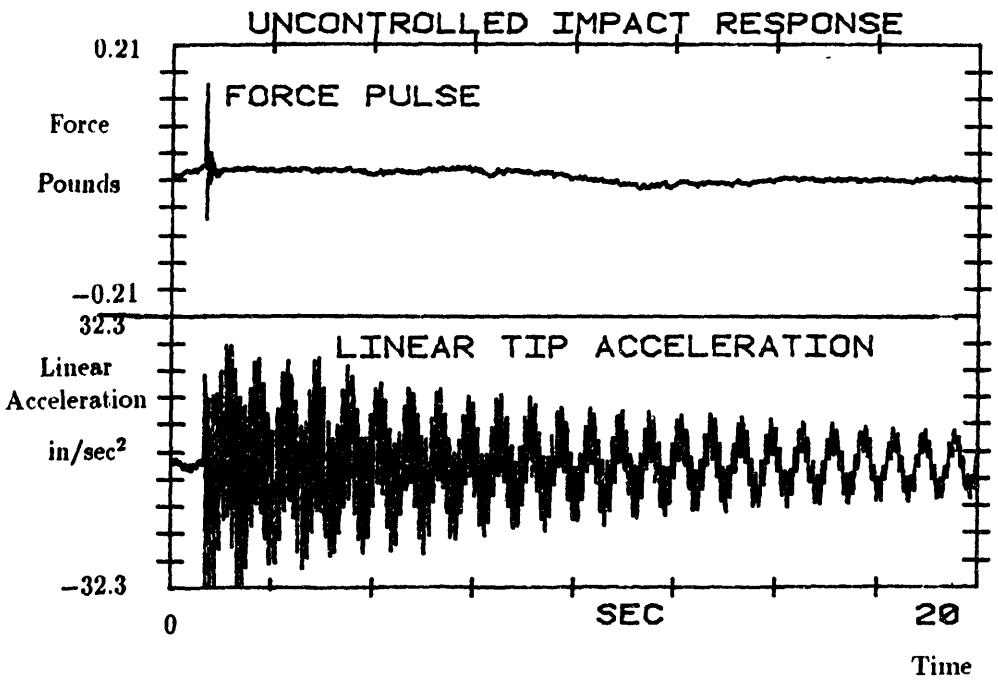

Figure 4.7: Uncontrolled impact response of clamped-free beam

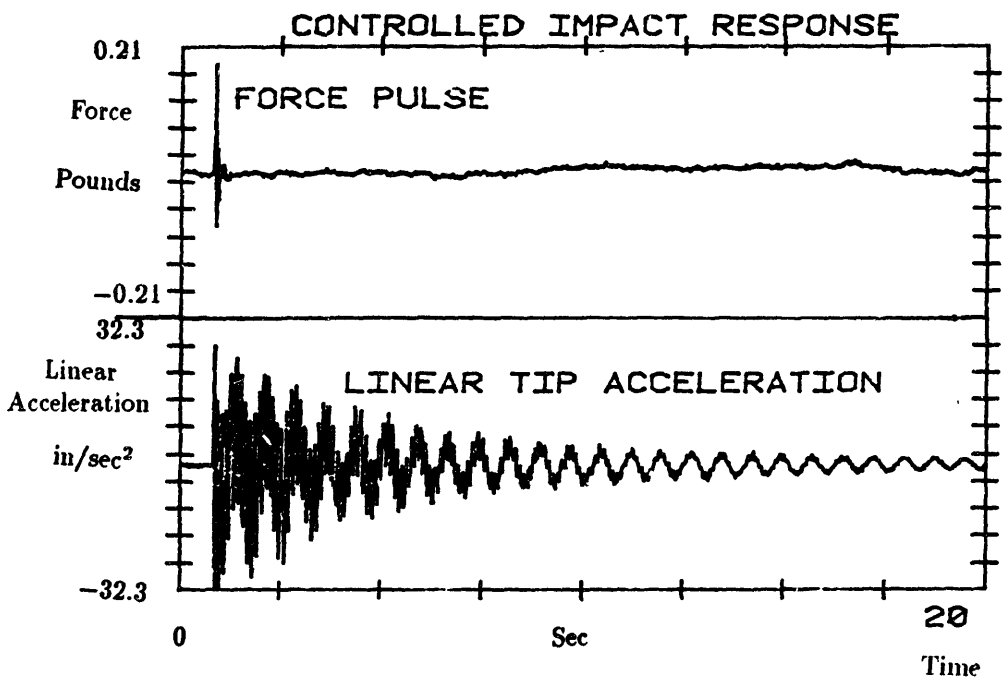

Figure 4.8: Controlled impact response of clamped-free beam

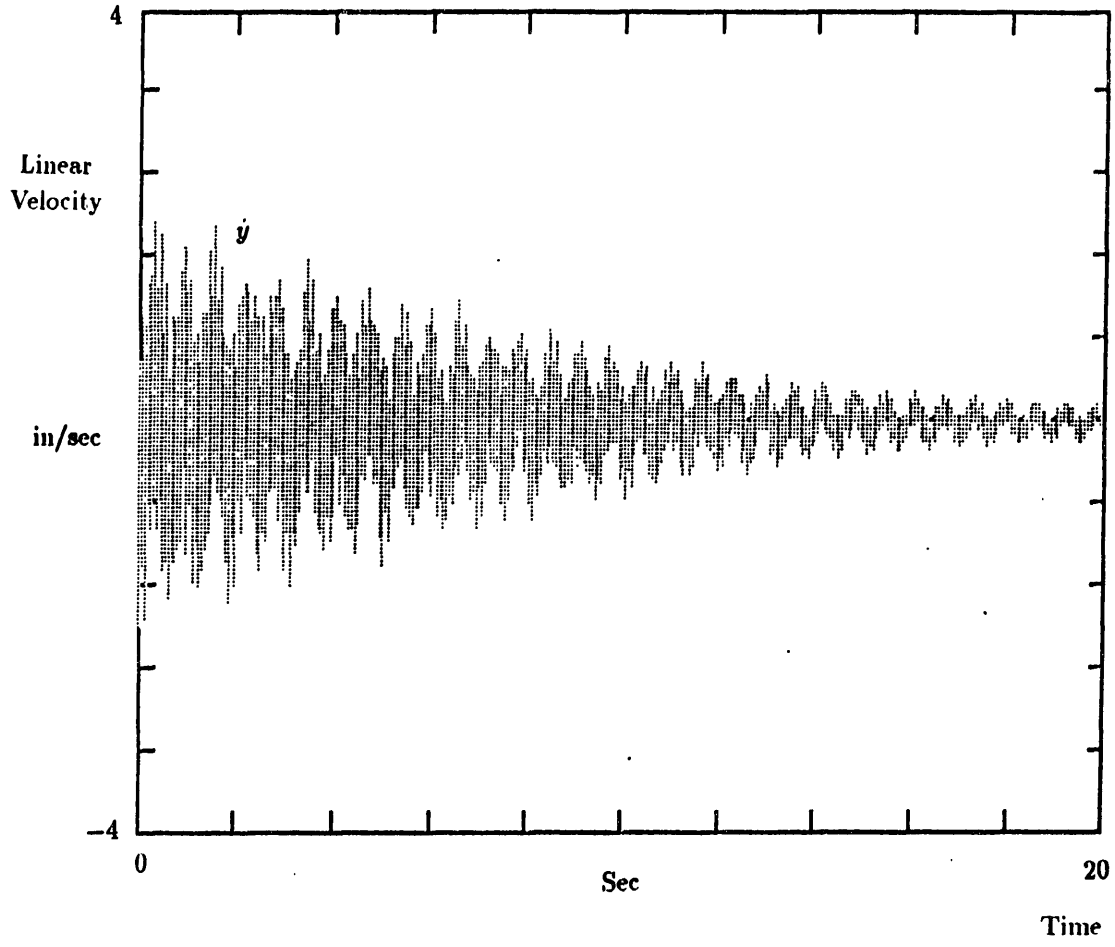

Figure 4.9: Simulation of impact response

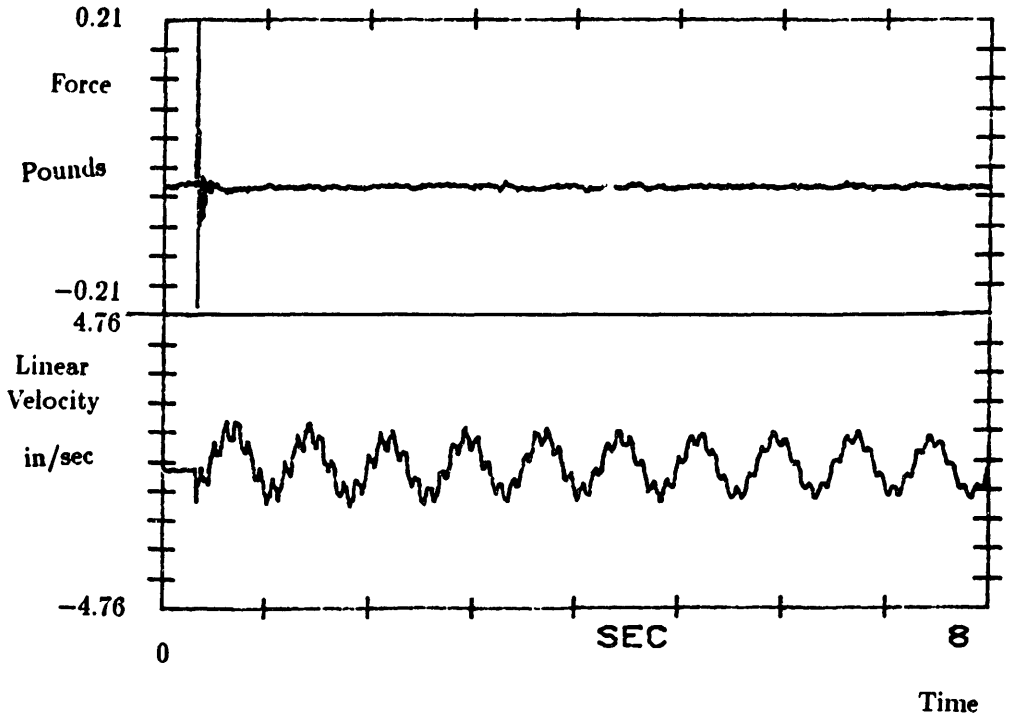

Figure 4.10: Uncontrolled impact response of $\dot{y}$ of clamped-free beam

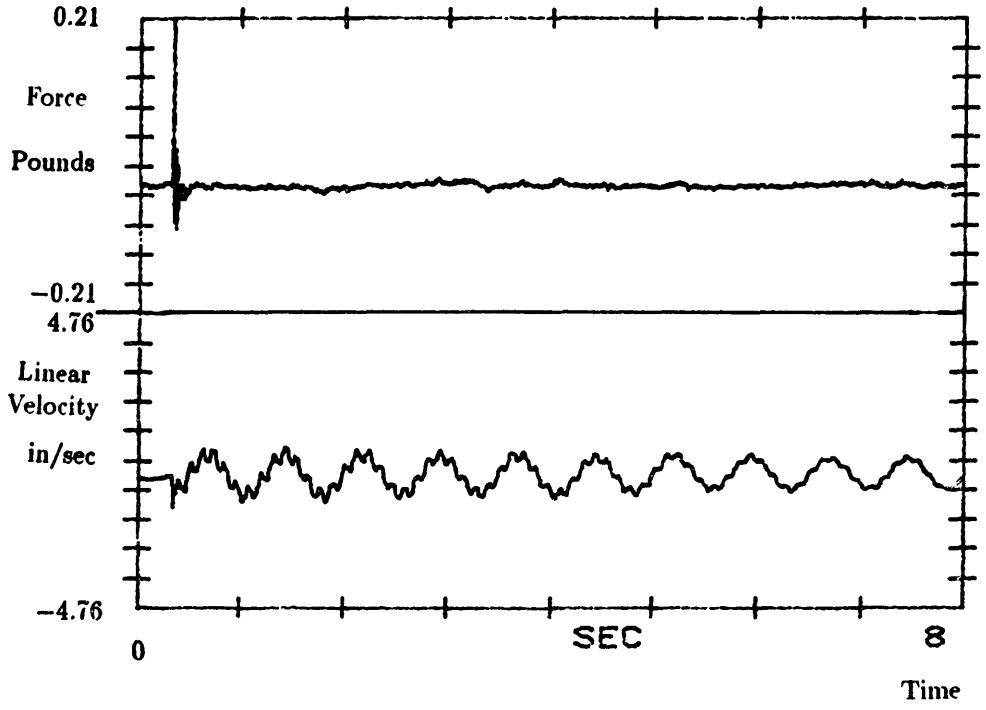

Figure 4.11: Controlled impact response of $\dot{y}$ of clamped-free beam

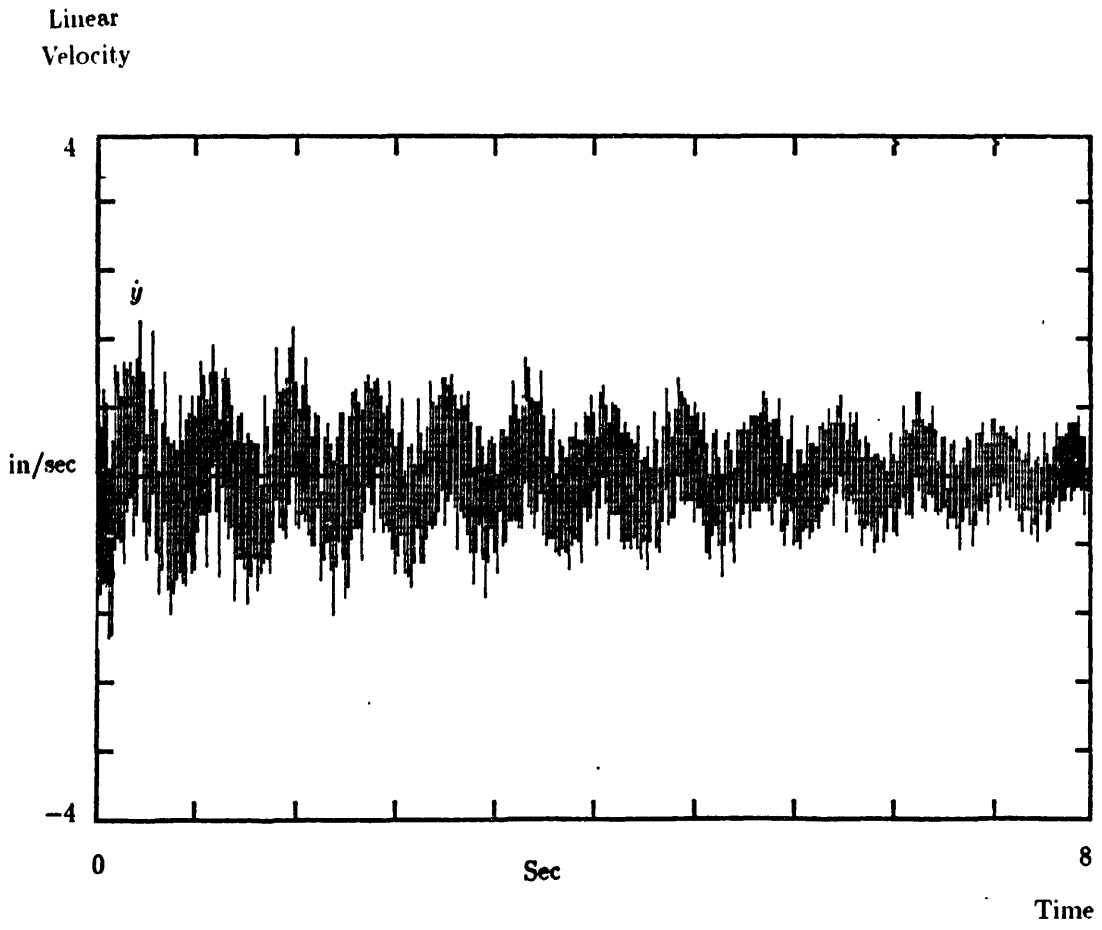

Figure 4.12: Simulation of impact response of $\dot{y}$ of clamped-free beam

linear tip velocity to the same pulse. Fig. 4.11 shows the controlled response of the linear tip velocity, and Fig. 4.12 shows a simulation of the controlled response of the linear tip velocity.

4.1.3 Results and Discussion

By comparing Fig. 4.2 and Fig. 4.3, it is evident that the end point impedance controller damps the first mode vibrations of the clamped-free beam. The settling time is reduced from over 200 seconds to 50 seconds. In order to see the damping of the second mode, a smaller time window was used. Examination of Figs. 4.7 and 4.8 shows that both first and second mode vibrations are controlled. This is as expected since the controller is designed to absorb travelling waves and not simply control individual modes of the beam. The first two modes of the clamped-free beam had frequencies of 1.35 hz and 8.65 hz. Since the valid frequency range for the $\sqrt{s}$ operator is limited to 18 hz, these are the only two modes which were examined. Even though the $\sqrt{s}$ operator had the incorrect phase above 18 hz, there was still no problem with instability of the higher frequency modes, as might be expected. This is because the $\sqrt{1/s}$ operator had a frequency range of several thousand hertz. Comparing Figs. 4.4 and 4.5, it is seen that the moment part of the control is more effective than the force part. Since the $\sqrt{s}$ operator contributes to the force part of the control, the force signal is valid only up to 18 hz. However, since the $\sqrt{1/s}$ operator contributes to the moment part of the control, the moment signal is valid up through the higher frequency modes. And since the moment part of the controller is more effective, it acts to diminish the effects of any instability of the higher frequency modes due to the $\sqrt{s}$ operator.

In order to show that the mathematical model of the beam and the controller was correct, simulations were run using the actual gains measured for the controller, and the same pulse input as is shown in Fig. 4.6 (compare Fig. 3.8 for pulse shape). Fig 4.9 shows the controlled linear tip velocity response to the same conditions as the response shown in Fig. 4.8. It must be realized that the simulation displays velocity while the real data shows acceleration, but the comparison is for the amount of decay over a similar time period. Notice that the simulation has the about the same amount of decay over the 20 second period as the real data. A more meaningful comparison can be made between Figs. 4.11

and 4.12. The simulation is given the same input as was used in the experiment, and it is seen that the two traces are very similar. The major difference between these two plots is the high frequency content in the simulation signal. This is because the theoretical model for the beam does not include any passive damping in the beam whereas the higher modes of the real beam damp out within several seconds. By adding a low-pass filter with a cutoff frequency of 20 hz to the output of the simulation, the first two modes can be seen more clearly. The results of adding the filter to the simulation can be seen in Fig. 4.13 where the top trace is the unfiltered velocity, and the bottom trace is the filtered velocity. The resulting response closely resembles Fig. 4.11 which gives credibility to the mathematical models for the beam and the controller.

4.2 Clamped-sliding beam

4.2.1 Experimental Setup

In order to enforce a sliding end condition, two identical beams were clamped to an aluminum block so that the two beams were parallel. The aluminum block was bolted to a massive table so that the clamped end of the beam was held rigidly. The sliding boundary condition was produced by connecting the two beams with a light aluminum tube as shown in Fig. 4.14. The connecting tube enforced a zero slope condition at the tip so that the beam assembly acted like a clamped-sliding beam. The parameters for the beam assembly are listed in Table 3.4. The mass of the connecting link was 0.05286 pounds so that the boundary condition was actually sliding with a tip mass. The beam assembly was clamped to the table so that the beam vibrated in the horizontal plane.

The motion at the tip was linear motion and was sensed with an Entran linear accelerometer. The Vishay strain gauge conditioner was set at the same gain (i.e., 2000) as with the clamped-free experiment. Only one element of the characteristic impedance controller was used. This was due to the absence of angular motion at the tip of the beam. Also, the only control effort that could do work was a force. A moment would not do any work because the tip could not rotate. The output of the controller was limited with zener diodes as with the clamped-free beam controller to protect the film. The signal was limited to ± 4 volts which was amplified by the Kepco which had a gain of 100. The force

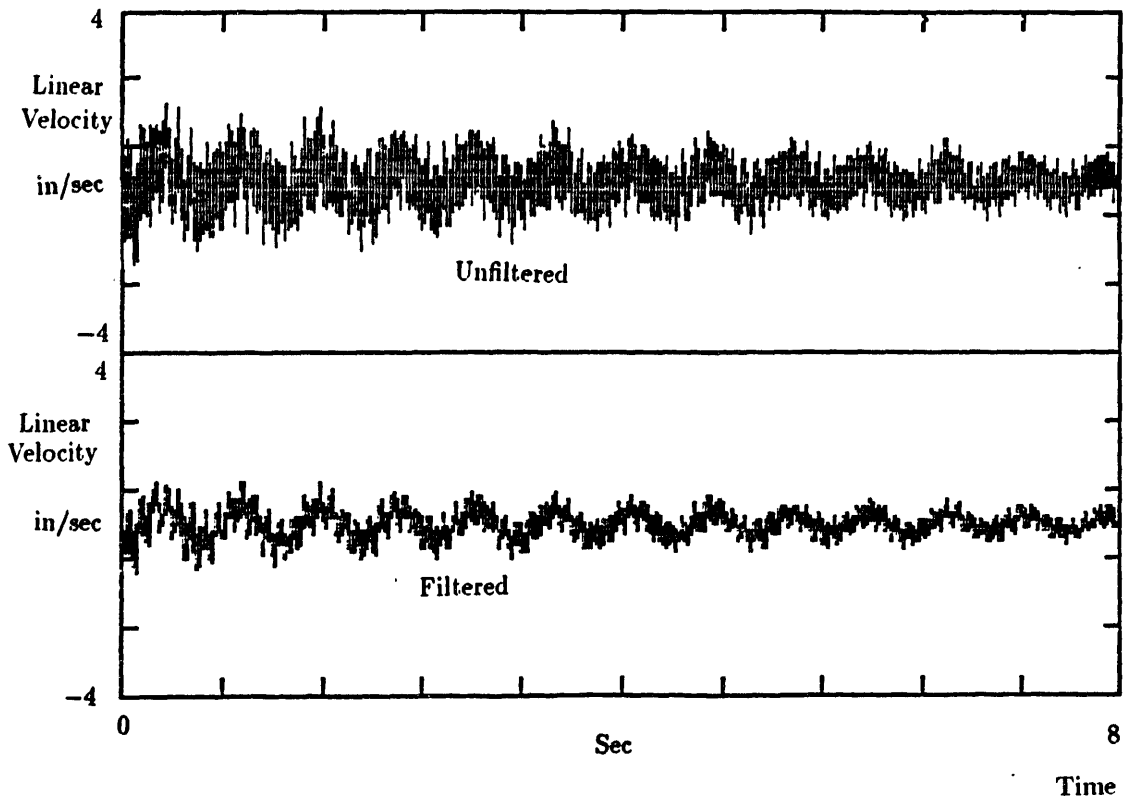

Figure 4.13: Low pass filter added to output of simulation

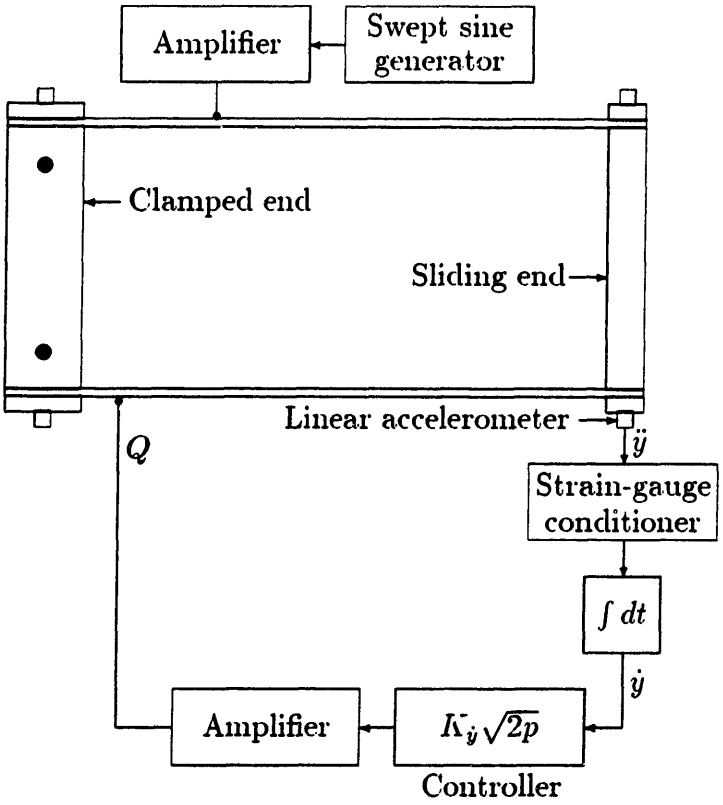

Figure 4.14: Top view of clamped-sliding beam setup

actuator used was piezoelectric film with a linear distribution as described in Appendix C. The gain for the film actuator was 1.7364×10^{-4} lbf/V created by using two pieces of film: one on each beam. The combination of all the gains in the system were lumped together so that $K_{\dot{y}} = 0.545$. There was a second set of film actuators bonded to the other side of each beam used to excite the beam assembly with a swept sine force so that frequency response data could be obtained. The swept sine signal was generated with a Zonic spectrum analyzer. The excitation signal was amplified with a Kepco amplifier so that the excitation signal applied to the film was ±450 volts.

4.2.2 Procedure and Results

For the clamped-free beam experiment, both sides of the beam were needed for piezoelectric film control actuators. In the case of the clamped-sliding beam, only one side of the beam was needed for control actuation. The other side was available to bond piezoelectric film for use as an excitation source. Therefore, it was possible to excite the beam with an sinusoidal force whose frequency continuously swept a range of values making it possible to calculate a transfer function. This will be discussed after a description of the initial displacement testing.

Decay from Initial Displacement

In order to study the effects of the fractional derivative controller on the damping of the clamped-sliding beam, the decay from an initial displacement was studied. The tip of the beam was displaced by three-sixteenths of an inch and released. Fig. 4.15 shows the free decay of the clamped-sliding beam. The figure also shows the control signal in the top portion of the plot, although the controller was not actually connected via a feedback signal to the beam. Fig. 4.16 shows the controlled response of the clamped-sliding beam with the force signal sent to the control actuator.

For the purposes of comparison, two different controllers were hooked up to the beam. The first was linear velocity feedback which is effectively a dashpot, and the second is a bang-bang type controller which was implemented by feeding the linear velocity feedback through an analog comparator. The responses for

these two controllers are shown in Figs. 4.17 and 4.18.

Swept Sine Excitation

The first attempts at frequency domain analysis of the clamped-sliding beam were done using an impact hammer. The resulted in the total destruction of metalized coating of the piezoelectric film. As an alternative, a second set of film actuators were used to excite the film with a swept sine force input. The excitation voltage of ±450 volts produced a tip motion of approximately ±1/4 inches.

The swept sine was a continuous sweep from three hertz to seven hertz at a rate of 0.02 hz/sec. Figs. 4.19 and 4.20 show the uncontrolled and the controlled transfer functions respectively up to 5 hz which includes the first mode. The frequency scales are linear and the magnitude scales are logarithmic. The same plots are shown with linear-linear scales in Figs. 4.21 and 4.22 so that the difference in peaks is emphasized. On all plots, the transfer function below three hertz is meaningless since the input excitation was band-limited between three and seven hertz.

The sine sweep was reset to try to capture the modal frequency of 4.9125 hz so that better data could be obtained. The frequency sweep was set from four to six hertz. A plot showing an overlay of the uncontrolled transfer function and the controlled transfer function is shown in Fig. 4.23. Again, the plot is meaningless for frequencies below four hertz and above six hertz.

The Nicolet spectrum analyzer was able to calculate damping factors from the transfer function. The damping factor for the uncontrolled beam was $\zeta = 0.00507$ and the damping factor for the controlled beam was $\zeta = 0.0128$. Also, the uncontrolled modal frequency of 4.9125 hz was changed to 4.875 hz with control.

4.2.3 Discussion

In Figs. 4.15–4.18 it is easier to see when the motion has stopped by examining the control signal rather than the acceleration signal. It is clearly seen that the fractional derivative controller is controlling vibrations at the tip of the beam. The control signal if Fig. 4.15 is still quite large at 40 seconds whereas when the

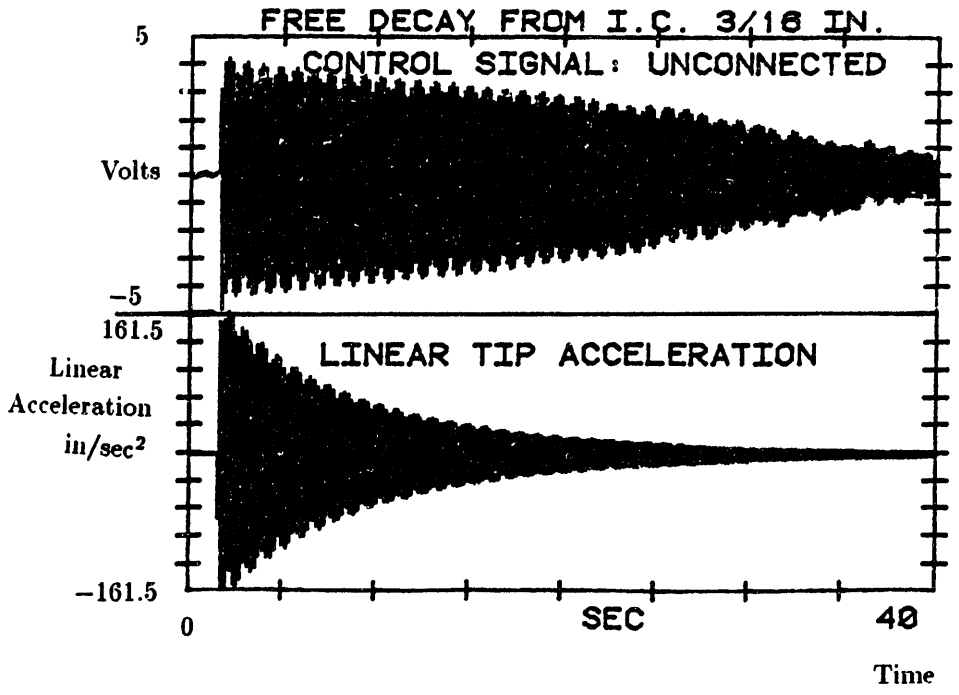

Figure 4.15: Free decay of clamped-sliding beam from initial displacement

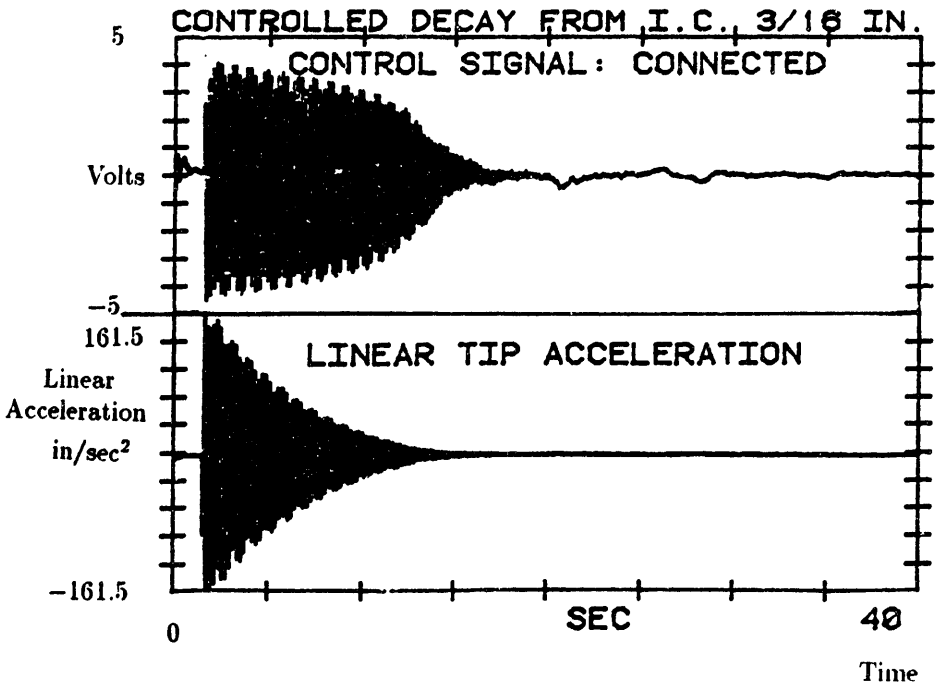

Figure 4.16: Controlled decay of clamped-sliding beam from initial displacement

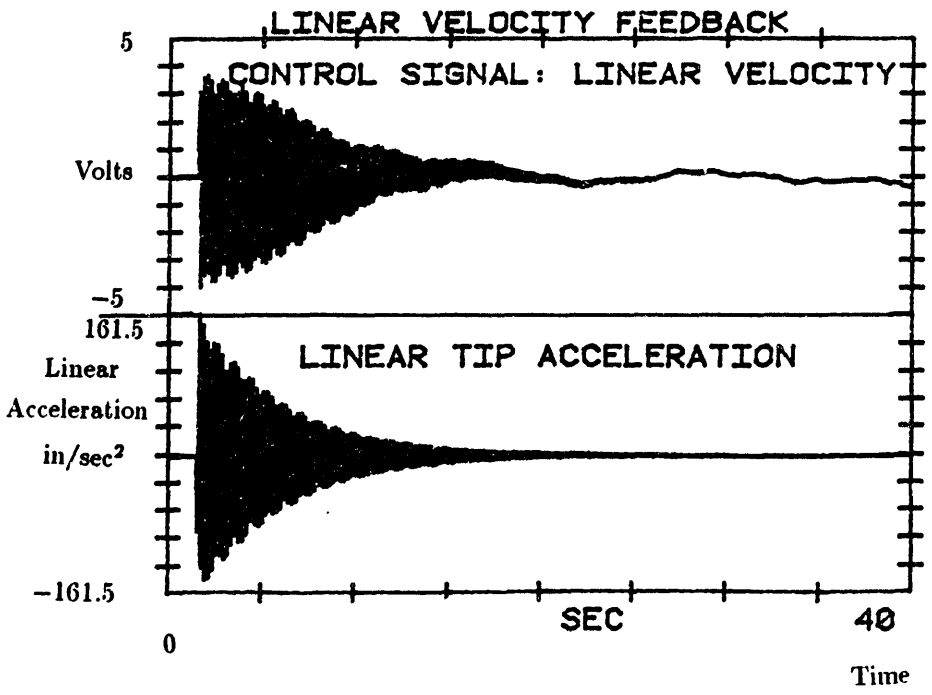

Figure 4.17: Linear velocity feedback control

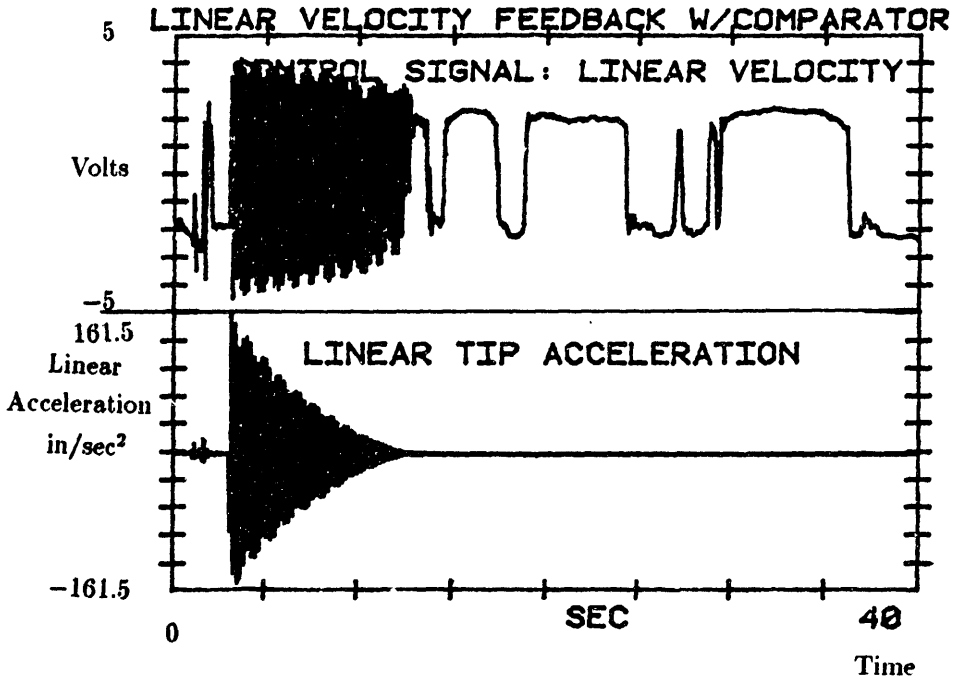

Figure 4.18: Bang-bang control

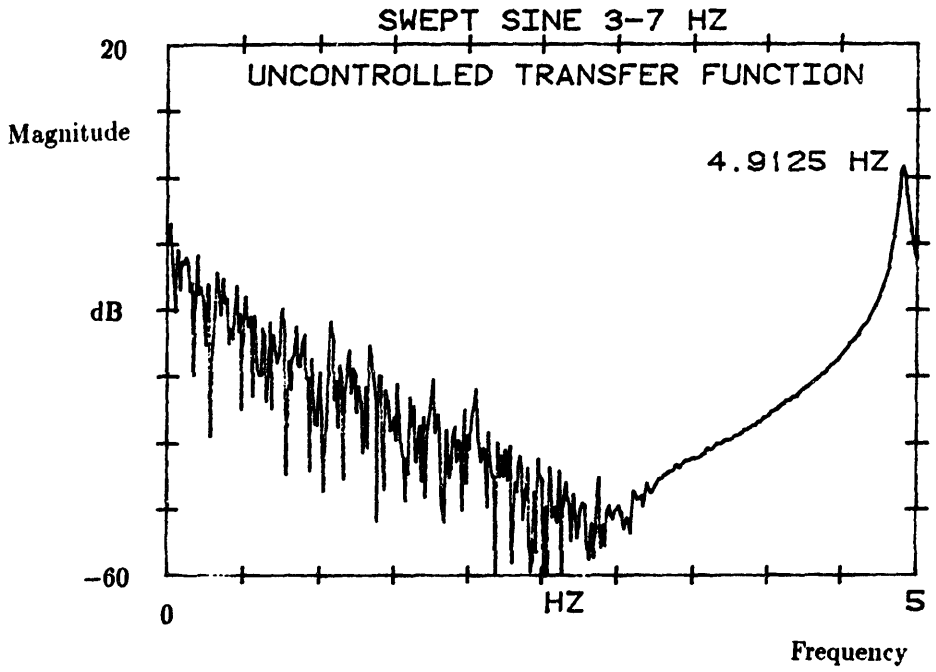

Figure 4.19: Transfer function of uncontrolled beam

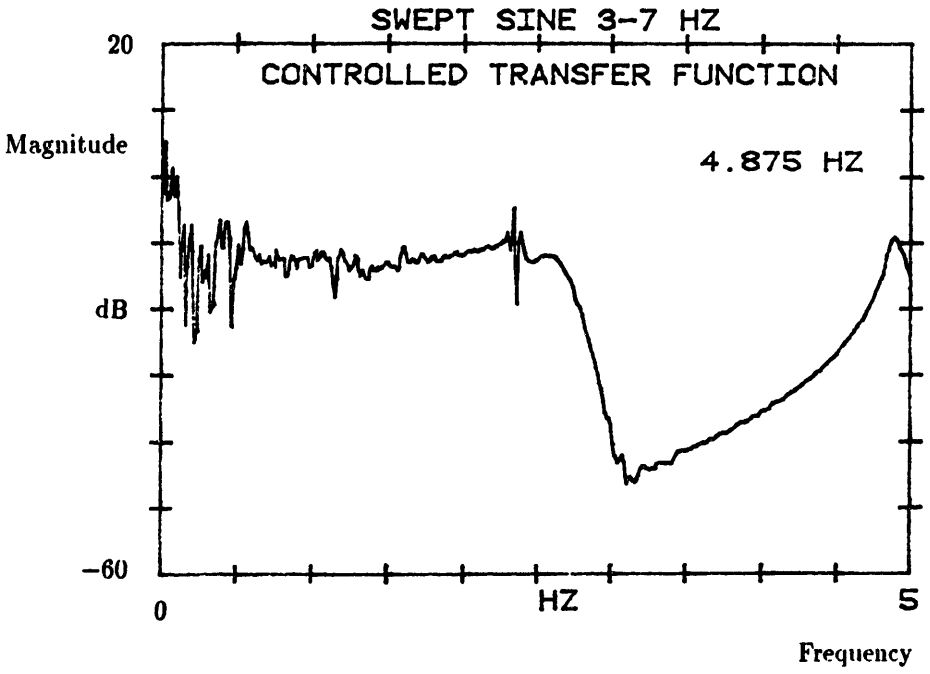

Figure 4.20: Transfer function of controlled beam

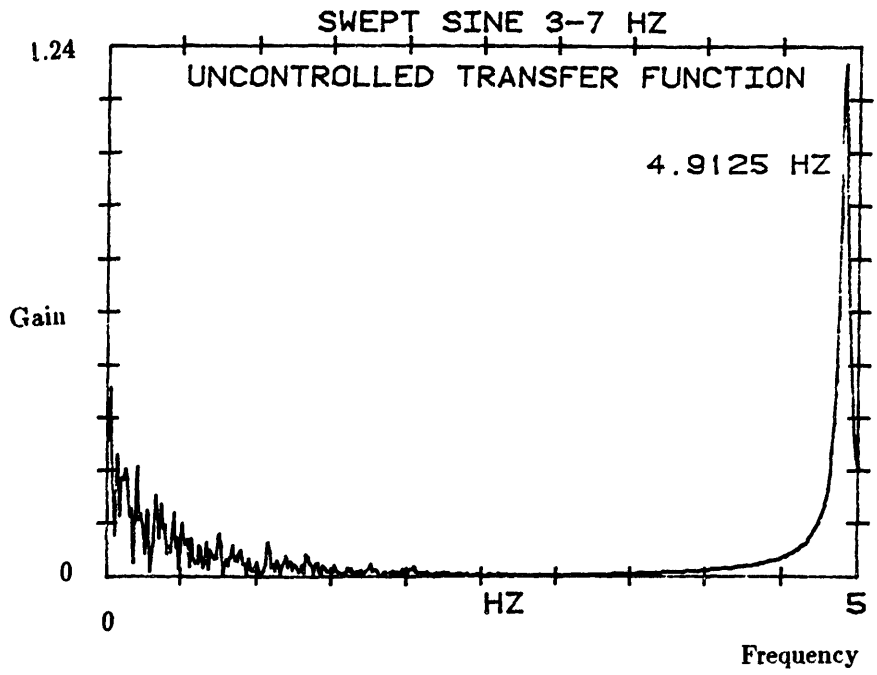

Figure 4.21: Transfer function of uncontrolled beam: linear-linear scales

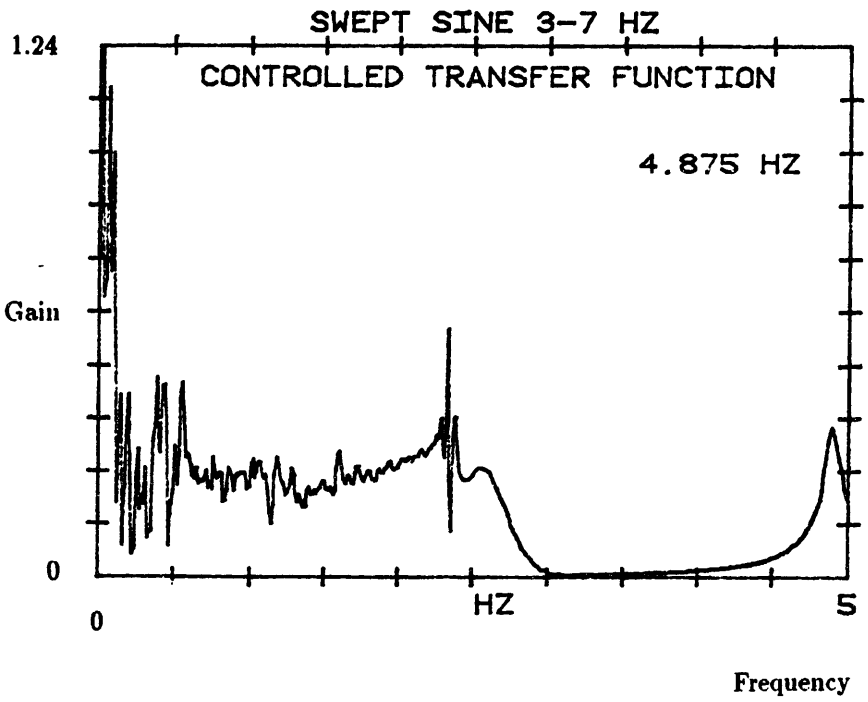

Figure 4.22: Tranfer function of controlled beam: linear-linear scales

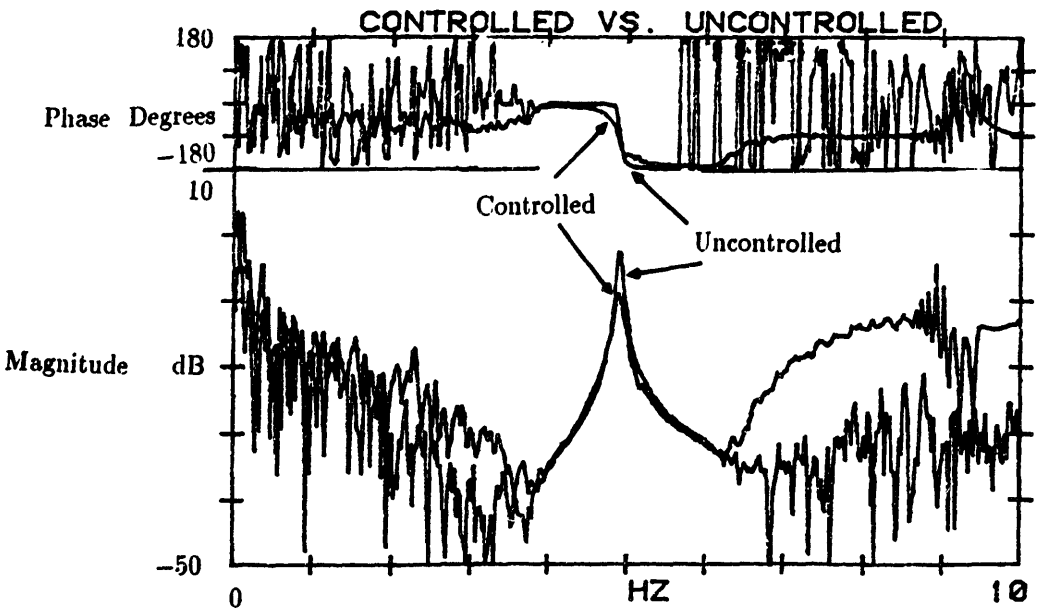

Figure 4.23: Controlled vs. uncontrolled transfer function

control signal is fed back to the beam as is done in Fig. 4.16, the control signal is zero after 15 seconds.

Of the two alternate controllers that were tried for a comparison, the linear velocity feedback controller does not do as good a job as the fractional derivative controller. The bang-bang controller does do a better job but only slightly so. This is because the bang-bang controller uses larger control forces than the fractional derivative controller for small signals. The advantage of the fractional derivative controller is that it is a proportional type controller so that it is less likely to excite vibration in other parts of a complex structure to which the controlled beam is may be attached.

Figs. 4.19 and 4.20 show that the resonant peak varies from 12 dB to -9 dB, and that the frequency changes from 4.9125 hz to 4.875 hz. The drop in the resonant peak is even more dramatic when plotted with linear scales as in Figs. 4.21 and 4.22. The change in damping factor from $\zeta = 0.00507$ to $\zeta = 0.0128$ represents a 152% increase in damping. The change in resonant frequency from 4.9125 to 4.875 represents a 0.76% decrease in the resonant frequency. This means that the system poles have been moved by the addition of the controller. A more complete parameter study would involve varying the gain so that a root-locus could be calculated. This was not done because a smaller gain would not have given much damping above the base passive damping of the beam, and an increase in gain was limited by the voltage that could safely be applied to the film.

One problem that arose during the control of the clamped-sliding beam was observation spillover. When the fractional derivative controller was attached, a mode at 102 hz became unstable. As was mentioned before, the implementation of the fractional derivative used was limited to 18 hz, after which the phase rolls off to zero. Unlike with the clamp-free beam, the clamped-sliding beam controller does not have the benefit of a control moment which has the correct phase at the higher frequencies to diminish the effects of observation spillover. However, the addition of a low-pass filter for the acceleration measurement with a 40dB/decade cutoff at 50 hz completely eliminated the spillover problem.

Chapter 5

Conclusions and Recommendation

5.1 Conclusions

The active control of vibrations in flexible structures such as long, cantilevered members on space structures, or smaller, high precision devices such as the Remote Center Compliance (a device used as part of the end effector of a robot for close tolerance assembly), may be done based on a distributed parameter model of the flexible structures. A Bernoulli-Euler beam model may be used to model the flexible structures by using the appropriate boundary conditions. Instead of using a lumped parameter model to design a controller for such systems, it is possible to design a controller based on the distributed parameter nature of the structure. Two types of structures were studied: a clamped-free beam which may be applied to the most general flexible structure problem; and a clamped-sliding beam which is used to model a Remote Center Compliance.

It is shown in Chapter 2 how an end point impedance controller with the same form as the characteristic impedance of the beam can null waves travelling along the beam so that no waves are reflected which prevents standing waves from forming on the beam. This situation is analogous to the characteristic termination of an electrical transmission line. This controller is designed to absorb any waves so that there is no consideration toward the damping of a particular mode. This also means that all modes are controlled by an end point characteristic impedance controller.

The characteristic impedance of a Bernoulli-Euler beam involves fractional

operators with laplace transforms of $\sqrt{s}$ and $\sqrt{1/s}$. These operators may be implemented with analog circuits which involve an RC lattice which can be made arbitrarily large to approximate the fractional operators up to higher frequencies.

In order to match the characteristic impedance of a beam, it is necesarry to measure both angular velocity and linear velocity at the tip of the beam. This is possible in a free-free or clamped-free beam configuration. For a clamped-sliding beam configuration, there is no angular velocity produced at the end of the beam so that the characteristic impedance cannot be matched. However, a subset of the characteristic impedance controller—the fractional derivative—may be used to control vibrations at the tip of the beam.

The controller can be designed and implemented with very little truncation of the model. The only approximation enters into controller through the implementation of the fractional operators which can only be approximated. Even so, it is shown that the implementation of the fractional integrator can be made to behave like a true fractional integrator for a very large bandwidth.

The continuous model does need to be truncated in order to do digital simulations of the beam and controller. The model for the beam was approximated by matching the systems bode plots for an arbitrary number of modes. The number of modes modelled for digital simulation for the clamped-free beam was five. The approximation of the fractional operators was done using a Regular Newton process which is an iterative approximation process.

Dynamic simulations show that the characteristic impedance controller effectively controls motion at the end of a free-free beam and a clamped-free beam; and that the fractional derivative controller controls the vibration of the tip of a clamped-sliding beam. However, these simulations assume that the actuation efforts are not limited in magnitude. The actuators used on two experimental beams—a clamped-free beam and a clamped-sliding beam—were made with piezoelectric polymer film which could create finite control efforts which were limited by the amount of voltage that could safely be applied.

Even with the small control efforts, the controller was able to increase the damping of both the clamped-free beam, and the clamped-sliding beam. A dynamic simulation of the clamped-free beam with experimental parameters and gains put into the model closely simulates the behavior of the actual experiment. This gives confidence that the mathematical models for both the beam and the

controller are valid.

The settling time for the clamped-free beam decreased by more that a factor of four for the first mode. Also, it was shown that the characteristic impedance controller was able to control the first and second modes simultaneously.

The fractional derivative controller used on the clamped-sliding beam was able to increase the damping factor ζ by 152%. The settling time for the fracional derivative controller is 24% shorter than for the linear velocity feedback controller using comparable gains. The settling time for the bang-bang controller is 53% shorter than for the fractional derivative controller. However, the fractional derivative controller produces a proportional type control which is sinusoidal whereas a bang-bang controller produces a square wave.

5.2 Recommendations

One of the most lamentable aspects of the experimental part of this thesis is that the actuators were so weak. If the characteristic impedance control law could be tested with the use of a reaction wheel to produce a moment, and a proof mass actuator to produce a force, the theory would be incontravertably substantiated.

The use of stronger actuators would allow a wider range of gains to be used. It would then be possible to calculate root-locus plots in which case performance could be specified and the appropriate gains applied.

One of the flaws with the dynamic simulations of the beam/controller systems is that the passive damping of the beam is not included. In order to get truly accurate simulations, the passive damping should be included.

It would also be good to have a fractional derivative operator implementation with a higher bandwidth. This would eliminate the problem of observation spillover.

A more detailed modeling of the boundary conditions should include tip masses and inertias. The reflections matrices L_{22} and R_{22} should be expanded to include the effects of inertial elements.

Bibliography

[1] Acton, F. S., *Numerical Methods That Work*, Harper & Row, Publishers, New York.

[2] Bailey, T. L., "Distributed-Parameter Vibration Control of a Cantilever Beam Using a Distributed-Parameter Actuator", Combined Bachelor's and Master's thesis, Massachusetts Institute of Technology, September, 1984 Also Draper Laboratory report CSDL-T-863.

[3] Bailey, T. L., and J. E. Hubbard, Jr., "Distributed Piezoelectric-Polymer Active Vibration Control of a Cantilever Beam", *Journal of Guidance* **8**(5), September-October 1985, pp. 605–611.

[4] Balas, M., "Feedback Control of Flexible Systems", *IEEE Transactions Automatic Control*, Vol. AC–23, August 1978, pp. 673–679.

[5] Berkman, F., and D. Karnopp, "Complete Response of Distributed Systems Controlled by a Finite Number of Linear Feedback Loops", *Transactions of the ASME, Journal of Engineering for Industry*, November 1969, pp. 1063–1068.

[6] Book, W. J., and M. Majett, "Controller Design for Flexible, Distributed Parameter Mechanical Arms via Combined State Space and Frequency Domain Techniques",

[7] Brown F. T., "A Unified Approach to the Analysis of Uniform One-Dimen/-sional Distributed Systems", *Transactions of the ASME, Journal of Basic Engineering*, June 1967, pp. 423–432.

[8] Brown F. T , "On the Dynamics of Distributed Systems", *Applied Mechanics Reviews*, Vol. 17, No. 5, May 1964.

[9] Burke, S. E., and J. E. Hubbard, Jr., "Distributed Parameter Control Design for Vibrating Beams Using Generalized Functions", presented at Forth IFAC Symposium on Control of Distributed Parameter Systems, 29 June-3 July, 1986, Los Angeles, California.

[10] Carlson, G. E., and C. A. Halijak, "Approximation of Fractional Capacitors $(1/s)^{1/n}$ by a Regular Newton Process", *IEEE Transactions of Circuit Theory*, June 1964, pp. 210–213.

[11] Carlson, G. E., and C. A. Halijak, "Simulation of the Fractional Derivative Operator $\sqrt{s}$ and the Fractional Integral Operator $\sqrt{1/s}$", *Kansas State University Bulletin*, Vol. 45, pp.1-22, July 1961.

[12] Crandall, S., D. Karnopp, E. Kurtz, and D. Pridmore-Brown, *Dynamics of Mechanical and Electromechanical Systems*, Mcgraw-Hill, New York, 1968.

[13] D'Azzo, J. J., and C. H. Houpis, *Linear Control System Analysis and Design*, McGraw-Hill Book Company, New York, 1981.

[14] Drake, S.H., "Using Compliance in Lieu of Sensory Feedback for Automatic Assembly", Doctor of Science Thesis, Massachusetts Institute of Technology, September, 1977. Also Draper Laboratory report CSDL-T-657.

[15] Forsythe, G. E., M. A. Malcolm, C. B. Moler, *Computer Methods for Mathematical Computations*, Prentice-Hall, Co., Englewood Cliffs, New Jersey, 1977.

[16] *Knyar^{TM} Piezo Film Technical Manual*, Penwalt Corp. publication.

[17] Plump, J., J. E. Hubbard, Jr., and T. L. Bailey, "Nonlinear Control of a Distributed System: Simulation and Experimental Results", presented at the 1985 ASME Winter Annual Meeting.

[18] Reid, J. G., *Linear System Fundamentals*, McGraw-Hill Book Company, New York, 1983.

[19] Schwarz R. J., and B. Friedland, *Linear Systems*, McGraw-Hill Book Company, New York, 1965.

[20] TUTSIM® User's Manual, Applied i, Palo Alto, CA.

[21] Van de Vegte, J., "The Wave Reflection Matrix in Beam Vibration Control", *Transactions of the ASME. Journal of Dynamic Systems, Measurement. and Control*, June 1971, pp. 94–101.

[22] Vaughan, D. R., "Application of Distributed Parameter Concepts to Dynamic Analysis and Control of Bending Vibrations", *Transactions of the ASME. Journal of Basic Engineering*, pp. 157–166, June 1968.

Appendix A

Fractional Operators

The operators s and $1/s$ are well known Laplace transforms of d/dt and $\int dt$: differentiation and integration, respectively. In a similar fashion, the operators $\sqrt{s}$ and $1/\sqrt{s}$ are the Laplace transforms of $d^{1/2}/dt^{1/2}$ and $\int^{1/2} dt^{1/2}$: fractional differentiation and fractional integration respectively. These fractional operators appear in equation 2.54 which is the control law for end point impedance control. Therefore, in order to implement this control law it is necessary to describe the fractional operators in the time domain. Unlike the operators s and $1/s$, the fractional operators cannot be exactly represented in closed form. They can be approximated using a Regular Newton process[10].

Carlson and Halijak [11] show that the fractional operators may be approximated with an operational amplifier circuit as shown in Fig. A.1. If the input impedance Z_i is a capacitor, then the circuit approximates the fractional derivative. If Z_i is a resistor, then the circuit approximates the fractional integral. The accuracy of the approximation improves for larger lattice networks, and the actual transfer function can be calculated by finding the equivalent impedance of the lattice network and dividing it by the input impedance Z_i. The impedance of the lattice can be found recursively starting at the top of the lattice and using the formula

$$Z_{eq} = \frac{Z_1 Z_2 + (2Z_1 + Z_2)Z_3}{Z_1 + 2Z_2 + Z_3}$$

where the Z_i are defined in Fig. A.2, which represents a single stage in the lattice. $Z_1 = R$, the resistors, $Z_3 = 1/Cs$, the capacitors, and Z_2 is equal to the equivalent impedance to the lattice network above the current stage. For the first, or top, stage, $Z_2 = 0$ since the lattice network is shorted at the top. Ta-

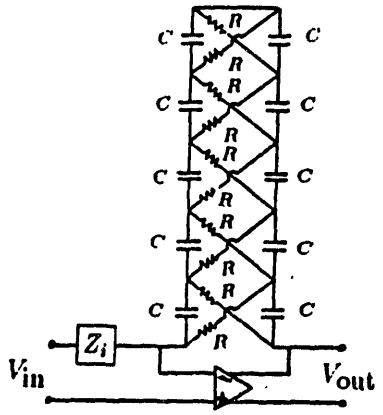

Figure A.1: Op-amp circuit for approximating fractional operators

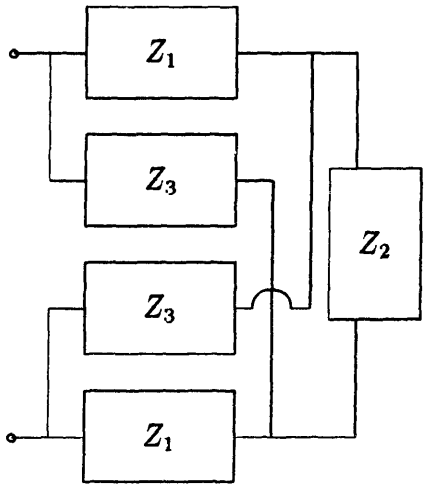

Figure A.2: Impedance representation of lattice stage

ble A.1 show the equivalent impedances for 1–5 stage lattices. By dividing the lattice impedance by R, an approximation for $\sqrt{1/RCs}$ is obtained. Similarly, by dividing the lattice impedance by $1/Cs$, an approximation for $\sqrt{RCs}$ results. Figs. A.3 and A.4 show the step responses of the fractional integrator and fractional derivative, respectively ($RC = 1$). Figs. A.5–A.8 show the calculated and experimental Bode plots for the fractional operators for $RC = 1$. In order to boost the gain of the fractional operator, it is necessary to make the product RC small. This works well for the fractional integrator, but for the fractional derivative the high frequency noise would be boosted. For the implementation of the controller described in Chapter 4, the fractional integrator was built with $RC = 0.01$. This resulted in an operator which had the transfer function shown in Fig. A.9. The phase for this operator is seen to remain steady at -45 degrees up to 100 hz, and in fact is good for much higher frequencies.

1-stage lattice	$\frac{2R}{CRs+1}$
2-stage lattice	$\frac{(4CRs+4)R}{(CRs)^2+6CRs+1}$
3-stage lattice	$\frac{(6(CRs)^2+20CRs+6)R}{(CRs)^3+15(CRs)^2+15CRs+1}$
4-stage lattice	$\frac{(8(CRs)^3+56(CRs)^2+56CRs+8)R}{(CRs)^4+28(CRs)^3+70(CRs)^2+28CRs+1}$
5-stage lattice	$\frac{(10(CRs)^4+120(CRs)^3+252(CRs)^2+120CRs+10)R}{(CRs)^5+45(CRs)^4+210(CRs)^3+210(CRs)^2+45CRs+1}$

Table A.1: Impedances of 1–5 stage lattices

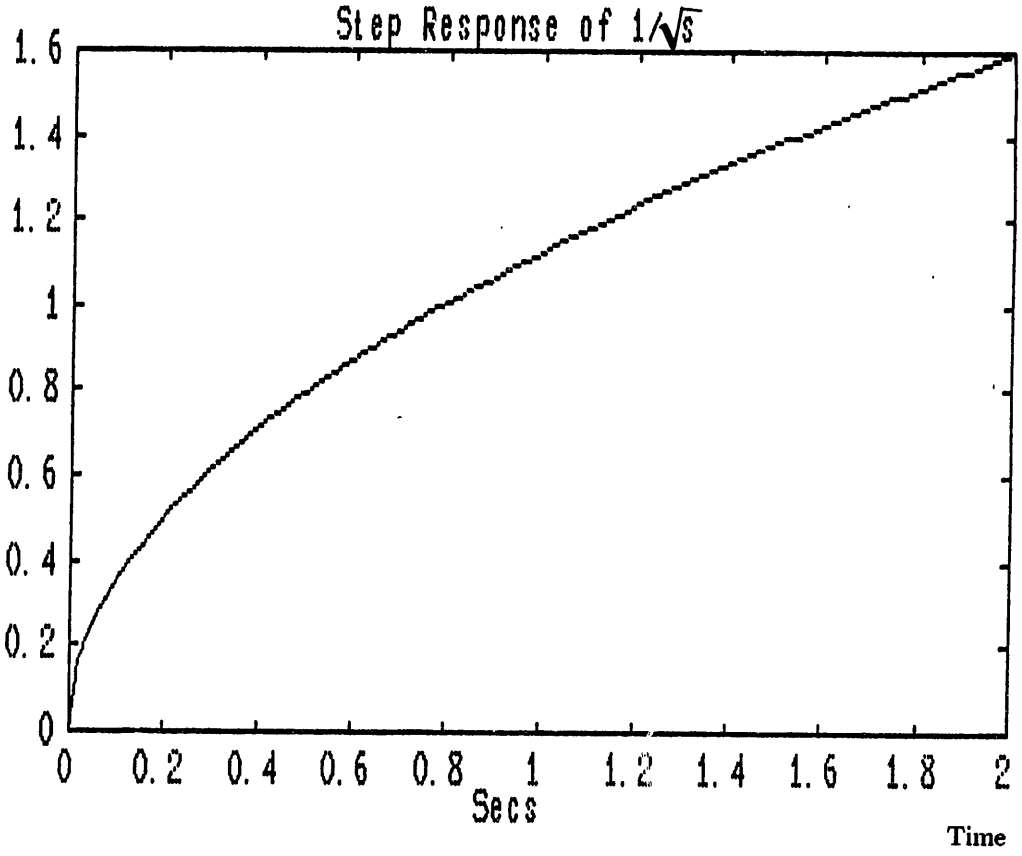

Figure A.3: Step response of $\sqrt{1/s}$

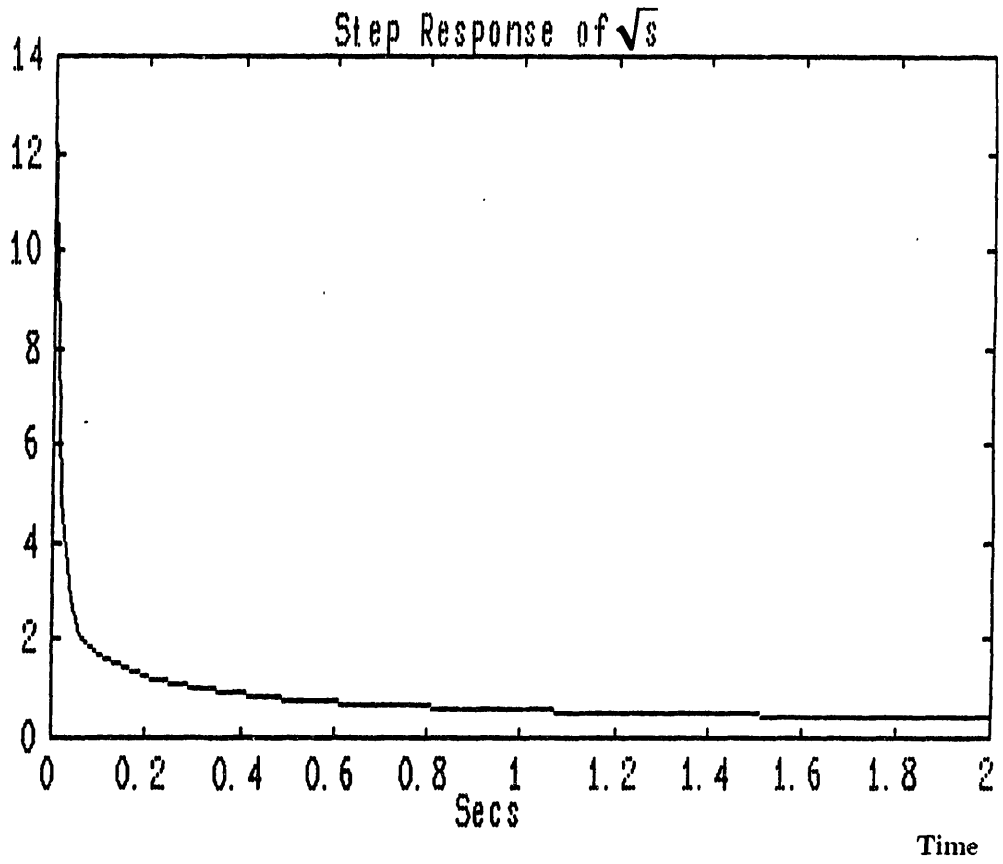

Figure A.4: Step response of $\sqrt{s}$

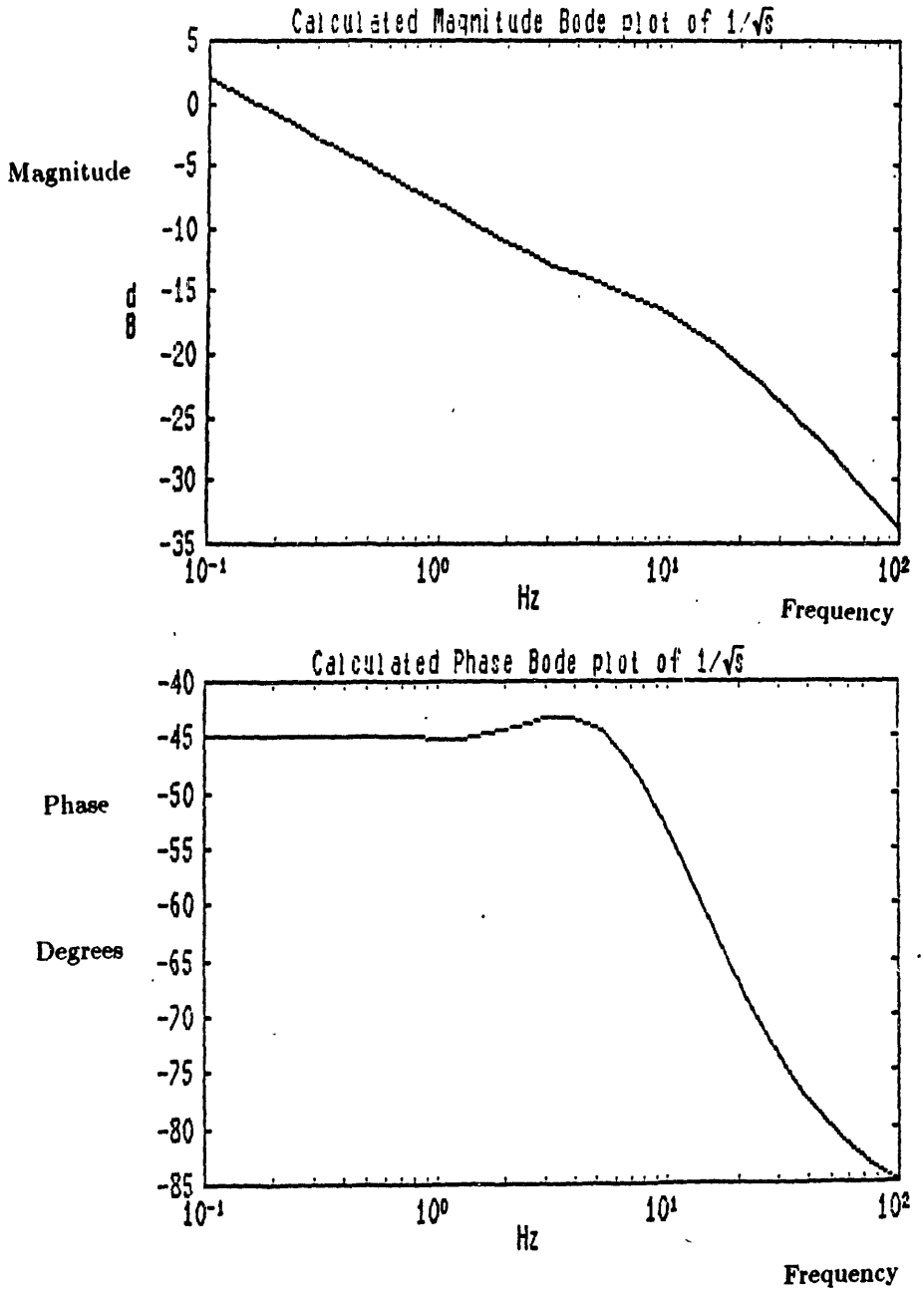

Figure A.5: Calculated Bode plot for $\sqrt{1/s}$

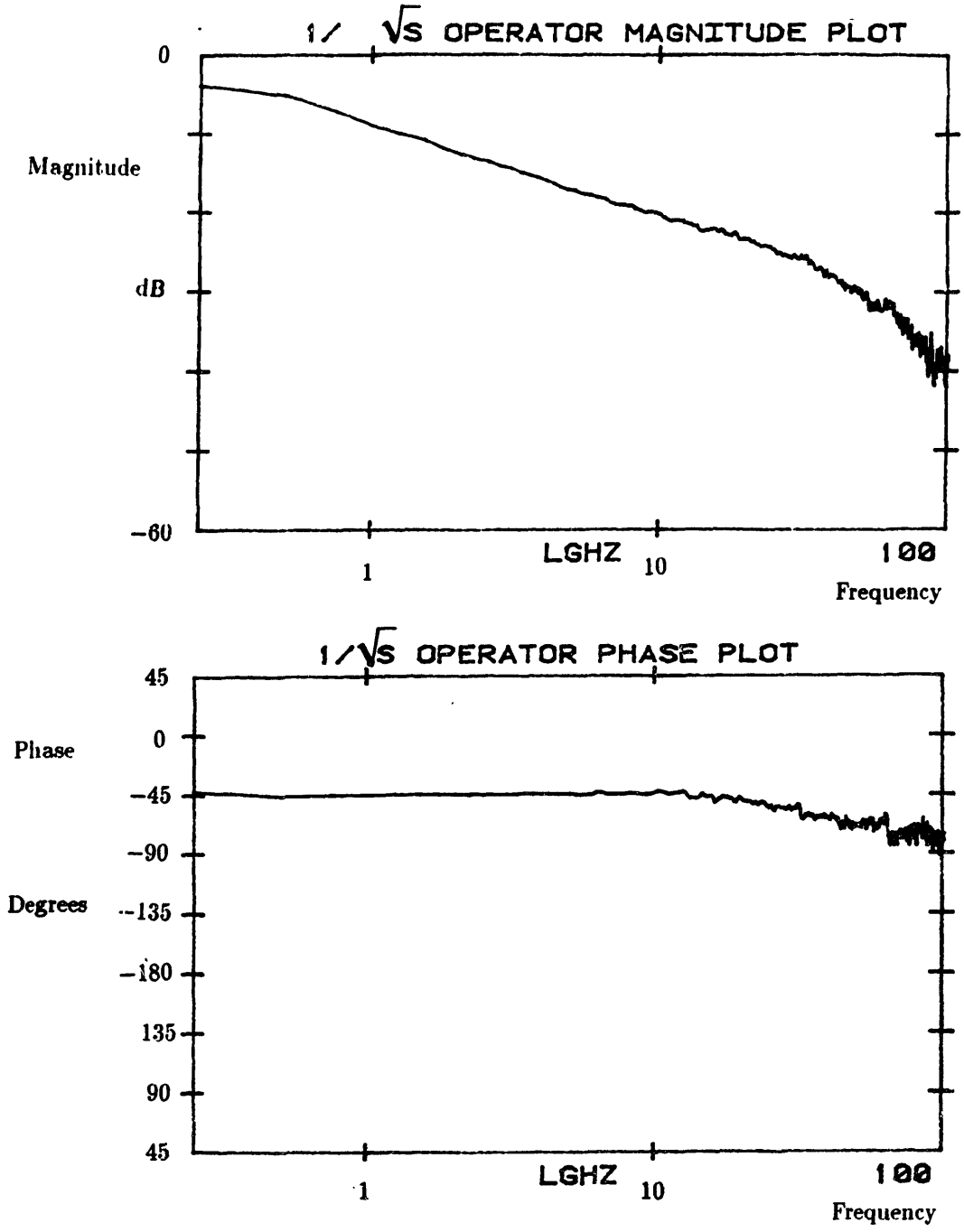

Figure A.6: Experimental Bode plot for $\sqrt{1/s}$

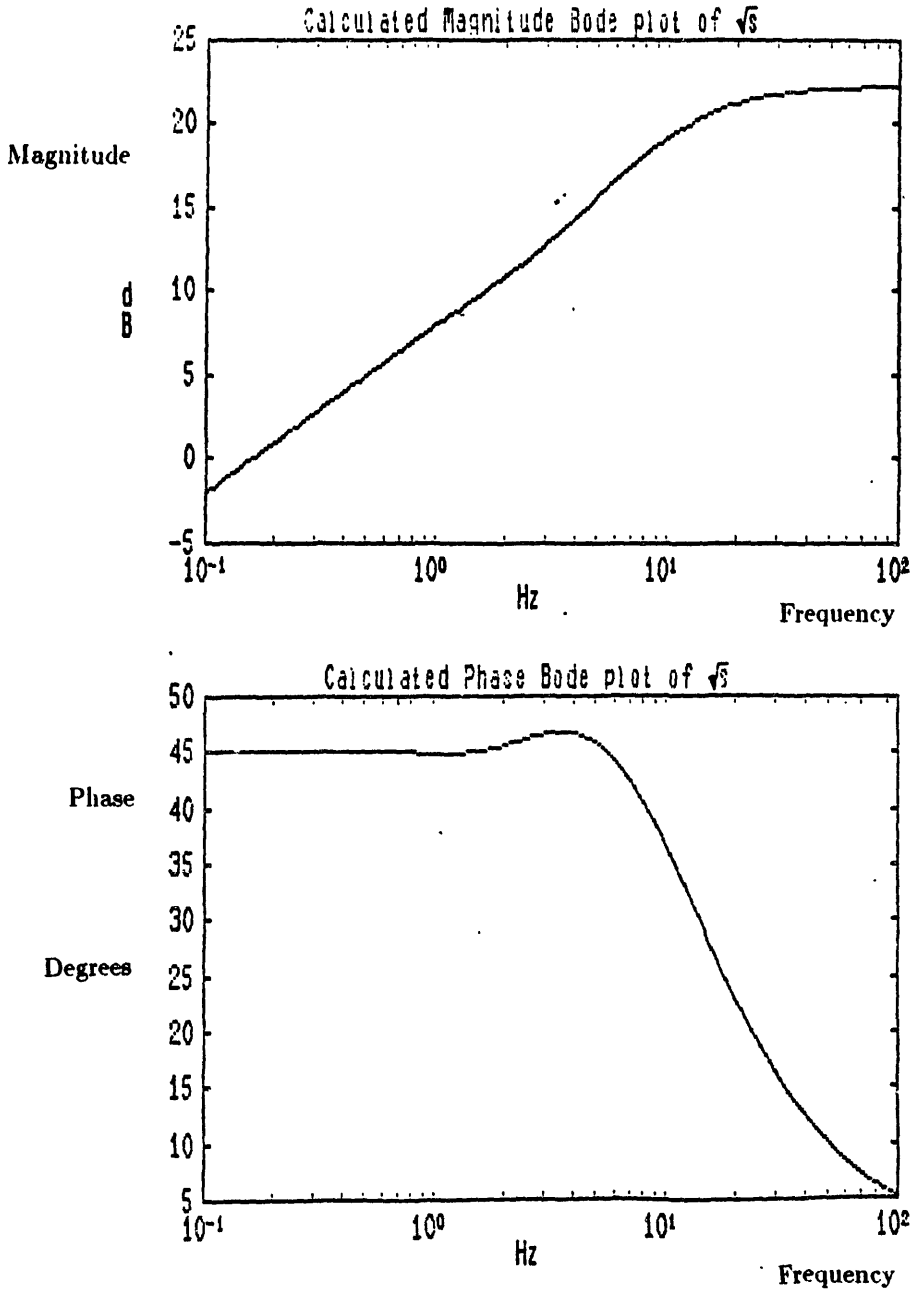

Figure A.7: Calculated Bode plot for $\sqrt{s}$

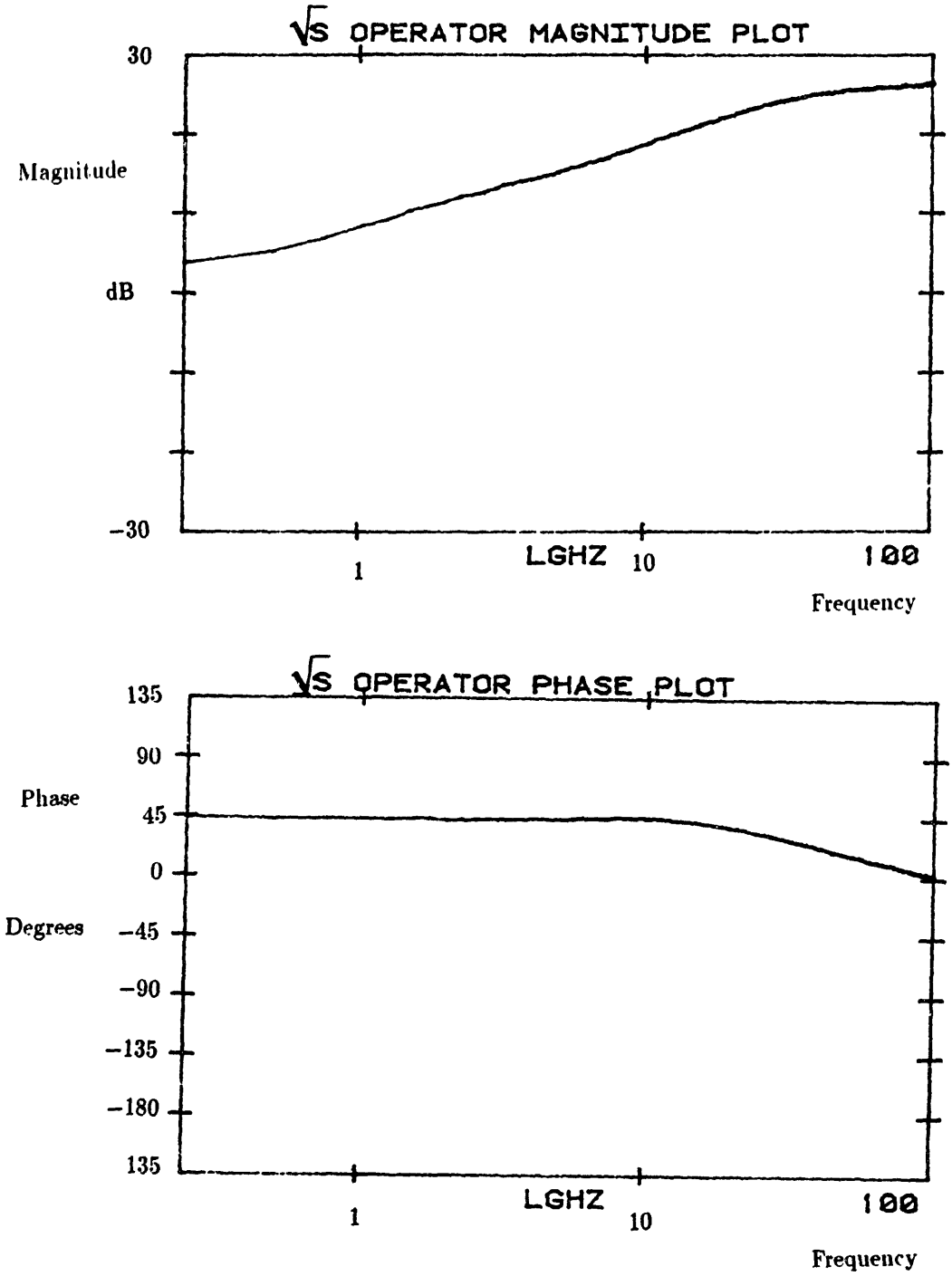

Figure A.8: Experimental Bode plot for $\sqrt{s}$

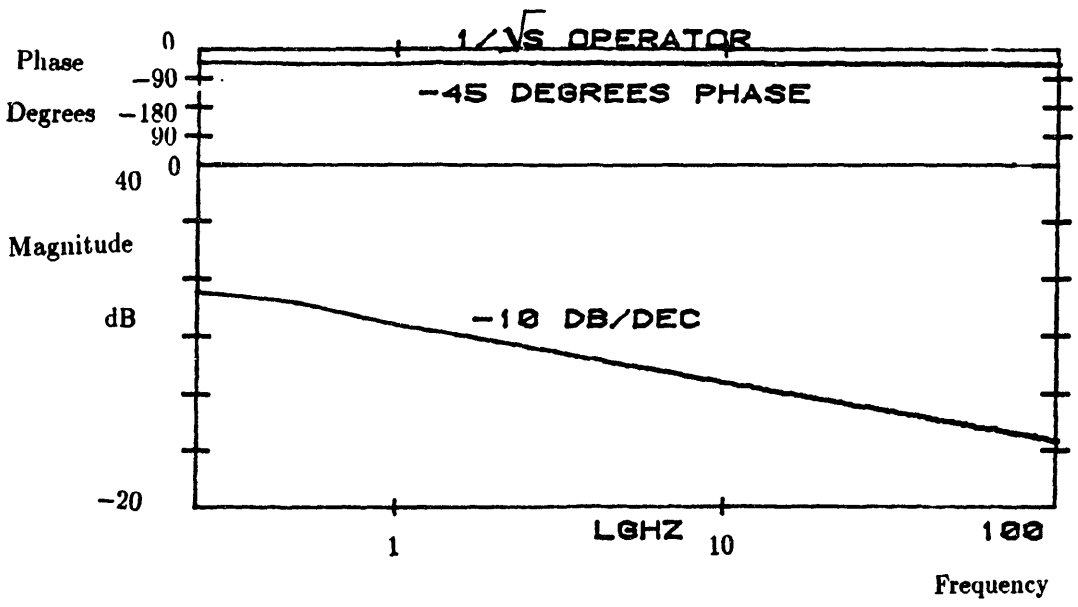

Figure A.9: $\sqrt{1/s}$ operator with $RC = 0.01$

Appendix B

Backward Integration

When using digital techniques for the simulation of dynamic systems, it is necessary to perform numerical integration. Most of the time, the popular methods of integration—Euler, Runge-Kutta, Adams-Bashford—work fine in simulating dynamic systems. There are some systems described as being "stiff" [1,15], however, which cause problems for the conventional integration techniques. These systems are characterized by large jacobian matrices and widely spaced eigenvalues. The resulting solutions are noisy and/or include unstable parasitic solutions.

One solution to this problem is to make the integration time step small enough to follow the true solution accurately. However, this will increase the time and expense of the solution, and it may not even work if the increased accuracy is lost because of truncation due to finite precision of the computer. A simple solution which works well is an implicit formula known as the backward Euler method:

$$y_{n+1} = y_n + hf(y_{n+1}, t_{n+1}) \tag{B.1}$$

where h is the integration time step, and $f(y,t)$ is defined by the differential equation

$$y' = f(y). \tag{B.2}$$

Compare equation B.1 to the formula for normal Euler integration:

$$y_{n+1} = y_n + hf(y_n, t_n).$$

In terms of a state space formulation, the governing differential equation is

$$\begin{aligned} \dot{\mathbf{x}} &= \mathbf{A}\mathbf{x} + \mathbf{B}\mathbf{u} \\ \mathbf{y} &= \mathbf{C}\mathbf{x} + \mathbf{D}\mathbf{u} \end{aligned} \tag{B.3}$$

where $\mathbf{y}$ is the vector of output variables, $\mathbf{x}$ is the vector of state variables, and $\mathbf{u}$ is the vector of input variables. In state space notation, the discrete system equation is

$$\mathbf{x}_{n+1} = \mathbf{x}_n + h(\mathbf{A}\mathbf{x}_{n+1} + \mathbf{B}\mathbf{u}_{n+1}). \tag{B.4}$$

Solving for the state vector at step $n+1$, a simple recursive equation is obtained:

$$\mathbf{x}_{n+1} = (\mathbf{I} - h\mathbf{A})^{-1}\mathbf{x}_n + (\mathbf{I} - h\mathbf{A})^{-1}h\mathbf{B}\mathbf{u}_{n+1}. \tag{B.5}$$

This equation is easily implemented on any computer with very good results. As an example Fig. B.1 shows the step response for the free-free beam given in Chapter 3 of the angular velocity $\dot{\theta}_a$ to a moment input at the same end, M_a. The highly oscillatory solution was produce by conventional Adams integration (as used by PC-MATLAB), and is readily seen to be much noisier than the solution produced via backward integration.

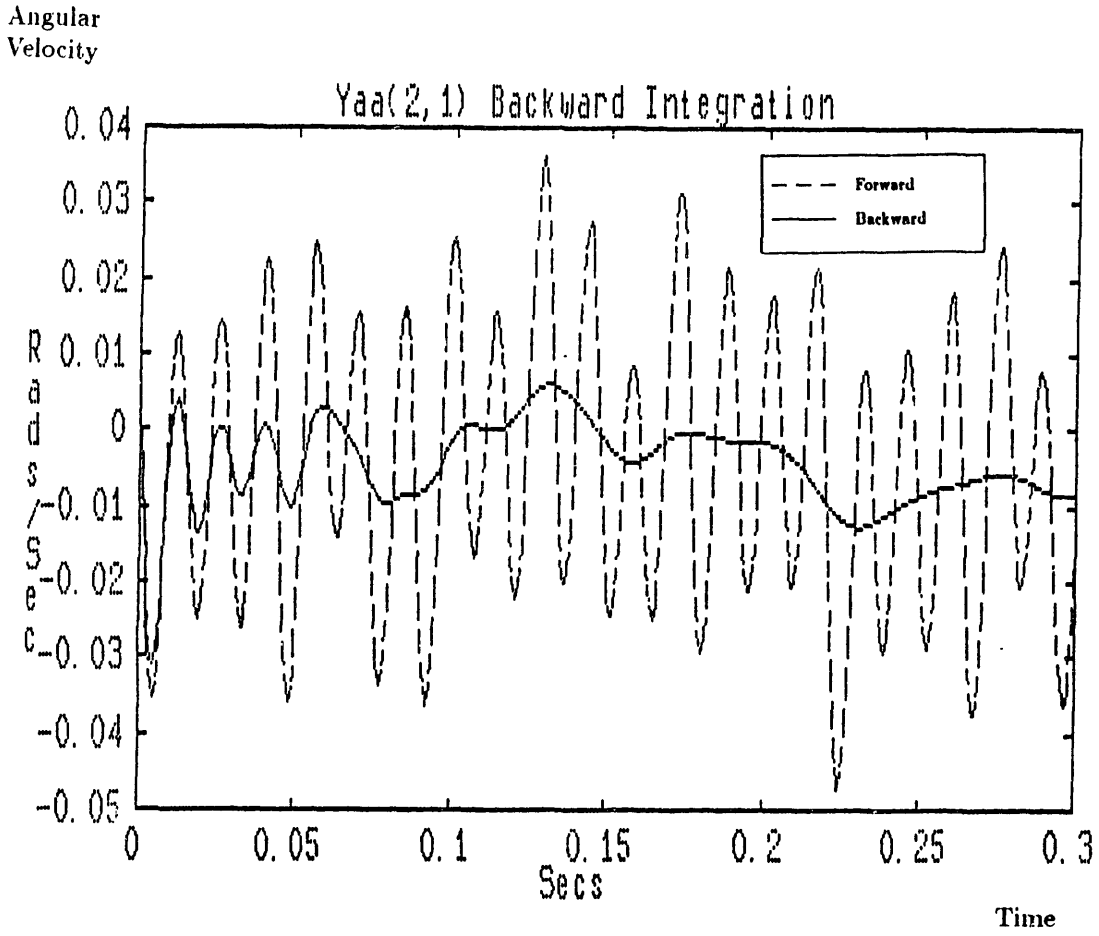

Figure B.1: Comparison of backward integration to forward integration

Appendix C

Film Actuators

The actuators used in the clamped-free and the clamped-sliding beam experiments were made using piezoelectric polymer film [16]. With the film glued to the side of a beam, a distributed moment over the length of the beam was created with the application of an electric field across the film. By shaping the film, the distributed moment over the length of the beam could be made to emulate a variety of forces and/or moments. The controllers examined in this thesis required the use of a moment actuator and a force actuator at the tip of the beam. The piezoelectric film can be distributed in such a way as to produce these two actuators [9].

C.1 Moment

By using a spacially uniform film distribution on the beam (see Fig.C.1), the film produces a uniform moment distribution over the length of the beam which can be modelled as a moment applied at the end of the beam. To find the relationship between an applied voltage and the moment produced at the tip of the beam it is convenient to use the Liapunov functional

$$F = \frac{1}{2}\int_0^l \left[EI\left(\frac{\partial^2 w}{\partial x^2}\right)^2 + \rho A\left(\frac{\partial w}{\partial t}\right)^2 \right] dx \qquad \text{(C.1)}$$

where w is the displacement of the beam from its undisturbed state. The motion of a beam with a piece of piezoelectric film attached to one side is described by the equation [3]

$$EI\frac{\partial^4 w}{\partial x^4}\rho A\frac{\partial^2 w}{\partial t^2} = m\frac{\partial^2 V}{\partial x^2} \qquad \text{(C.2)}$$

where

$EI = E_1 I_1 + E_2 I_2$
E_1 =Elastic modulus of beam
E_2 =Elastic modulus of film
I_1 =Area moment of inertia of beam
I_2 =Area moment of inertia of film

and

$m = -d_{31} \frac{h_1+h_2}{2} \frac{E_1 h_1 E_2 B}{E_1 h_1 + E_2 h_2}$
d_{31}=film piezoelectric constant
h_1 =thickness of beam
h_2 =thickness of film
B =width of beam

V is the voltage applied across the film.

The boundary conditions for a clamped-free beam are

$$w = \frac{\partial w}{\partial x} = 0 \quad @ \quad x = 0$$

$$\left.\begin{array}{l} EI\frac{\partial^2 w}{\partial x^2} = mV \\ EI\frac{\partial^3 w}{\partial x^3} = m\frac{\partial V}{\partial x} \end{array}\right\} \quad @ \quad x = l. \tag{C.3}$$

By letting $V(x,t) = V_{\max}\Lambda(x)\rho(t)$ where $V_{\max}$ is the maximum applied voltage, $|\Lambda(x)| \leq 1$ is the film distribution on the beam, and $|\rho(t)| \leq 1$ is the time history of the applied voltage, the Liapunov functional F may be extremized to yield

$$\left.\begin{array}{l} \dfrac{dF}{dt} = \underbrace{mV_{\max}\,\rho(t)}_{\text{moment}} \underbrace{\dfrac{d^2w(l,t)}{dxdt}}_{\substack{\text{angular} \\ \text{velocity}}} \end{array}\right\} \text{power} \tag{C.4}$$

It is seen from the above equation that the magnitude of the moment at the end of the beam is $M_{\max} = mV_{\max}$. One of the actuators on the clamped-free beam used for experimentation produced the moment

$$M = -9.937 \times 10^{-5} V_{\max}\,\rho(t) \ \frac{\text{in lbf}}{\text{V}}.$$

C.2 Force

By using a linear spacial distribution of film over the beam (see Fig. C.2), the

distributed moment varies linearly over the length of the beam which may be modelled as a force at the end of the beam. Using this shape in a calculation similar to that for the uniform distribution of film, the power extracted by the film is

$$\left.\begin{aligned} \frac{dF}{dt} = \underbrace{\frac{mV_{\max}\,\rho(t)}{l}}_{\text{force}} \underbrace{\frac{dw(l,t)}{dt}}_{\text{velocity}} \end{aligned}\right\} \text{power} \qquad \text{(C.5)}$$

In the case of the clamped-free experiment, the force produced at the tip of the beam was

$$Q = -9.0 \times 10^{-7} V_{\max}\,\rho(t)\ \frac{\text{lbf}}{\text{V}}.$$

For the beam used in the clamped-sliding experiment, the force was

$$Q = -1.7364 \times 10^{-4} V_{\max}\,\rho(t)\ \frac{\text{lbf}}{\text{V}}.$$

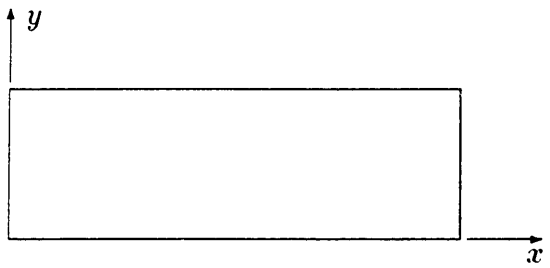

Figure C.1: Uniform distribution of film

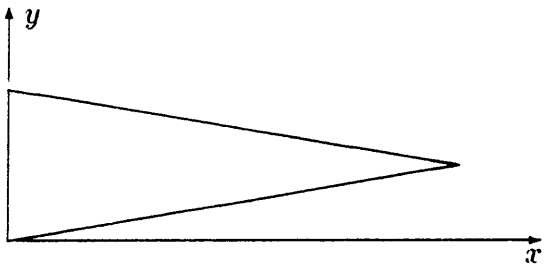

Figure C.2: Linear distribution of film